Università degli Studi di Padova

DIPARTIMENTO DI TECNICA E GESTIONE DEI SISTEMI INDUSTRIALI

Corso di Laurea Magistrale in Ingegneria Meccatronica

Commissioning and first measurements of a new ICP discharge experiment at the Neutral Beam Test Facility

Relatore:
Prof. Emanuele Sartori

Correlatore:
Dott.ssa Isabella Mario

Candidato:
Edgard Zuin
Matricola 2058882

Anno Accademico 2023/2024

Abstract

ITER is an international project aimed at demonstrating the feasibility of nuclear fusion as a source of sustainable and clean energy. In order to reach and sustain nuclear fusion reactions external heating systems such as Neutral Beam Injectors (NBI) are necessary. Two NBIs (and a third one is provisional) are foreseen for ITER, delivering up to 33 MW of heating power to fusion plasma injecting beams of neutral particles at high energy. These beams are produced by neutralizing a precursor negative ion beam extracted from a caesiated plasma source. The source plasma is produced by inductive coupling in multiple RF drivers at 1 MHz frequency.

SPIDER, in operation since 2018, is the full-scale prototype of the negative ion source that will be installed on ITER. The experimental phase of SPIDER, as well as the results of RF driver ion source worldwide, highlighted that the achieved extracted current at the maximum RF power is marginal to fullfill the ITER requirements.

With the aim of investigating and implementing engineering and physical solutions to increase the extracted current density by providing the effective power coupling of the RF source, a new facility, MINION, has been created and developed.

In this context, the main objective of this thesis work was firstly to contribute to the commissioning of the experiment, and of the various plant systems. A study dedicated to inductive coupling within the RF source was then pursued, both experimentally and numerically. To this end, magnetic measurements and three-dimensional finite-element-simulations were carried out, to provide the interpretation of the experimental evidences, which are strongly influenced by the magnetic field structure. Finally, axis-symmetric simulations of the RF induced electric field and current densities on both the passive structures and the plasma were developed using the finite element code FEMM.

Sommario

ITER è un progetto internazionale finalizzato a dimostrare la fattibilità della fusione nucleare come fonte di energia sostenibile e pulita. Per raggiungere e mantenere le reazioni di fusione nucleare sono necessari sistemi di riscaldamento esterno come gli iniettori di neutri. Due iniettori (e un terzo è provvisorio) sono previsti per ITER, tali da fornire fino a 33 MW di potenza di riscaldamento al plasma iniettando fasci di particelle neutre ad alta energia. Questi fasci sono prodotti neutralizzando un fascio di ioni negativi precursori estratti da una sorgente di plasma. Il plasma della sorgente è prodotto un da accoppiamento induttivo in multipli driver RF a frequenza di 1 MHz.

SPIDER è il prototipo su scala reale della sorgente di ioni negativi che sarà installata su ITER, in funzione dal 2018. La fase sperimentale di SPIDER, così come i risultati dei driver RF delle sorgenti di ioni a livello mondiale, hanno evidenziato che la corrente estratta raggiunta alla massima potenza RF è marginale per soddisfare i requisiti di ITER.

Con l'obiettivo di investigare e implementare soluzioni ingegneristiche e fisiche per aumentare la densità di corrente estratta fornendo l'accoppiamento efficace di potenza della sorgente RF, è stata creata e sviluppata una nuova sorgente, MINION.

In questo contesto, l'obiettivo principale di questo lavoro di tesi è stato innanzitutto contribuire alla messa in servizio dell'esperimento e dei vari sistemi impiantistici. Quindi è stato condotto uno studio dedicato all'accoppiamento induttivo all'interno della sorgente RF, sia dal punto di vista sperimentale che numerico. A tal fine, sono state effettuate misurazioni magnetiche e simulazioni agli elementi finiti tridimensionali, per fornire l'interpretazione delle evidenze sperimentali, che sono fortemente influenzate dalla struttura del campo magnetico. Infine, sono state sviluppate simulazioni assialsimmetriche del campo elettrico indotto dalla sorgente RF e delle densità di corrente sia sulle strutture passive che sul plasma utilizzando il codice a elementi finiti FEMM.

Contents

Chapter 1

Introduction

1.1 The energy problem

Energy consumption worldwide has experienced exponential growth since the middle of the 19th century. As shown in Figure 1.1, world energy consumption has been

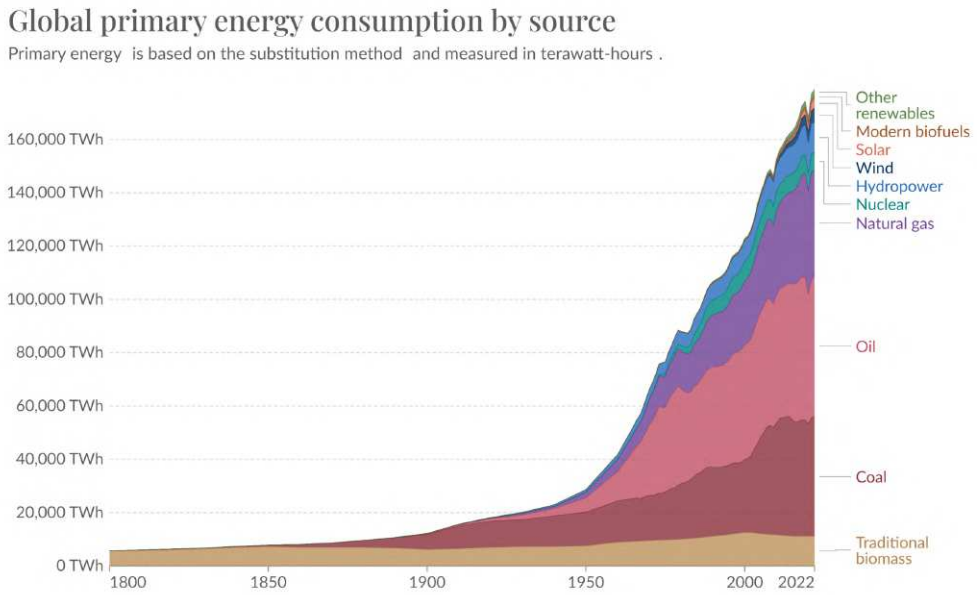

Figure 1.1: Global energy consumption divided by source type [1].

almost constantly on the rise, with a particularly steep increase in the last 50 years. The constant growth of the world population and the resulting industrial development are the main factors responsible for the increasing demand for energy. Nowadays, the majority of energy is still produced from non-renewable sources such as coal, oil and natural gas. However, issues related to climate change and air pollution have become increasingly relevant, leading the governments of major countries around the

world to implement energy development policies aimed at reducing pollutant emissions in energy production processes. The search for new energy sources having the advantages of being relatively clean and nearly inexhaustible capable of competing with non-renewable fuels, has consequently seen substantial economic investments. A potential energy source option that meets these criteria is controlled thermonuclear fusion.

1.2 Energy production by nuclear fusion

Nuclear fusion is the process by which two light atomic nuclei combine to form a single heavier one while releasing massive amounts of energy. The main obstacle to fusion is the electrostatic repulsion force between nuclei; to overcome it, it is necessary to provide them with sufficient energy. Elevated kinetic energy indeed enhances the probability to overcome the repulsive Coulomb barrier through the tunnel effect. Under such conditions, nuclei can approach each other until a distance is reached where nuclear forces prevail, and fusion can therefore occur.

The binding energy per nucleon (BEN) define the average energy required to remove an individual nucleon from a nucleus. A graph of binding energy per nucleon versus mass number A is given in Figure 1.2.

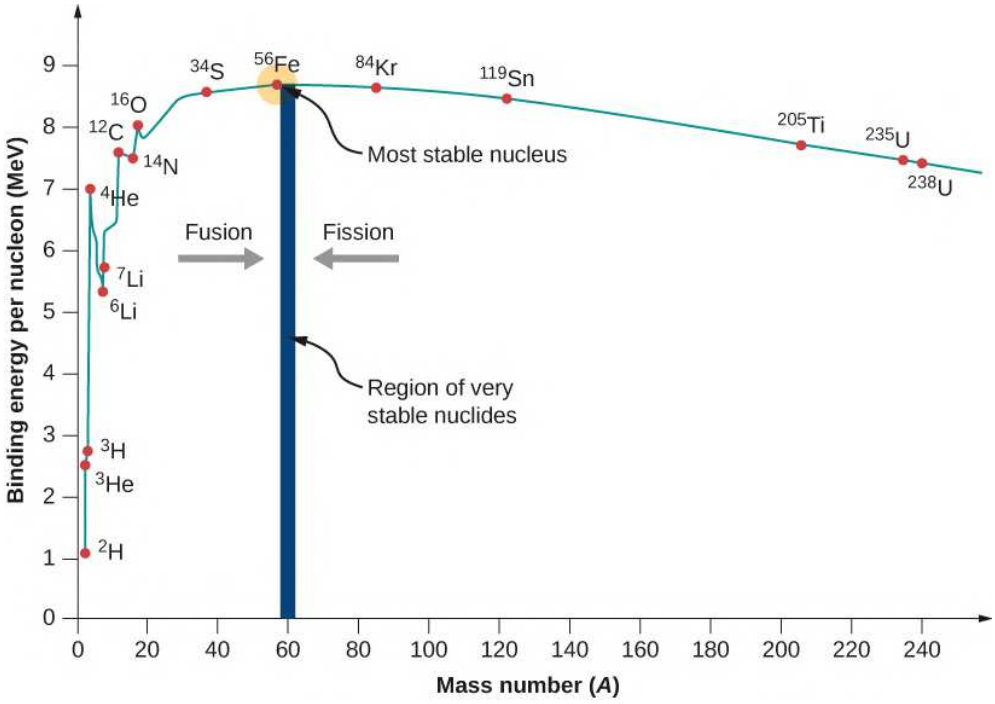

Figure 1.2: Binding energy per nucleon for stable nuclei [2].

As we can see, the graph rises at low A, peaks very near iron $^{56}_{26}$Fe and then tapers

off at high A. The peak value indicates that the iron nucleus stands as the most stable nucleus in the natural world. The rising and tapering off of the graph is attributed to the interplay of competing forces within the nucleus: for lower mass number$A$, nuclear force prevails, holding nucleons together in more strongly way, whereas for higher A, coulomb repulsion force prevails, tending to break apart the nucleus. This constitutes a pivotal aspect in nuclear reactions since only heavier nuclei, such as ${}^{235}_{92}\mathrm{U}$ and ${}^{239}_{94}\mathrm{Pu}$, which can be readily separated, are appropriate for fission reactions. Conversely, only lighter nuclei are suitable for fusion reactions. For this reason, only some reactions are energetically favorable for the nuclear energy production and they involve deuterium and tritium.

The main ones are the following:

$$
\begin{aligned}
{}^{2}\mathrm{D} + {}^{2}\mathrm{D} &\Rightarrow {}^{3}\mathrm{He}(0.82\mathrm{MeV}) + \mathrm{n}(2.45\mathrm{MeV}) \\
{}^{2}\mathrm{D} + {}^{2}\mathrm{D} &\Rightarrow {}^{3}\mathrm{T}(1.01\mathrm{MeV}) + {}^{1}\mathrm{H}(3.02\,\mathrm{MeV}) \\
{}^{2}\mathrm{D} + {}^{3}\mathrm{T} &\Rightarrow {}^{4}\mathrm{He}(3.5\mathrm{MeV}) + \mathrm{n}(14.1\mathrm{MeV}) \\
{}^{2}\mathrm{D} + {}^{4}\mathrm{He} &\Rightarrow {}^{4}\mathrm{He}(3.6\mathrm{MeV}) + {}^{1}\mathrm{H}(14.7\mathrm{MeV})
\end{aligned}
$$

Among all these alternatives, the D-T reaction holds a central position in global fusion research efforts. The probability of taking place a fusion reaction is contingent on the cross-section, which is influenced by the particle's energy, as illustrated in Figure 1.3. It is evident from the figure that the reaction featuring deuterium and tritium possesses the highest cross-section at lower temperatures.

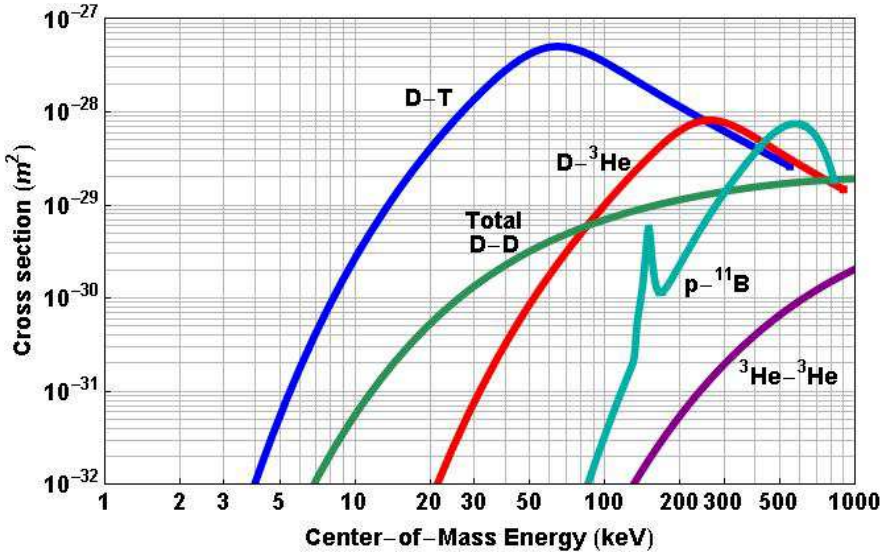

Figure 1.3: Cross-sections of some fusion reactions as functions of Center of Mass Energy (keV) [3].

Both of these isotopes of hydrogen are either naturally abundant or can be artificially produced on Earth. Deuterium is available in seawater (30 g/m^3) hence, it can be regarded as practically limitless concerning the requirements for future fusion reactors. Tritium, on the other hand is not a stable isotope and has a limited lifespan. For these reasons it is not possible to obtain it in nature in a sufficiently high quantity to meet a constant production of energy but it can be obtained in a fusion reactor through a reaction from lithium:

$$n + {}^6\mathrm{Li} \Rightarrow {}^4\mathrm{He} + \mathrm{T} + 4.8\mathrm{MeV}$$

Therefore, the primary fuels for a fusion power plant are deuterium and lithium, and the latter, extractable from the Earth's crust, does not pose critical issues in terms of availability [4]. The key advantage of nuclear fusion, in contrast to fission, lies in its passive safety: achieving and sustaining the necessary physical conditions for fusion is extremely challenging. Consequently, in the event of any anomalous operation of the fusion device, stopping it would be straightforward without significant consequences on a large scale. Additionally, the nuclear waste generated by neutron activation of the materials in the fusion device has a much shorter lifetime (some decades). For these reasons, nuclear fusion can offer a clean and competitive method of energy production compared to the use of non-renewable resources.

1.3 Plasma and energy balance

To attain a reaction rate that is sufficiently high, it is necessary to reach elevated temperatures (around 10^8 K). Under these physical conditions, matter exists in a plasma state.

Plasma, also known as the "fourth state of matter," is a nearly ionized gas composed of charged and neutral particles, which can be achieved by heating ordinary gas. The macroscopic quasi-neutrality of plasma is maintained by the mutual compensation of the spatial charge of the positive ions and electrons that constitute it. Under steady-state conditions, not only the overall charge density of the plasma is almost neutral, but also the sum of currents due to the two species of opposite charge is nearly zero e.g. at the walls of the containment chamber. Any charge inside the plasma is shielded by the plasma itself over a limited distance, defined by the Debye length λ_D in Equation 1.1 [5],

$$\lambda_D = \sqrt{\frac{\varepsilon_0 k_B T_e}{n e^2}} \tag{1.1}$$

where ε_0 is the permittivity in free space, k_B is the Boltzmann constant, T_e is the elec-

tron temperature, n is the electron density and e is the electron charge. Physically, this parameter corresponds to the length scale that the plasma takes to screen the external field, which is the typical distance over which an imbalance of electric charge can exist. It's crucial to observe that the Debye length λ_D increases as the electron temperature T_e rises and as the plasma density n decreases.

The net energy gain Q in a steady-state for a fusion reactor is defined as the ratio of output power P_{out} to input power P_{in}. In order for the fusion reaction to be considered advantageous, it is necessary for Q to be greater than 1, meaning that the energy produced through the fusion reaction must be greater than the energy required to initiate and sustain the reaction itself. The input power is composed of various contributions from different effects that concatenate. The main contribution comes from the power deposition inside the plasma through the α-particles produced by the fusion reaction itself. Ideally, this contribution could be the only effect needed to heat the plasma, which is why we talk about a self-sustaining condition in a thermonuclear reactor. In reality energetic neutrons escaping the fusion chamber are lost, thus other external heating methods are added to this contribution, RF waves ranging from MHz to GHz and neutral beam, with a consequent decrease in the gain factor Q. The output components arise from transport and radiation, primarily attributed to the bremsstrahlung effect. The transport phenomena can be described by the energy confinement time τ_e defined as:

$$\tau_e = \frac{W}{P_L} \tag{1.2}$$

where W is the total energy stored in the plasma and P_L is the total power lost due to transport phenomena. In a simple case, without considering additional external heating, the Lawson criterion sets a threshold beyond which the energy produced by nuclear fusion reaction is greater than the power necessary to heat the plasma:

$$n\tau_e \geq \frac{12k_BT_e}{E_\alpha\langle\sigma v\rangle} \tag{1.3}$$

where σ is the cross-section of the fusion reaction, in Figure 1.3, and E_α is the energy of the produced α-particles. Plotting Equation 1.3 against temperature, in keV, a minimum of the curve is obtained at the location of the *ignition condition*, around $T = 25$ keV, that is the ideal condition in which the nuclear fusion is self-sustaining and the gain factor $Q = \infty$. This outcome is pivotal as the interplay of temperature, confinement time, and plasma density plays a fundamental role in fusion research. The product of these three parameters, known as the triple product, offers a convenient means to define the ignition condition. In the case of a D-T reaction, this condition corresponds to:

$$nT\tau_e > 5 \times 10^{21} \mathrm{m}^{-3}\mathrm{keVs} \tag{1.4}$$

In order to reach such condition and to increase the triple product is essential to confine the plasma. The basic idea is that through confinement, it is possible to increase the density of the plasma or the energy confinement time. Among the various techniques studied, only two are the most widely used in terms of relevance and effectiveness: the inertial confinement and the magnetic confinement. The first one, involving a laser system, heats a compressed fuel pellet with the goal of extracting fusion energy before the system undergoes expansion and cooling caused by Rayleigh Taylor instability (interface instability). The idea is to increase the triple product by increasing the plasma density [6]. The second one, the magnetic confinement, relies on confining plasma in toroidal geometry using magnetic fields. The idea is to enhance the triple product by enhancing the confinement time. This method will be discussed in the following section.

1.3.1 The magnetic confinement

The charged particles contained within the plasma, when subjected to an externally applied magnetic field, move along the field lines. The particles, that move with a velocity component perpendicular to the field, are indeed subject to the Lorentz force, defined as:

$$\vec{F} = q\vec{v} \times \vec{B} \tag{1.5}$$

where q is the particle charge, $\vec{v}$ is the particle velocity and $\vec{B}$ is the magnetic field. The particle are trapped in closed helicoidal trajectories inside the plasma volume. This method allows for the containment and confinement of plasma within a finite volume. The circle of the trajectory is described by the *Larmor radius*, defined by:

$$r_L = \frac{mv_\perp}{qB} \tag{1.6}$$

where $v_\perp$ is the perpendicular component of the particle velocity. The typical frequency of the motion is called cyclotron frequency ω_c defined by:

$$\omega_c = \frac{qB}{m} \tag{1.7}$$

The simplest configuration for a confined plasma is a linear column, but the main challenge lies in particle losses at the column's edges. The solution involves a toroidal shape for the vessel where coils generate a magnetic field. The most commonly used

devices based on magnetic confinement are *tokamak*[1] and stellarator. In both of them, the magnetic field lines wrap around the torus in a helical shape, owing to the presence of two magnetic fields:

- a toroidal field produced by the external coil that surrounds the torus;
- a poloidal field component that induced a centripetal force. This second field is necessary to prevent the lateral drift of confined charged particles produced by the magnetic field gradient generated by the toroidal field. This phenomenon would result in a degradation of confinement if there were no presence of the toroidal field.

Therefore, the toroidal field serves as the guiding center for the helical trajectories of electrons and ions and the poloidal field prevents particles from drifting vertically and escaping the confinement region outward. The combination of these two magnetic fields oppose the plasma's expansion toward the inner walls of the ring-shaped vacuum vessel.

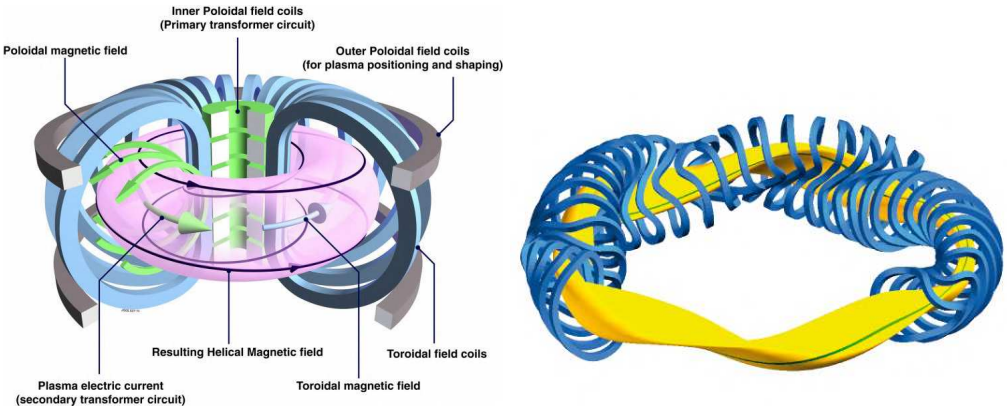

(a) (b)

Figure 1.4: (a) sketch of a *tokamak* magnetic confinement system, example of the JET facility in Great Britain [7]; (b) sketch of the stellarator magnetic confinement, example of Wendelstein-7X facility in Germany[8].

In Figure 1.4 the two configurations most commonly used for magnetic confinement are presented. The fundamental difference between these two geometries lies in the fact that, in the *tokamak* configuration, the poloidal field is induced by a toroidal current achieved by a central solenoid magnet, whereas in the stellarator configuration, the field depends only on the shape of the coil used. Stellarators have certain advantages, such as the potential for steady-state operation and reduced reliance on external magnetic field coils, but they also pose engineering challenges due to their complex geometry.

[1] *Tokamak* is a Russian acronym for toroidal chamber with magnetic coils.

1.4 The ITER project

In this scenario, the largest international experiment on nuclear fusion is located in Cadarache, France.

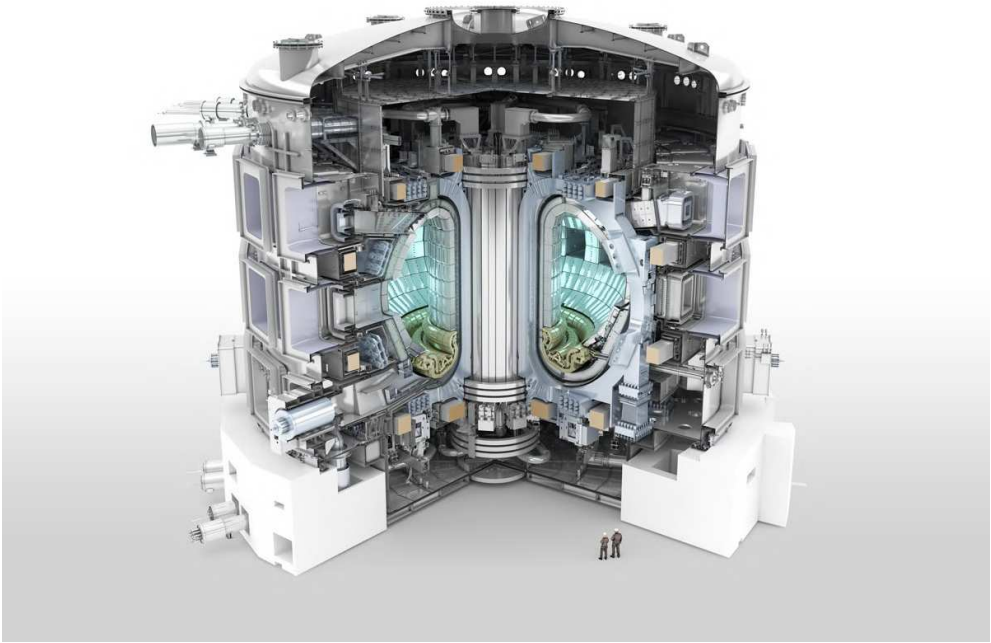

Figure 1.5: Technical design of ITER tokamak [9].

The ITER project originated from a 2006 agreement signed by China, the European Union, India, Japan, Korea, Russia, and the United States. The objective is to create the largest fusion generator with the purpose of testing the physical feasibility of producing energy through a nuclear fusion reaction. In particular, ITER aims at obtaining a power gain of $Q = 10$, with a nominal power output of 500 MW. ITER is slated to become the world's largest *tokamak* configuration thermonuclear reactor.

As mentioned before, in order to initiate a nuclear fusion reaction, it is necessary for the matter to be under extreme conditions of heat and pressure. The challenge is to succeed in reproducing these conditions within the vacuum chamber, where the gaseous hydrogen fuel transforms into plasma. In pursuit of this objective, ITER is configured with the parameters outlined in Table 1.1.

These features position ITER as the pioneering fusion device capable of successfully generating net energy. Regrettably, this proves to be a daunting task, and although progress toward the ultimate goal is ongoing, several parameters still need to meet the required specifications.

One of the most challenging aspects to achieve is maintaining the temperature of the produced plasma at high values in order to operate for long periods. It is necessary,

Parameter	Value
Fusion power	500 MW
Power gain factor Q	10
Pulse length	up to 3600 s
Plasma major radius	6.2 m
Plasma minor radius	2.0 m
Plasma current	15 MA
Toroidal field at 6.2 m radius	5.3 T

Table 1.1: ITER main parameters [9].

therefore, to continue heating the plasma particles, counteracting energy losses, in order to maintain conditions conducive to triggering the plasma and simultaneously ensuring the required power factor. To this end, the ITER project envisages three plasma heating modes:

- Ohmic heating, which can be defined as "intrinsic" heating, originating from the poloidal plasma current induced by the tokamak coils. Similar to an electric current flowing through a metal wire heating it up, the toroidal plasma current circulating around the tokamak releases its energy, thereby heating the plasma. This method provides only the initial heating because it becomes less effective as the temperature increases due to the fact that the plasma resistivity η is proportional to $T^{\frac{3}{2}}$.

- Radio-Frequency heating, is instead an "external" heating consisting in the excitation of the electrons emitting electromagnetic (EM) waves within the tokamak. EM waves infiltrate the plasma until they reach the resonance condition, absorbing and transferring their energy to plasma particles.

- Neutral beam heating, which is another "external" heating method based on the neutral beam injection will be described in section 1.4.1.

The Figure 1.6 illustrates the plasma heating system implemented in ITER.

1.4.1 Neutral beam injection (NBI)

Neutral-beam injection (NBI) is a technique employed to heat the plasma inside a fusion device. It involves directing a stream of high-energy neutral particles into the magnetic confinement field. Once inside, these neutral particles undergo ionization through collisions with the plasma particles. The confining magnetic field retains these ionized particles in the plasma, allowing them to transfer a significant amount of their

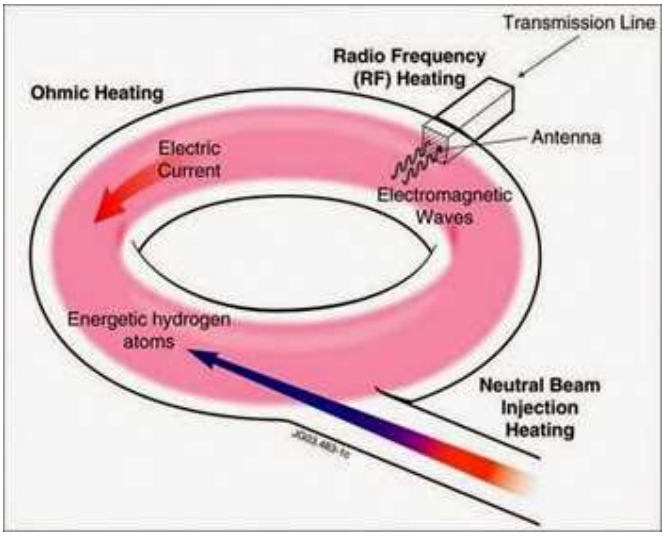

Figure 1.6: Sketch of the ITER heating system composed by ohmic heating, Radio-Frequency heating (RF) and neutral beam heating.

energy through additional collisions with the plasma. It is important to highlight that the beam of neutrals produced and injected must be designed to have precise energy. Indeed, if the particle beam is too weak, it fails to reach the core of the plasma, and the heating process becomes less effective. Conversely, if the beam has too much energy, it may pass through the plasma core and collide with the vessel wall without being fully absorbed.

Energetic neutral beams are generated by neutralizing a precursor ion beam, which may consist of either positive or negative ions. Considering a hydrogen beam, the most significant interaction between the beam and the plasma are charge exchange, Equation 1.8, and ionization due to collision with ions, Equation 1.9, and electrons Equation 1.10:

$$\mathrm{H}_{\mathrm{beam}} + \mathrm{H}^{+}_{\mathrm{plasma}} \rightarrow \mathrm{H}^{+}_{\mathrm{beam}} + \mathrm{H}_{\mathrm{plasma}} \tag{1.8}$$

$$\mathrm{H}_{\mathrm{beam}} + \mathrm{H}^{+}_{\mathrm{plasma}} \rightarrow \mathrm{H}^{+}_{\mathrm{beam}} + \mathrm{H}^{+}_{\mathrm{plasma}} + \mathrm{e}^{-} \tag{1.9}$$

$$\mathrm{H}_{\mathrm{beam}} + \mathrm{e}^{-} \rightarrow \mathrm{H}^{+}_{\mathrm{beam}} + 2\mathrm{e}^{-} \tag{1.10}$$

The intensity of the beam, denoted as I, depends on both the penetration depth x, and the initial beam intensity I_0:

$$I = I_0 e^{x/\lambda} \tag{1.11}$$

where λ is

$$\lambda = n\left(\sigma_{cx} + \sigma_i + \frac{\langle \sigma_e v_e \rangle}{v_{beam}}\right) \tag{1.12}$$

where σ_{cx} and $\sigma_{i,e}$ are the cross-section for charge exchange and for the ionization of the ions and of the electrons, $\langle \sigma_e v_e \rangle$ is the reaction rate of the collisions with electrons and n is the density. This approach enables the determination of an energy range that permits the beam to enter the plasma and deliver power to its center. To achieve adequate penetration depth of the beam into the plasma, the beam energy needs to be on the order of hundreds of keV. For ITER, a beam energy of approximately 1 MeV is mandated [10]. This is necessary to ensure highly efficient non-inductive current drive with high-energy particles (as current drive efficiency rises with particle energy) and to provide 33 MW of heating power through two heating beamlines.

The main elements of an NBI system include:

- Ion source, it is the device where the ions of the gas used for experimentation are generated by the cold plasma.
- Acceleration stage, it is the stage in which the ions generated in the source are accelerated by appropriately polarized grids.
- Neutralization chamber, it is the stage in which the ion beam, interacting with low-pressure gas, is neutralized, generating a beam almost entirely composed of neutrals.
- Residual Ion Dump (RID), it is the stage in which the residual ions are removed from the beam through a magnetic field or electrostatic field (the latter in the case of ITER), generating a beam consisting of only neutral particles.

In Figure 1.7, a typical diagram of NBI is presented, where the four distinct parts that compose it are delineated.

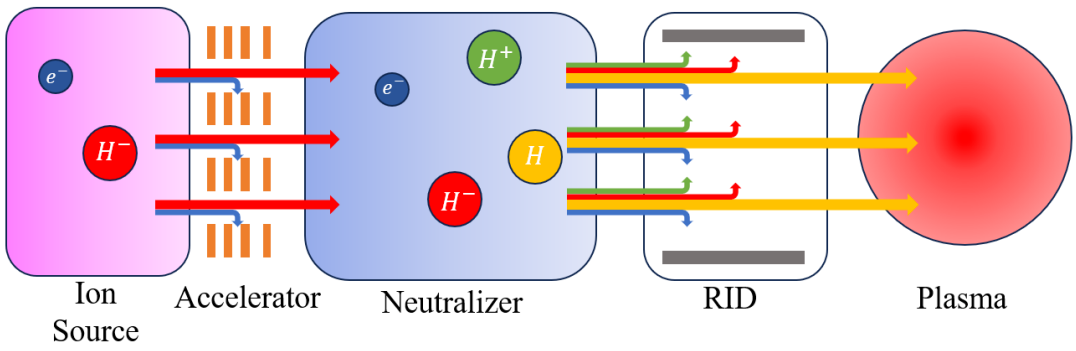

Figure 1.7: Scheme of a neutral Beam Injector.

The neutralizer is the most critical stage of the system, and its efficiency determines the efficiency of the entire beam generation line. The efficiency is different for positive and negative beams: the efficiency of neutralizing positive ions decreases with increasing energy. However, for negative ions, it consistently maintains acceptable values, approximately around 60%, as depicted in Figure 1.8. Due to this reasons, the ITER NBI system regards the negative ion source as its benchmark source.

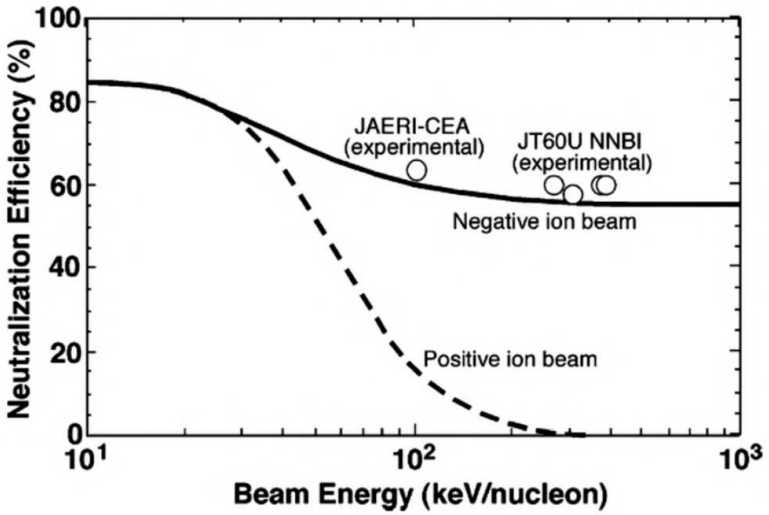

Figure 1.8: Neutralization efficiency of positive and negative ions as a function of kinetic energy [11].

Some specific requirements for ITER neutral beam injector are reported in Table 1.2.

Parameter	**Hydrogen**	**Deuterium**
Power delivered to ITER	16.5 MW	16.5 MW
Extraction area	0.2 m^2	0.2 m^2
Extracted current density	$\geq$ 329 A/m^2	$\geq$ 286 A/m^2
Accelerated current	$\geq$ 49 A	$\geq$ 40 A
Accelerated ion energy	0.87 MeV	1 MeV
Ratio of co-extracted electrons to ions	< 1	< 1
Source pressure	0.3 Pa	0.3 Pa
Beam divergence	$\leq$ 7 mrad	$\leq$ 7 mrad
Beam inhomogeneity	$< 10\%$	$< 10\%$

Table 1.2: Main parameters of one ITER NBI. [12], [9].

To attain this objective, various facilities worldwide are delving into the diverse aspects and challenges associated with fusion, all sharing the same ultimate aim.

1.4.2 Neutral Beam Test Facility (NBTF)

The Neutral Beam Test Facility (NBTF), located at the Consorzio RFX, in Padua, aims to investigate and test the full-scale prototype of the negative ion source of ITER. The goal is to study configurations, issues, and new engineering implementations in order to improve the performance of the source before it is connected to the complete facility in Cadarache. To achieve this purpose, currently, there are three experiments in place:

- MITICA: (**M**egavolt **ITER** **I**njector and **C**oncept **A**dvancement), is the full scale prototype of the NBI that will be installed on ITER. Actually is still under construction.
- SPIDER : (**S**ource for the **P**roduction of **I**ons of **D**euterium **E**xtracted from a **R**F plasma) is the full scale prototype of the negative ion source that will be installed on ITER. It has been operating since 2018 and currently is in a phase of improvement and optimization.
- MINION: (**M**agnetized **I**CP for **N**egative **I**on **O**peration in **N**BI) consist of a single RF driver, the same of the SPIDER's RF driver, its purpose is to optimize the configuration of the magnets surrounding the RF coil that will be installed around the SPIDER drivers.

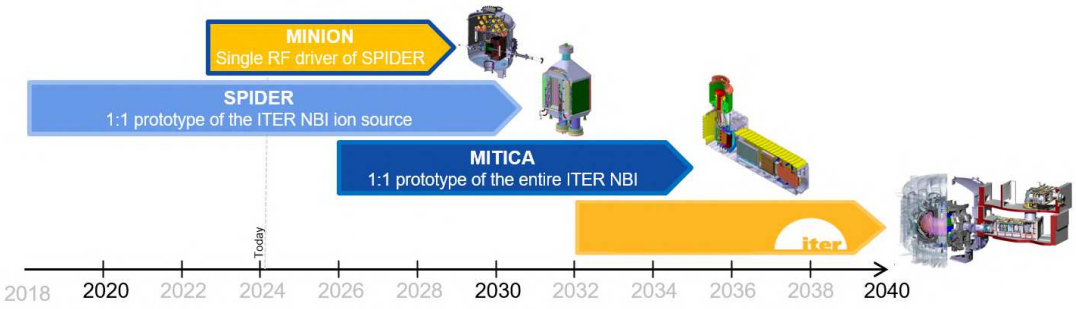

Figure 1.9: Timeline of the ITER project.

1.5 Aim of the thesis

This work is focused on commissioning activities on the MINION experiments, first measurements and on the development of a model to study and optimize the RF inductive coupling. The experimentation in MINION here described is relevant for SPIDER, due to the flexibility and intrinsic fast implementation of technological solutions to be evaluated thank to the extended suite of diagnostics installed.

The first part of the thesis is therefore dedicated to the commissioning phase of the facility, analyzing the main activities carried out for the commissioning of individual plants. In particular, simplified models have been developed to study gas calibration and ignition filament, and electrical measurements along the RF transmission line have been conducted to characterize the system and load. Furthermore, during the this phase, multiple diagnostics used in plasma characterization were installed and tested, for which I provided assistance in commissioning. Specifically, I supervised and managed the visible light cameras used as a plasma diagnostic tool within the expansion chamber.

The focus then shifts to the study of the magnetic configurations tested during the experimental phase through models and simulations aimed at understanding the pros and cons aspects of the proposed configurations. Particular attention has been dedicated to the effects of the magnetic field produced by cusp magnets and the filter field.

The last part of the thesis is dedicated to a specific study of the inductive coupling of the source through finite element simulations aimed at adequately modeling the plasma properties considering an axissymmetric model. Particular focus was placed on the sensitivity study of the model, considering how the main characteristic phenomena of the plasma distribution contribute to the inductive coupling.

Chapter 2

Negative ion sources and diagnostics

In this chapter, the main characteristics of ion sources will be presented, focusing particularly on the key differences between arc filament sources and RF-based sources. Subsequently, the main physical processes involved in the production of negative ions in RF-based source systems will be presented. The final section is centered around the SPIDER experiment to better understand the context in which the MINION experiment unfolds.

2.1 Negative ion sources

As previously outlined in *Chapter 1*, in order to achieve a neutral beam capable of heating the plasma to the high energies needed for the ITER project, the precursor beam must consist of negative ions. Hence, it is crucial to characterize the operation of the source and enhance its technical limits to meet the requirements of ITER NBI.

In general, an ion source applied in the field of fusion is formed by a magnetically confined expansion chamber, inside which a cold hydrogen or deuterium plasma is generated through the ionization of gas at low pressure. The magnetic confinement of the chamber is achieved by permanent magnets placed outside the chamber or by a magnetic filter field generated through a solenoidal electrical circuit, allowing control over the field intensity at the expense of a more complex engineering implementation.

To sustain the discharge, it is necessary for the electron temperature of the plasma to remain high throughout the discharge. To this end, there are two main types of ion sources based on two distinct principles of ion generation:

- Filament-based source, where electrons are acquired through thermionic emission from suitably heated filaments;
- RadioFrequency-based source: where an oscillating magnetic field produced by

an RF coil is used to excite and heat the electrons.

2.1.1 Filament-based source

The initial focus on developing negative hydrogen ion sources for ITER NBI was centered on filament arc sources, as outlined in the ITER reference design in 2002 [13].

An arc filament source is one of the relatively simpler setups for producing plasma. Essentially, plasma is generated inside a low-pressure chamber, where electron emission from a set of tungsten filaments, negatively polarized with respect to the chamber, ionizes a rarefied gas. In the heated conductor, lattice electrons are highly energetic, and the probability that some of them surpass the extraction potential becomes significant. The primary thermionic emission of electrons, accelerated by the filament's polarization relative to the chamber, ionizes the low-pressure gas, producing plasma [14]. This phenomenon, defined as *thermionic emission*, is qualitatively described by Richardson's law, Equation 2.1,:

$$j = AT^2 exp\left[-\frac{e\phi}{k_B T}\right] \tag{2.1}$$

where j is the maximum current density for a given experimental setup, A, expressed in [$Am^{-2}K^{-2}$], is a parameter that depends on the filament material, T is the absolute temperature, ϕ is work function of the filament material. In Figure 2.1 is presented a typical setup for a filament-based plasma source.

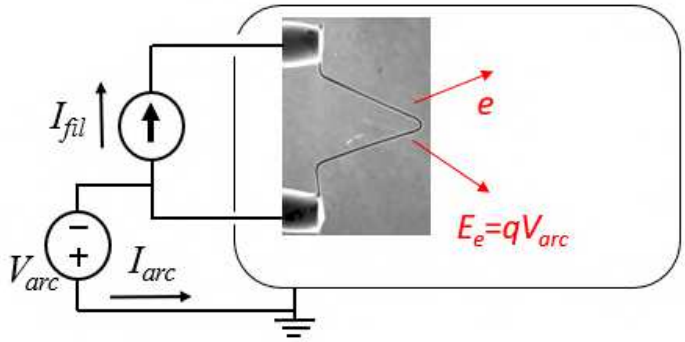

Figure 2.1: Experimental setup for a filament based source, I_{fil} is the filament current and V_{arc} is the polarization voltage between filament and chamber.

This method of plasma production, however, has various negative aspects. The main problem lies in the wear of the filament due to sputtering phenomena, leading to constant maintenance. Estimates required replacing the filament every six months [15]. Additionally, using the filament as an extraction source leads to the generation of impurities, as it is directly exposed to the plasma and involves a significant energy

consumption, requiring the filament to be brought to temperatures of approximately $2000 - 3000$K.

Considering this issue, the RF-driven negative ion sources, which have been initially developed at Max Planck Institute for Plasma Physics (IPP) at Garching, were proposed as an alternative.

2.2 RF source

In an RF source, ionization energy is induced through an oscillating electric field produced by an external coil that wraps around the driver. Subsequently, accelerated electrons lead to gas ionization and plasma formation. This system can be simplified an electrical transformer. The primary circuit consists of the coil where the oscillating current flows, generating an oscillating field that impacts the plasma, considered as the secondary circuit.

Compared to filament-based sources, this type of source offers significant advantages. Firstly, it requires minimal maintenance as there is no filament, or at least the filament is not the means of sustaining the plasma (typically, a filament is used as a means to initiate the discharge). Secondly, since cesium is necessary to enhance source performance, cesium consumption in RF sources is reduced compared to filament-based sources because there are no filament impurities produced during operations that can burn the cesium deposited on the chamber walls. Moreover, the thermal inertia of the filament slows down the arc response to current variations, whereas in RF sources, the plasma response to injected power variations is significantly faster.

This series of advantages has gradually led ITER to abandon the project of using an arc-based filament source and since 2007, the RF source has served as the reference design for the ITER NBI source [16].

2.2.1 The driver and plasma generation

Figure 2.2 shows a general scheme of a RF source.

In RF sources, the plasma is generated in a specific zone called *driver* by the energy produced through the coil that surrounds it. The driver consists of an alumina or quartz cylinder capable of isolating the internal layers of the driver from the external coil. As long as alternating current flows through the coil, it induces a field into the plasma. In order to protect the alumina or quartz layer from the influence of the plasma, there is a Faraday shield positioned in the inner layer that directly faces the plasma, constructed from electrodeposited copper. The Faraday shield serves not only to safeguard the wall from sputtering phenomena and from the heat load of the plasma, but also to prevent

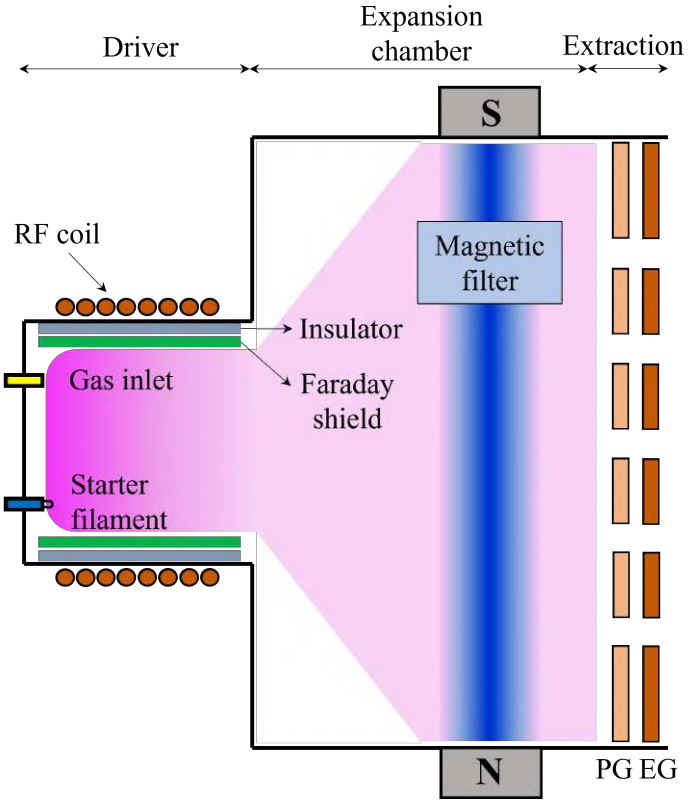

Figure 2.2: Schematic view of a RF negative ion source.

capacitive coupling between the coil and the plasma. This way, a purely inductive coupling is established between the two materials, allowing for the precise design of the matching frequency to achieve optimal power coupling between the power supplied by the generator, and the power absorbed by the plasma.

The plasma-facing side of the driver back cover, is a water-cooled molibdenum-coated Copper element. From the driver backplate auxiliary systems are fixed, such as gas injection, starter filaments, Faraday shield cooling, diagnostics, and the permanent magnets for plasma confinement on the inside [17]. The Figure 2.3 shows the design of the driver.

As shown in the figure, there is also a starting filament. This is necessary during the discharge initiation phase to generate primary electrons, which are then accelerated by the induced electric field. When the plasma density increases and electrons are heated, new plasma particles are generated from the impact of electrons with the gas, and the process becomes self-sustaining. At this stage, power is cut off to the filament to preserve its wear and tear.

More specifically, the coil is powered by an RF generator capable of delivering power P_{inj} up to 100 kW. Not all the power supplied by the generator, however, is coupled with the plasma. It is necessary to consider the losses generated by the trans-

mission line, especially from the resistive elements of the RF matching network and the driver itself. The power actually absorbed by the plasma can be defined as:

$$P_{abs} = P_{inj} - R_{loss} I_{rms}^2 = \eta P_{inj} \tag{2.2}$$

where R_{loss} is the effective resistance, I_{rms} is the root mean square of the induced current and η can be considered as the coupling efficiency.

It is necessary to emphasize that these losses are by no means negligible. For an RF inductively coupled plasma (ICP) source, approximately 40% of the power supplied by the RF generator is dissipated through the resistive components of the driver, and about 74% of this power is absorbed by the Faraday shield due to eddy currents [18], [19]. The majority of the remaining dissipated power occurs through the Joule heating effect, which warms the RF coil. Significant engineering research is therefore conducted to reduce these losses, both by exploring innovative designs for constructing the Faraday shield, especially regarding the shape of the shield's slit [20], and by seeking methods to magnetically confine the plasma within the driver. This latter alternative forms the basis of the research conducted with the MINION experiment and will be extensively discussed in the following chapters of this thesis.

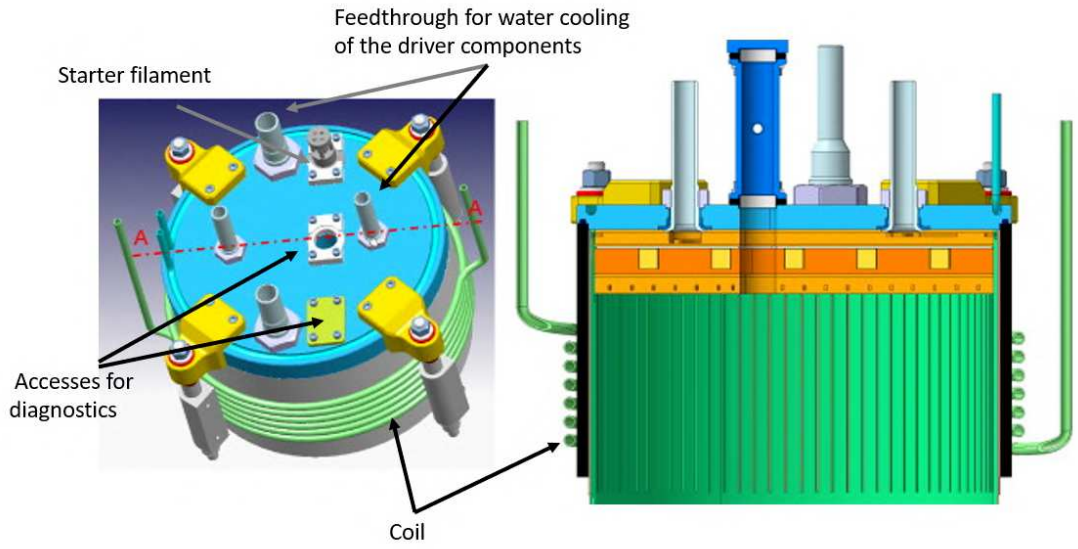

Figure 2.3: View of the drivers for the ion source of the SPIDER test facility.

The current generated by the generator powering the RF coil oscillates at a frequency, v_{rf} of approximately 1 MHz, and the induced field oscillates at the same frequency. This frequency choice is dictated by the need for the field to excite electrons even in the very early stages of the discharge when the plasma density and electron temperature are still very low.

2.2.2 Production of negative hydrogen ions

The driver is directly connected to the expansion chamber, inside which the plasma produced in the driver flows. In this volume, on one side, there is plasma expansion due to a density gradient, and on the other side, due to the magnetic field parallel to the plasma grid, the electron temperature decreases. The temperature T_e typically decreases from about 10 eV inside the driver to about 2 eV in the expansion chamber.

To achieve the maximum performance of the source, the expansion of the plasma should be uniform. In reality, this expansion is asymmetric due to phenomena related to drift motion in the plasma expansion region. In the driver region, additionally to the drift motions, plasma potential oscillation, causing the plasma to arrange with a higher density profile in a circular corona zone near the faraday shield lateral walls.

Inside the expansion chamber, the production ofnegative ions occurs through two main processes. In the first of these, called volume production, ions are generated through collisions in the bulk plasma. In the second, called surface production, ions are produced mainly by H or D atoms and positive ions impacting on a low work function surface.

Regarding volume production, low-temperature electrons are the cause of the formation of negative hydrogen ions through the phenomenon called "dissociative electron attachment." This phenomenon involves the production of negative ions through collisions between electrons and H_2 (or D_2) molecules vibrationally excited [21].

$$e^- + H_2 \Rightarrow H + H^- \tag{2.3}$$

However, there is also an opposing process leading to the destruction of ions called electron detachment, described by the following law:

$$e^- + H^- \Rightarrow e^- + H + e^- \tag{2.4}$$

Since the cross-sections of the two processes are comparable, this results in the easy destruction of negative ions by faster electrons.

For that reason, this single formation process is not sufficient to maintain the necessary flow of negative ions in ion sources for fusion purposes. In fact, these molecules constitute only about 3% of the entire population. This aspect is highly beneficial for neutralization but leads to stripping losses due to the fact that electrons within the grid system, following collisions with the background gas, are not fully accelerated. As seen in Figure 1.3, most losses occur between the PG and the EG due to the cross section. To limit these losses, it is necessary to keep the pressure as low as possible, hence the stringent limits required by ITER.

Concerning surface production, negative ions are produced by the interaction between the plasma and the metal surface of the expansion chamber. Specifically, the primary surface impacted by the plasma is the plasma grid (PG).

This grid separates the expansion chamber from the extraction zone. To enhance the surface production, caesium Cs in evaporated into the ion source by means of ovens and redistributed by the plasma. This helps reduce the surface work function and increases the probability of extraction [22], [23]. The primary reactions that define the production of ions are:

$$H^+ + e^-_{wall} \Rightarrow H^- \tag{2.5}$$

$$H^+ + e^-_{wall} \Rightarrow H \tag{2.6}$$

$$H + e^-_{wall} \Rightarrow H^- \tag{2.7}$$

To prevent the accumulation of cesium on the walls, they are maintained at a temperature of approximately $35-40°C$, which is higher than the cesium's melting temperature of 28°C. The plasma grid is also heated to elevated temperatures (around 100-150°C) to improve performance [24].

In addition to the electron detachment process, the other main re-neutralization processes include:

$$H^- + H \Rightarrow e^- + H_2 \tag{2.8}$$

$$H^- + H^+ \Rightarrow H + H \tag{2.9}$$

$$H^- + H_2 \Rightarrow H_2 + H + e^- \tag{2.10}$$

$$H^- + H_2^+ \Rightarrow H_2 + H \tag{2.11}$$

$$H^- + H_3^+ \Rightarrow H_2 + H_2 \tag{2.12}$$

In order to inhibit these processes of re-neutralisations and reduce the electron temperature, an additional magnetic field called *filter field* is used. This field, produced by permanent magnets and/or by a current flowing through the plasma grid, magnetizes the electrons which can traverse this region primarily through Coulomb collisions, and which have a cross-section that decreases as the speed increases, given by $\sigma(v) \simeq v^{-4}$ close the PG [25].

Through the employement of the filter field, the majority of high-energy electrons are consequently eliminated.

The additional electron of the negative ions is weakly bound (0.75 eV).

2.2.3 Extraction and acceleration stage

The extraction of the beam occurs in the region immediately following the expansion zone, called the extraction region.

Ions are extracted from the expansion chamber through several apertures positioned on the plasma grid (PG) by an electric field generated by the potential difference between the PG and the extraction grid (EG). The EG is positively polarized relative to the PG with a potential difference in the order of 10 kV to prevent excessive thermal loading on the components.

The last grid, which is called grounded grid GG, is present to accelerate to the negative ions to the nominal energy value. The totally supplies voltage U_{HV} is so divided in two contributions: extraction potential U_{ex} and acceleration potential U_{acc}, in detail, we can write:

$$U_{ex} = U_{EG} - U_{PG} \tag{2.13}$$

$$U_{acc} = U_{GG} - U_{EG} \tag{2.14}$$

$$U_{HV} = U_{ex} + U_{acc} \tag{2.15}$$

This dual acceleration phase is needed to eliminate co-extracted electrons before they are fully accelerated. The filtering of these electrons is done through a magnetic field generated by permanent magnets installed in the EG. This additional magnetic field primarily affects the motion of co-extracted electrons, with little influence on negative ions. In Figure 2.4, the complete system is depicted.

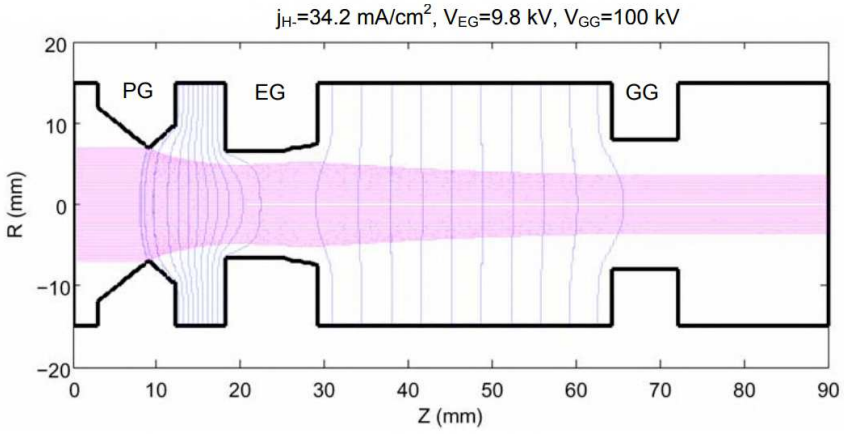

Figure 2.4: SLACCAD simulation of the beam optics: equipotential lines (blue) and particle trajectories (magenta) are estimated by integration of the Poisson's equation, potential were set $U_{ex} = 9.8$ V and $U_{HV} = 100$ kV. [26]

The transition layer between the plasma grid and the extraction grid has a convex profile and acts as an electrostatic lens for the negative ions, it is called *meniscus*. Even though the relationship between the shape of the meniscus and the parameters of the plasma is not yet entirely clear, [27], roughly speaking, it is possible to say that this concavity depends on the size of the aperture, the extracted voltage, and the general parameters of the plasma [28].

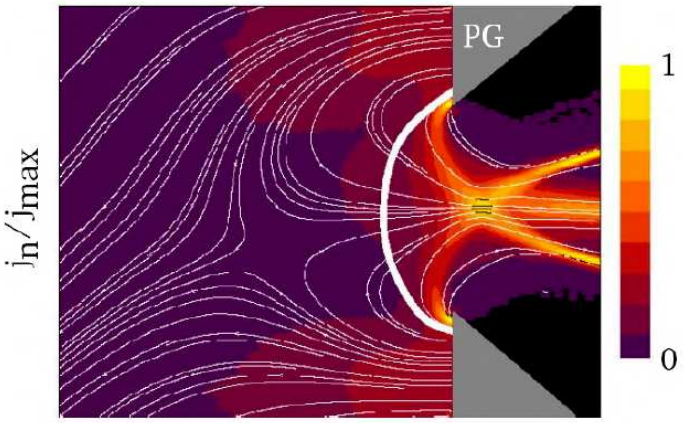

Figure 2.5: Plasma meniscus, highlighted by the white line, obtained with a 2D PIC-MCC simulation [29].

The quantity of ions that can be extracted through an applied electric field from an ideal planar electrode is directly proportional to the electric field applied between the electrodes and that resulting from the space charge present in the region between the electrodes. The density current that can be extracted is governed by the Child-Langmuir law [30]:

$$j_{ex} = \frac{4\varepsilon_0}{9}\sqrt{\frac{2Ze}{m}}\frac{U_{ex}^{3/2}}{d^2} \tag{2.16}$$

where j_{ex} is the extracted current density, m is the extracted ion, Z is the charge, d is the distance between the electrodes.

Considering circular apertures with a radius R, starting from the Equation 2.16, it is possible to define the maximum current extracted from each beamlet as:

$$I = \pi R^2 j_{ex} = \frac{4\pi\varepsilon_0}{9}\sqrt{\frac{2Ze}{m}}\frac{R^2}{d^2}U_{ex}^{3/2} = \mathbb{P}U^{3/2} \tag{2.17}$$

The parameter $\mathbb{P}$ is the beamlet *perveance*. It is possible to vary the perveance by adjusting the extraction voltage or the extracted current. Usually, U_{ex} is set by the experimental setup of the extraction system, whereas to increase the extracted current, one can act on increasing the RF power of the generator. However, if the extraction

voltage is too low, the extracted current may not reach the desired value despite the increase in power. The perveance $\mathbb{P}$ is a fundamental parameter in the study of beams, as the beam divergence reaches a minimum as a function of it.

2.3 SPIDER experiment

SPIDER, which began operations in 2018, is the full-scale prototype of the ITER's negative ion source. Its design, originated from studies conducted at the Max Planck Institute for Plasma Physics (IPP) at Garching, was developed through a collaboration between the Consorzio RFX and IPP. The entire negative ion source, including the plasma source and extractor, follows the same topological design that will be used in MITICA, the full-scale prototype of the Neutral Beam Injector (NBI), subsequently employed in ITER [31].

Spider consists of 8 drivers connected to a single expansion chamber, each capable of being powered with 100 kW at a frequency of 1 MHz. A schematic view of the source is depicted in the Figure 2.6, while the main design parameters are presented in the Table 2.1.

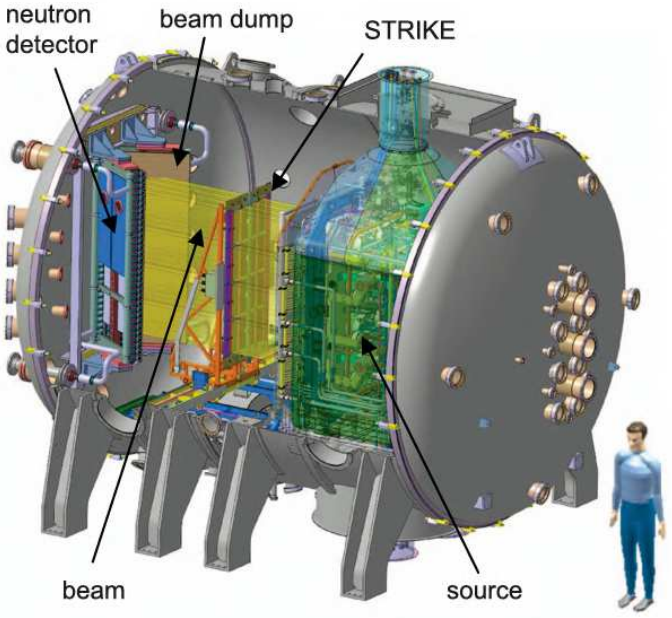

Figure 2.6: CAD model of SPIDER, with cut through view of the internal components [32]

The acceleration stage is composed of three multiaperture grids system, each grid of about 2 m^2 wide with 1280 apertures, arranged in 4×4 groups of 5×16 apertures.

The plasma grid (PG), separating the expansion chamber from the acceleration stage, is partially covered by a Bias Plate (BP), which consists of a grid of about 10

Parameter	**Hydrogen H_2**	**Deuterium D_2**
Beam energy	100 keV	
Beam current density	255 A/m^2	258 A/m^2
Beam pulse duration	3600 s	
Fraction of co-extracted electrons	< 0.5	< 1
Beam uniformity	$> 10\%$	
Maximum source filling pressure	0.3 Pa	
Divergence	< 7 mrad	

Table 2.1: SPIDER requirements

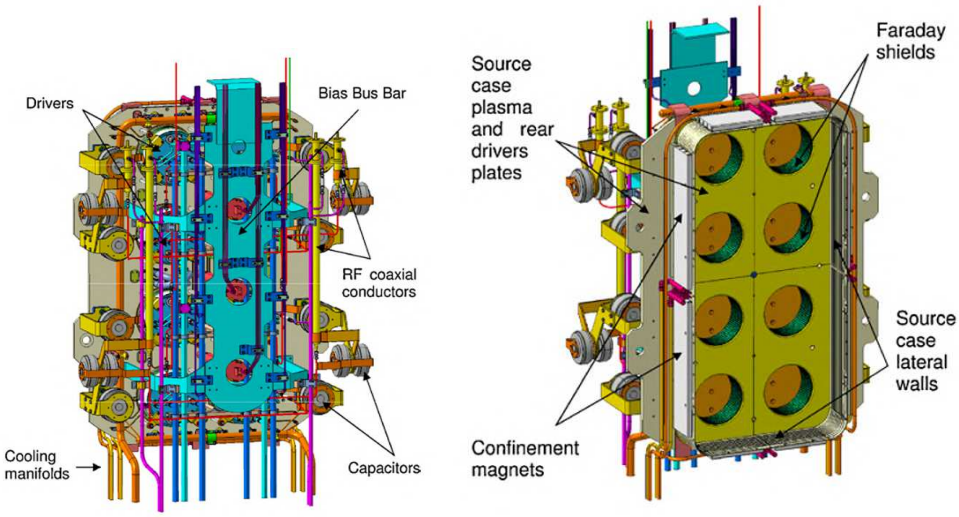

(a) (b)

Figure 2.7: Schematic view of the RF ion source (a) rear view, (b) front view [33].

.

mm. This plate can be used to compensate the electric field to maximize the extracted ion current and limit the co-extracted electron [34]. The extraction grid (EG) is biased at 12 kV with respect to the PG and is employed for ion extraction. Finally, the grounded grid (GG) serves as the final acceleration stage and can be polarized up to 100 kV relative to the plasma grid.

The filter magnetic field is generated by a current flowing vertically along the PG. Permanent magnets are installed on the source walls to reduce the plasma losses, thus improving the plasma confinement in the ion source. The remove the co-extracted electrons from the beam, sets of permanent magnets are placed on the Extraction Grid (EG). Permanent mags are installed on the Grounded Grid (GG) as well, to balance the negative ion trajectory perturbation introduced by the EG magnets. Additional bars are also present, through which a regulated current flows to achieve a magnetic field that

enhances the system's efficiency. A sketch of the three grids is shown in Figure 2.8.

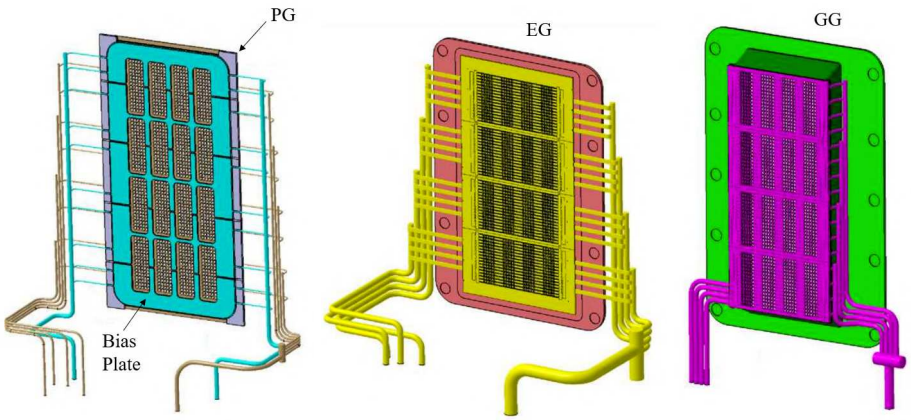

(a) (b) (c)

Figure 2.8: Schematic view of the three grid system with their cooling circuits: (a) plasma grid (PG) and bias plate, (b) extraction grid (EG), (c) grounded grid (GG) [35].

Chapter 3

The MINION test facility

In this chapter, the MINION experiment is introduced, and the commissioning phase of the experiment is described. The first part of the chapter analyzes the context in which the experiment originates and the purpose of the experimentation. Subsequently, the diagnostics used in the experiment are presented, which are relevant for comparison with the simulations discussed in the following chapters. Finally, there is an examination of the various facilities of the experiment, considering their commissioning.

3.1 MINION purpose and design

The experimental phase of SPIDER has highlighted the strengths and weaknesses or inefficiencies of the original design [36].

Firstly, as the full-scale prototype of ITER's negative ion source, SPIDER operates in vacuum. The experimental campaign has demonstrated the need to maintain an in-vessel pressure below 40 mPa to prevent discharges behind the RF drivers. To achieve this pressure, the pumping system, initially insufficient, is being augmented with non-evaporable getter (NEG) pumps [37], [38]. Additionally, to further improve the pressure, the apertures of the plasma grid are masked with a thin molybdenum layer closing the majority of the extraction apertures.

The main challenge, however, is related to the RF power applied to the drivers and the power effectively coupled with the plasma. On one hand, it has been found that the nominal power of 100 kW/driver is challenging to attain due to mutual interference from various resonant circuits. In this regard, the oscillators are being replaced with solid-state generators to ensure reaching the nominal power of the drivers. Nevertheless, the issue remains with coupling efficiency.

As discussed earlier, a significant portion of the RF power supply, approximately

40%, is dissipated by the resistive elements of the driver. The limited ability to couple power has generated problems concerning beam divergence and non-uniformity. The experimental campaign has indeed demonstrated that, on one hand, the ion temperature exceeds that predicted by simulation models [39], causing a minimum divergence of 12 mrad, which surpasses the ITER's target of 7 mrad.

Considering a linear relationship between the extracted current and RF power, a power of approximately 105 kW/driver would be required to achieve the current density mandated by ITER's stringent constraints, set at 355 A/m², view Table 1.2.

The experimental evidence highlighted the necessity to implement engineering and physical solutions to enhance the coupling efficiency between the power supplied to the coil and that absorbed by the plasma, aiming to increase the plasma density. With this primary objective, the MINION experiment is conceived.

This series of specific topics has been identified as the main aspects of study applied to the experiment [40]:

- Optimization studies on the RF driver setup (geometry, power loss) and optimization of the plasma expansion in the expansion chamber.
- Improvement of plasma confinement to reduce losses and increase plasma density.
- Enhanced comprehension of plasma physics in RF-based negative ion sources achieved by employing dedicated diagnostics and validating numerical models.
- Effect of the regeneration phase of NEG pumps relevant for future implementation on SPIDER, with particular attention to what happens when cesium is present in the source.
- Plasma ignition phase using RF solid-state generators, crucial to accelerate the startup phase of SPIDER with the new generation of RF generators.

For these purposes, specifically to enhance plasma density, new magnetic confinement configurations installed on the RF driver have been implemented and tested [41]. The basic idea is to improve electron temperature and plasma potential through enhanced confinement, aiming for more favorable conditions to extract colder negative ions. The goal is to identify the most efficient magnetic configuration and subsequently implement it in SPIDER and measure the beam parameters.

3.1.1 Design of the source

Let's now analyze the general design of the MINION test facility. The experiment involves a single RF driver, identical to one of the eight drivers used in the SPIDER

experiment, connected to an expansion chamber called the plasma box.

Like SPIDER and as required by the ITER experiment, MINION also operates in vacuum. The driver and the attached plasma box are therefore placed inside a cylindrical vacuum vessel. To facilitate assembly and disassembly operations, maintenance, and provide easy access to the driver, the vessel is divided into two halves. The upper half is fixed to a metal structure and has various flanges for connecting vacuum pumps, cryo and turbo, as well as pressure sensors to the chamber. The top vessel can also accommodate fixed internal metal structure for the future installation of non-evaporable getter (NEG) pumps. The lower part, on the other hand, has a motorized support allowing vertical and horizontal movements at ground level. The driver and the plasma box are connected to the lower part through a metal structure. The Figure 3.1 illustrates the schematic of the MINION experiment, including the vacuum vessel, the plasma source and some diagnostics.

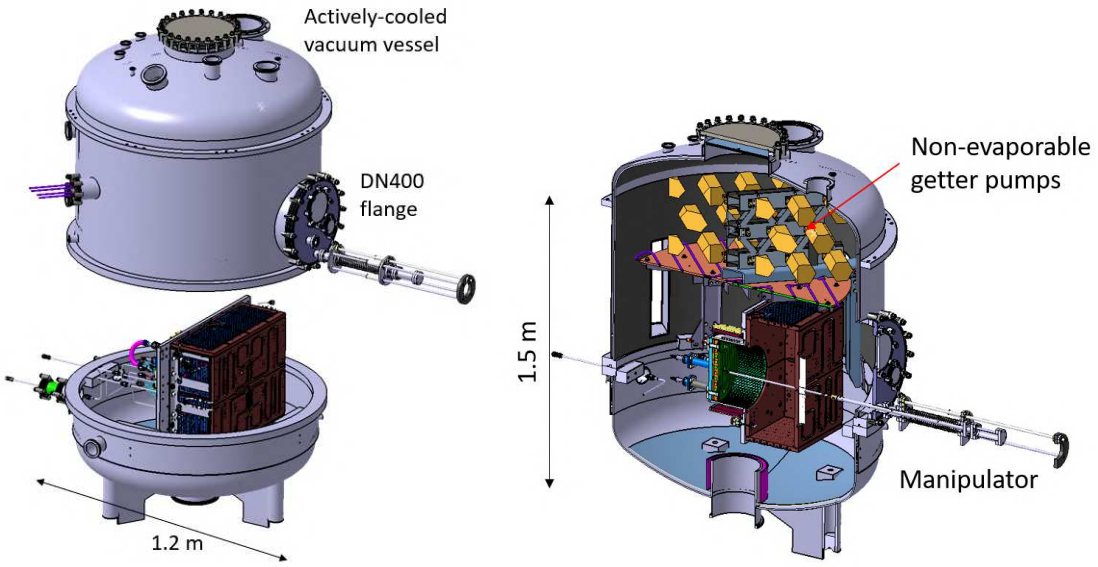

(a) (b)

Figure 3.1: Schematic of the MINION experiment, with vacuum vessel in grey and the plasma box in brown. In Figure (a), is mounted a flange DN400 used for diagnostic system. Figure (b) is a vertical section when the vessel is close, the manipulator is fully inserted in the source and the NEG system in presented on top.

The expansion chamber has dimensions of 22 cm in depth, 57 cm in width, and 50 cm in height. It is positioned to face the DN400 flange. This flange supports a manipulator, externally controllable, to which a Langmuir probe is attached. The Langmuir probe serves as a diagnostic tool to characterize the plasma and can reach the bottom of the driver along the plasma source axis.

Regarding the RF driver during this initial experimental phase, it has been equipped

with an electromagnetic shield (EMS) installed around the driver coil and equal to the one used in SPIDER but that has been brought closer to the driver, and a ferromagnetic shield to which permanent magnets have been fixed. This first phase tested magnetic configurations with 12 cusp magnets, 24 cusp magnets, and with the ferromagnetic shield without magnets. The results of these tests, both from a simulation and experimental perspective, will be extensively discussed in the following chapter. The Figure 3.2 illustrates the detailed view of the assembled RF driver and its individual components.

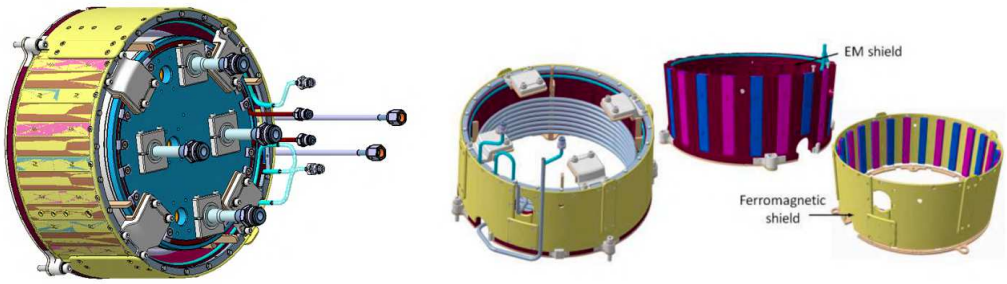

(a) (b)

Figure 3.2: Schematic view of the MINION's RF driver. (a) full view of the driver, (b) detailed view of the individual components including the ferromagnetic shield and magnets [41].

3.2 MINION diagnostic systems

Analyzing the generated plasma is essential in a fusion experiment. To provide a comprehensive characterization of the source in terms of efficiency and performance, various types of diagnostics have been installed on MINION. During the initial experimentation phase, only a portion of the diagnostic systems was installed. This section focuses on the main ones.

3.2.1 Langmuir probe

The efficiency of a plasma discharge can be defined by considering the plasma density achieved per unit of expended power. To obtain a good estimate of low-temperature plasma parameters, a Langmuir probe can be employed. The probe essentially consists of an electrode inserted into the plasma, polarized with respect to it, collecting ion and electron currents. From the collected current, an estimate of the plasma density, electron temperature, and plasma potential can be derived.

In applications of the probe within vacuum tube discharges, the plasma potential Φ_p, at the probe position, can be calculated by measuring the potential difference between the probe and one of the electrodes. However, this procedure results in a floating probe potential Φ_f that typically does not match the plasma potential. Considering an electrically neutral plasma where electron and ion densities are comparable, due to the higher thermal velocity of electrons, the floating probe initially attracts a higher electron current because electrons reach the probe faster than the heavier ions. Since the net current absorbed by the probe must be zero, the probe assumes a negative potential relative to the plasma. The collection of electrons is then decreased while that of ions is encouraged. This process leads to a floating potential that fluctuates to maintain a zero net absorbed current.

To solve the floating potential issue, typically the probe is polarized by applying a bias voltage V_b. The total current absorbed by the probe is determined by the contributions of both ion and electron currents $I_{tot} = A_{probe}(j^+ + j^-)$. A typical current-voltage characteristic for an ideal Langmuir probe is shown in Figure 3.3.

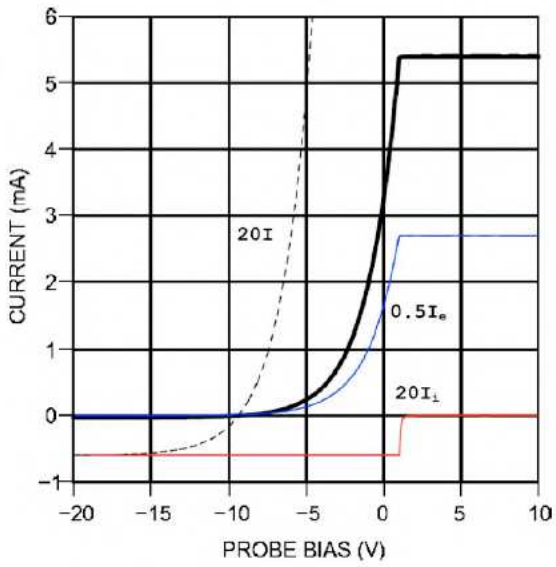

Figure 3.3: Ideal Langmuir probe current-voltage characteristic heavy line. The individual electron and ion currents that are used to construct the full characteristic are also shown. The dotted line is the full probe characteristic magnified by a factor of 20 so that the probe floating potential, V_f, that is the probe voltage where $I = 0$ can be easily determined [42].

When the bias voltage V_b is sufficiently negative compared to the plasma potential Φ_p, the probe collects the ion saturation current I_{iS}. Positive ions continue to be collected until the probe bias voltage reaches Φ_p, beyond which point ions begin to be repelled. For $V_b >> \Phi_p$, all ions are repelled, and ion current I_i goes to zero. Con-

sidering the Maxwellian distribution of temperature T_i, the dependence of ion current $I_i(V_b)$ can be expressed as:

$$I_i(V_b) = \begin{cases} -I_{iS}\, exp[e(\Phi_p - V_b)/k_B T_i], & \text{if } V_b \geq \Phi_p, \\ -I_{iS}, & \text{if } V_b < \Phi_p, \end{cases} \tag{3.1}$$

where k_B is the Boltzmann constant.

When $T_e >> T_i$ the ion saturation current is the Bohm ion current:

$$I_{iS} = I_{Bohm} = 0.6 e n_i \sqrt{\frac{k_B T_e}{m_i}} A_{probe} \tag{3.2}$$

where n_i is the ion density and m_i is the ion mass.

The fact that the ion current depends on the electron temperature implies the generation of a *sheath* zone around the negatively biased probe. The factor of 0.6 is necessary, instead, to account for the reduction in ion density in the *presheath*, where ions are accelerated up to the Bohm velocity.

For $V_b >> \Phi_p$, the probe collects the electron saturation current I_{eS}. For $V_b < \Phi_p$, electrons are partially repelled by the probe, and the electron current decreases exponentially with the increase in V_b. For $V_b << \Phi_p$, all electrons are repelled. The electron current I_e as a function of V_b can be expressed as:

$$I_e(V_b) = \begin{cases} I_{eS}\, exp[-e(\Phi_p - V_b)/k_B T_e], & \text{if } V_b \leq \Phi_p, \\ I_{eS}, & \text{if } V_b > \Phi_p, \end{cases} \tag{3.3}$$

The electron saturation current I_{eS} is given by:

$$I_{eS} = \frac{1}{4} e n_e v_{e,th} A_{probe}, \tag{3.4}$$

where n_e is the electron density, m_e is the electron mass and $v_{e,th}$ is the thermal electron velocity.

Taking into account the contributions of ion and electron currents, it is possible to derive the current-voltage characteristic (I-V), and its fitting is obtained with the following equation [43]:

$$I(V) = I_{sat}(1 + R(V_f - V)) \left(exp\left(\frac{V - V_f}{T_e} \right) - 1 \right) \tag{3.5}$$

where R accounts for the sheath expansion for $V < V_f$ and I_{sat} is the ion saturation current at V_f given by:

$$I_{sat} = e n \sqrt{\frac{e T_e}{m_i}} A_{probe} \tag{3.6}$$

where n is the plasma density at the sheath edge.

In the initial experimental phase, the MINION experiment was equipped with a mobile Langmuir probe mounted on a manipulator capable of measurements along the driver axis and across the entire expansion region. A sketch of the manipulator with the Langmuir probe used in the operations and its implementation is presented in Figure 3.4.

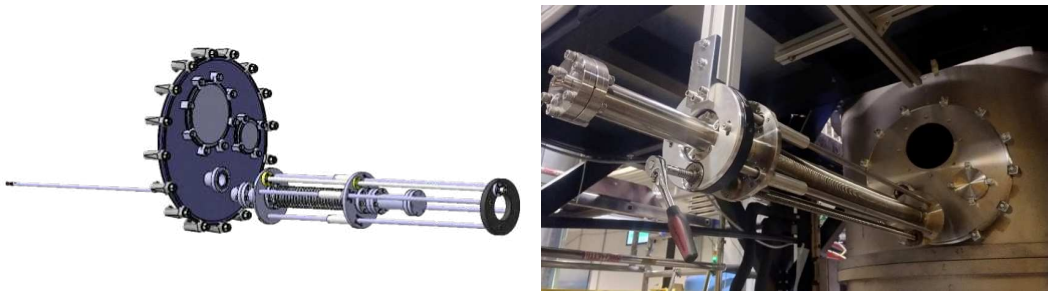

(a) (b)

Figure 3.4: (a) sketch of the manipulator with the Langmuir probe used in the operations, (b) manipulator connected to the MINION flange.

3.2.2 Optical Emission Spectroscopy (OES)

A wide range of plasma parameters can be extracted by studying the radiation emitted from the plasma source, such as electron density and temperature, cesium density, and neutral hydrogen density [44].

The transition of an electron from a higher energy state E_f to a lower energy state E_i results in the emission of a photon at frequency v:

$$E_f - E_i = hv \tag{3.7}$$

where $h = 6.626 \times 10^{-34}$ represent the Plank's constant.

Regarding hydrogen atoms, various emission lines have been tabulated based on the final orbit of the electrons. The main ones are listed in Table 3.1.

The electrons of hydrogen can change their orbit by interacting with a photon. Generally, there are three mechanisms for photon excitation and de-excitation: spontaneous emission, stimulated emission, and absorption. As for spontaneous emission, it occurs when an electron in a higher state transitions to a lower state, emitting a photon with energy equal to the difference in energy between the two states. The measurement of the probability of spontaneous emission for a process is estimated using the Einstein coefficients A_{if}. Regarding the second mechanism, stimulated emission occurs when there is an interaction between an electron in a higher state and a photon.

Series name	Line name	Initial orbit	Final orbit	λ [nm]
Lyman	L_{y_α}	2	1	121.6
	L_{y_β}	3		102.6
	$\vdots$	$\vdots$		$\vdots$
Balmer	H_α	3	2	656.3
	H_β	4		486.1
	H_γ	5		434.0
	$\vdots$	$\vdots$		$\vdots$
Paschen	P_α	4	3	1875
	P_β	5		1282
	$\vdots$	$\vdots$		$\vdots$

Table 3.1: Emission lines series in vacuum of atomic hydrogen [45].

The electron then falls to a lower state, emitting a photon with energy corresponding to the difference between the two states. The last process, absorption, occurs when an electron in a lower state transitions to a higher state by absorbing a photon with energy approximately equal to the difference between the two states considered. These three processes contribute to the generation of emitted radiation.

In an equilibrium plasma, each process is balanced by its reverse process. However, in low-density fusion plasmas, such as those discussed in this thesis, we instead refer to a non-equilibrium plasma because the electron temperatures differ from the ion temperatures. This temperature difference persists because in plasmas with medium to low densities, the dynamics are dominated by electrons. Specifically, processes of excitation and de-excitation due to electron collisions contribute significantly to the population and depopulation of excited states for different species. In addition to spontaneous emission and absorption processes, other processes, mainly related to electron density, can be considered. Population models are necessary to describe the excitation and de-excitation processes accurately.

Depending on the plasma density, there are three different population models:

- Corona model, used for plasmas with very low density $n_e \leq 10^{16}$ m^{-3};
- LTE model, the Local Thermodynamic Equilibrium (LTE) model, utilized for high-density plasmas $n_e \geq 10^{22}$ m^{-3};
- CR model: Collisional Radiative (CR) model, typically employed for plasmas with medium electron density. However, it can also serve as a good approximation for both the corona model and the LTE model.

To study the emitted light radiation, MINION is equipped with a mini-spectrometer *Hamamatsu* TM series C10082CAH with 1 nm resolution, capable to measure a spectrum between 350 and 850 nm [46]. To study the spectrum of rotational and vibrational molecules with high resolution, MINION is also equipped with a Czerny-Turner spectrometer with a spectral resolution of 0.05 nm that can operate between 350 and 1300 nm.

3.2.3 Additional diagnostics

In addition to these two main diagnostics, during the initial experimental phase, MINION was also equipped with the following additional diagnostics:

- Visible cameras: two surveillance cameras employed in two lines of sight to observe inside the expansion chamber. Specifically, these were positioned at two pre-defined access points in the plasma box to observe the inside of the expansion chamber from top to bottom and from left to right.
- Thermocouples: used to monitor the temperature of the cooling pipes by considering the temperature difference between the inlet and outlet of the cooling circuits. This difference is proportional to the power dissipated by the resistive components.
- Plasma Light Detection (PLD): this diagnostic is based on the response of photodiodes, utilized to determine plasma ignition and extinction, plasma dynamics, and the transition between capacitive coupling mode and inductive coupling mode.

In Figure 3.5, a sketch of the diagnostics used in Minion is shown along with their respective lines of sight.

3.3 MINION commissioning phase

In this section, the commissioning phase of the MINION experiment is presented. The various facilities required for the proper functioning of the system, their implementation, and the tests conducted to ensure that the various components of the system work correctly and are efficiently integrated will be discussed. In Figure 3.6, the physical implementation of the experiment is depicted with the vacuum vessel open, and the RF driver connected to the plasma box mounted at the bottom of the vessel. Some elements of the cooling and pumping system are also highlighted.

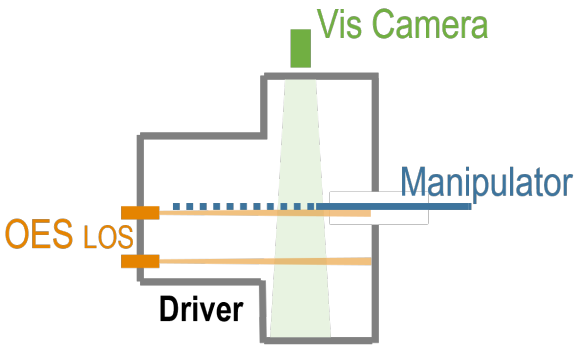

Figure 3.5: Sketch of the diagnostics used in MINION, detailing the manipulator with the Langmuir probe for axial measurements of plasma density, electronic temperature, and potential. Additionally, the visible cameras (only the top camera is shown in the figure) and the Optical Emission Spectroscopy (OES) with its two lines of sight.

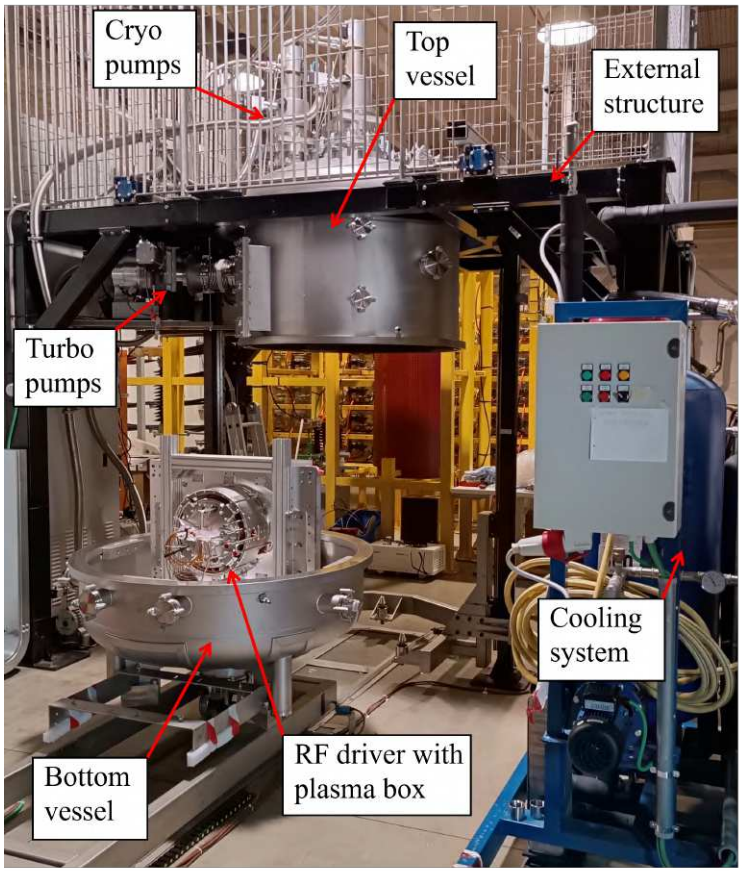

Figure 3.6: The MINION experiment with the vacuum vessel open, where the RF driver is positioned in the lower compartment connected to the plasma box. Some elements of the pumping and cooling systems are highlighted.

3.3.1 Vacuum and gas injection system

Let's begin the analysis by considering the vacuum system and gas injection system of MINION. Generally, when referring to the vacuum system, it encompasses a

complex of various elements: the actual vacuum chamber where the necessary vacuum is created to carry out the desired operations, the pumping system consisting of one or more pumps required to remove gases inside the chamber, pressure measurement devices, the set of various equipment needed to perform operations within the chamber (e.g., valves, manipulators, etc.), and the piping that connects the various components, allowing for the transport of gases.

We have already seen how, to meet the stringent pressure limits imposed by ITER, it is necessary to operate at chamber pressures of about $0.3 - 0.4$ Pa. To satisfy these requirements, the MINION pumping system is equipped with a series of vacuum pumps: two turbomolecular pumps MAGINTEGRA 1300, two cryogenic pumps COOLVAC 1.500 CL and a forevacuum screw pump ScrollVac 18 plus. During the second phase of MINION, the installation of 34 NEG pumps is planned in the dedicated structure located at the top of the vessel. As for the injection of hydrogen, a mass flow controller is used to inject gas through the back of the driver.

The Figure 3.7 depicts the schematic of the vacuum system, including the gas injection system used in MINION.

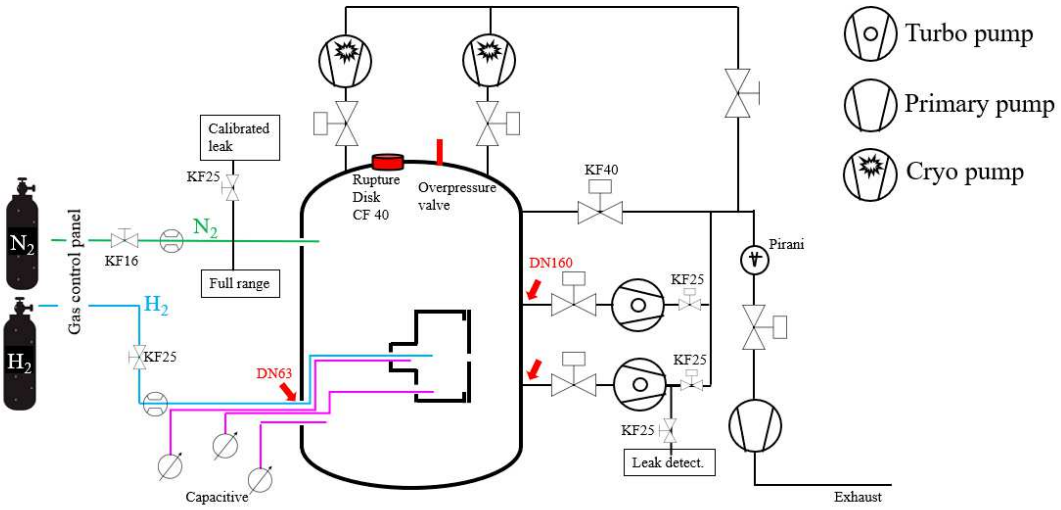

Figure 3.7: Vacuum and gas injection system of MINION. In detail, the pumping system is visible, specifying the vacuum pumps used, the implemented flanges and valves, the two gas lines, nitrogen and hydrogen, and the pressure measurement system.

Analytical estimation of conductance

Understanding the behavior of gas flow through a conduit is crucial for properly sizing the vacuum system, as it is closely related to the achievable final pressure and the system's evacuation time. To estimate the pressure behavior inside the plasma box,

essential for the correct ignition and characterization of the plasma, it is necessary to understand how the gas behaves and propagates from the expansion chamber to the vessel. In MINION, the vertical walls of the source are 2 mm away from the plasma grid facing the driver, a distance necessary as the side walls and the plasma grid can be independently polarized. Additionally, there is a hole in the front of the plasma grid through which the mobile Langmuir probe is inserted. To estimate the pressure behavior in the chamber with a specific gas flow, the conductance of the system has been previously studied.

The gas flow Q is defined as the quantity of gas passing through an isothermal plane per unit time, generally expressed as $p \cdot (dV/dt)$, where p is the pressure measured at the plane and dV/dt is the volume change per unit time through the plane [47]. Gas flow through a conduit occurs when there is a maintained pressure difference between the ends. In addition to the pressure gradient, the conduit's ability to allow gas passage is closely related to the geometry of the duct. The conduit's capacity to allow gas passage is defined through conductance, which is given by:

$$C = \frac{Q}{p_1 - p_2} \tag{3.8}$$

where $p_1 - p_2$ defines the pressure drop between the inlet and the outlet.

Let's first consider the conductance of the gaps between the side walls of the plasma box and the plasma grid, as this is the major contribution. In the molecular regime, it is possible to define conductance as a function only of the gap geometry and the gas nature, losing the dependence on the pressure gradient. The gas flow can be redefined as:

$$Q = \frac{1}{4} \cdot k_B T (n_1 - n_2) v_m \cdot A \tag{3.9}$$

where n_1 and n_2 are the molar densities, A is the area of the opening, and v_m is the arithmetic mean velocity given by:

$$v_m = \sqrt{\frac{8 k_B T}{\pi m}} \tag{3.10}$$

Introducing the corresponding pressures instead of molar densities, from the equation of ideal gas, the equation becomes:

$$Q = \frac{1}{4} \cdot (p_1 - p_2) \cdot A \tag{3.11}$$

Applying the definition of conductance, we obtain:

$$C_0 = \frac{1}{4} \cdot v_m \cdot A = \frac{1}{4} \cdot (8RT/\pi M)^{1/2} \cdot A \tag{3.12}$$

Since the gap dividing the plasma box and the plasma grid has a particular geometry with a constriction in the conduit, to obtain a more accurate estimate of the conductance, it is multiplied by a corrective factor defined as:

$$T = \frac{1 + ln\,(0.433 \cdot L/b + 1)}{L/b + 1} \tag{3.13}$$

where L and b are the weighted averages of the length and width of the gap.

Now let's move on to the analysis of the conductance of the plasma grid hole that allows the insertion of the Langmuir probe. To calculate the conductance of this channel, we start by considering the conductance of a long tube, i.e., one for which the length l is much greater than its characteristic dimensions, cross-sectional area A and diameter d. The conductance of a long tube can be calculated as:

$$C_0 = \frac{1}{12}\pi d^3 \frac{v_m}{l} \tag{3.14}$$

This relationship can be expressed more conveniently using the following units of measurement: cm for length, K for temperature, and grams g as follows:

$$C_0 = 3.81 d^3 (T/M)^{\frac{1}{2}}/l \tag{3.15}$$

The analysis just presented works for conduits with long tubes where it is assumed that the impedance due to the inlet opening can be neglected. If the tubes are short, meaning that the length of these tubes is less than approximately 20 times the tube diameter, it is necessary to also consider the resistance of the inlet opening by treating it as an impedance in series with that of the tube itself. The conductance of a short tube can be obtained by starting from that of a long tube and multiplying it by a corrective factor α. This factor is given by:

$$\alpha = \frac{1}{1 + \frac{3}{4}\frac{l}{d}} \tag{3.16}$$

where it can be observed that as $l >> d$, the correction factor α tends to 1, and therefore, the conductance of a short tube reduces to the conductance of a long tube.

For a more accurate analysis, it is possible to use Clausing's coefficient as the correction factor:

$$\alpha_{clausing} = \frac{15l/d + 12(l/d)^2}{20 + 38(l/d) + 12(l/d)^2} \tag{3.17}$$

The sum of the conductance of the slit and the conductance of the hole constitutes the impedance that allows calculating the flow between the plasma box and the vessel.

In Table 3.2, estimates of the conductances of the slit and the hole are provided,

considering operating conditions at a temperature of 300 K and using H_2 as the gas.

Parameter	**Slit**	**Hole**
C_0 (L/s)	9578.24	373.3
T	0.2239	-
$\alpha_{clausing}$	-	0.25
C (m^3/s)	0.2145	0.09332

Table 3.2: Conductance of the slit, between lateral wall of the plasma box and plasma grid, and of the hole.

Starting from the data sheets of the vacuum, turbo, and cryo pumps, it is possible to derive the pumping speed of the pumps under high vacuum conditions and in the presence of H_2. However, the nominal speed of the pumps S_{nom} is not directly applicable as it is necessary to consider that the pipelines connecting the pumps to the vessel introduce a resistance to the gas flow. This resistance can be calculated by means of an equivalent conductance applying the same formula in Equation 3.15 used in the calculation of conductance for long pipes.

Table 3.3 reports the characteristic data of pumping speeds, conductances, and the corresponding reduction in pumping speeds of the pumps.

Parameter	**Turbo pump**	**Cryo pump**
C(L/s)	3216.10	8749.27
S_{nom} (L/s)	940	2500
S_{eff} (L/s)	727.39	1944.41
S_{eff} (m^3/s)	0.7274	1.944

Table 3.3: Conductance and pumping speed of the pumps.

Assuming you want to work in the source with a pressure equal to 0.3 Pa, as per ITER specifications, and considering the flow expressed as the product of the source pressure and the total conductance between the source and the vessel, you obtain:

$$Q = C \cdot p_{source} = 0.0891(\text{Pa m}^3/\text{s}) \tag{3.18}$$

The gas flow can also be expressed as the effective pumping velocity for the pressure in the vessel, from which it is then possible to derive an estimate of the pressure in the vessel

$$p_{vessel} = \frac{Q}{S_{eff}} \tag{3.19}$$

Experimental estimation of conductance

Now let's consider the experimental estimation of conductance. The experimental setup allows for the determination of the gas flow rate, Q, introduced into the plasma box through a mass flow controller and the pressures in the source and in the vessel, measured by specific vacuum gauges. Using the measured flow rate and vessel pressure, the effective pumping velocity has been derived. The Table 3.4 presents the values obtained by studying different pumping configurations.

Parameter	**TMPs**	**Cryo$_A$ + TMPs**	**Cryo$_B$ + TMPs**	**Cryo$_{A+B}$ + TMPs**
S_{eff} (m^3/s)	1.3	2.9	2.7	4.1

Table 3.4: Effective pumping velocity estimated for various configurations of pumping.

From the tests conducted, it is possible to derive the following pumping speeds for individual pumps: $S_{TMP} = 1.3$ m^3/s, $S_{cryo_A} = 1.4 - 1.6$ m^3/s, $S_{cryo_B} = 1.2 - 1.4$ m^3/s. The problem is that turbo pumps have this pumping speed only for limited gas flow, approximately 30 sccm. Beyond these flows, the pressure in the vessel increases too much, and the pumping speed drops.

Starting from the experimental data obtained for pumping speed, gas flow, and source pressure, it is possible to estimate the conductance between the source and the vessel as $C = 0.47$ m^3/s. Thus, the actual conductance turns out to be approximately 30% higher than the estimated conductance. With a maximum gas flow of 100 sccm (limited by the mass flow controller used in the initial experiments), the maximum achievable source pressure is around 0.395 Pa, a limiting condition for plasma ignition. A possible way to increase the source pressure without increasing gas flow or reducing the pumping speed, is to reduce the conductance, at the expense of a slower system dynamics. Practically the conductance was reduced by partially closing the gap between the side walls of the plasma box grid with the kapton tape. Thanks to this operation, a conductance of approximately $C = 0.37$ m^3/s was achieved. Figure 3.8 shows the experimentally derived pumping speed estimate and the trends in the source pressure with respect to conductance.

In Figure 3.9, instead, the experimentally measured pressure at the source and in the vessel is shown as a function of the signal provided to the mass flow controller.

As can be seen from the graph, adjusting the conductance allows reaching a pressure of approximately 0.3 Pa using a gas flow rate of 60 sccm. With a gas flow rate of 100 sccm, a source pressure of about 0.5 Pa is achieved, as expected from the pressure trend observed in graph in Figure 3.8b. The vessel pressure follows the trend of the source pressure as expected.

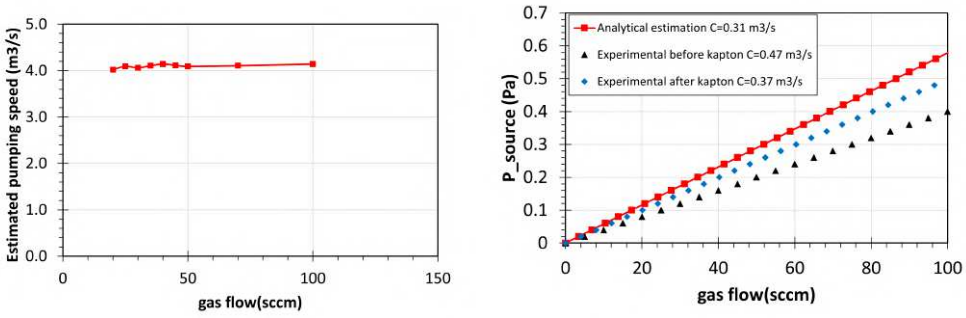

(a) (b)

Figure 3.8: (a) Experimentally estimated pumping speed based on gas flow and pressure measurements; (b) comparison between the trends of source pressure with varying conductance.

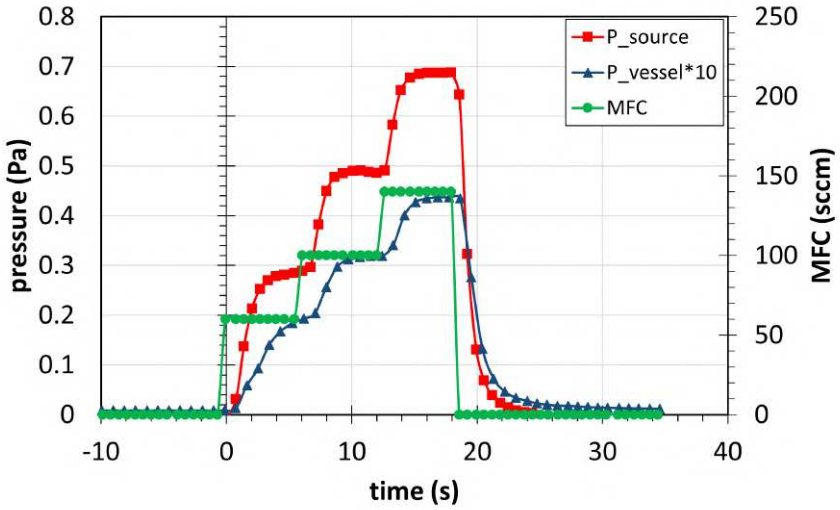

Figure 3.9: Pressure measurements at the source and in the vessel as the gas flow varies induced by the signal to the mass flow controller (MFC).

3.3.2 Cooling system

Now let's consider the cooling system of MINION. In the Figure 3.10, the entire cooling system is schematically shown, where various cooling lines are highlighted.

The cooling circuit consists of three branches. The first branch is intended to cool the Faraday shield lateral wall of the driver and the Faraday shield back plate. These two components are particularly prone to heating as they directly face the plasma and absorb, as previously seen, a significant percentage of power input from the RF coil. The second branch includes the two parts of the Electromagnetic Shield (EMS), the back cover and the rear driver plate. The last branch, on the other hand, includes the cooling of the plasma grid and the copper ring at the driver's exit on the back plate.

In the initial experimentation phase, only short-duration pulses were executed, so

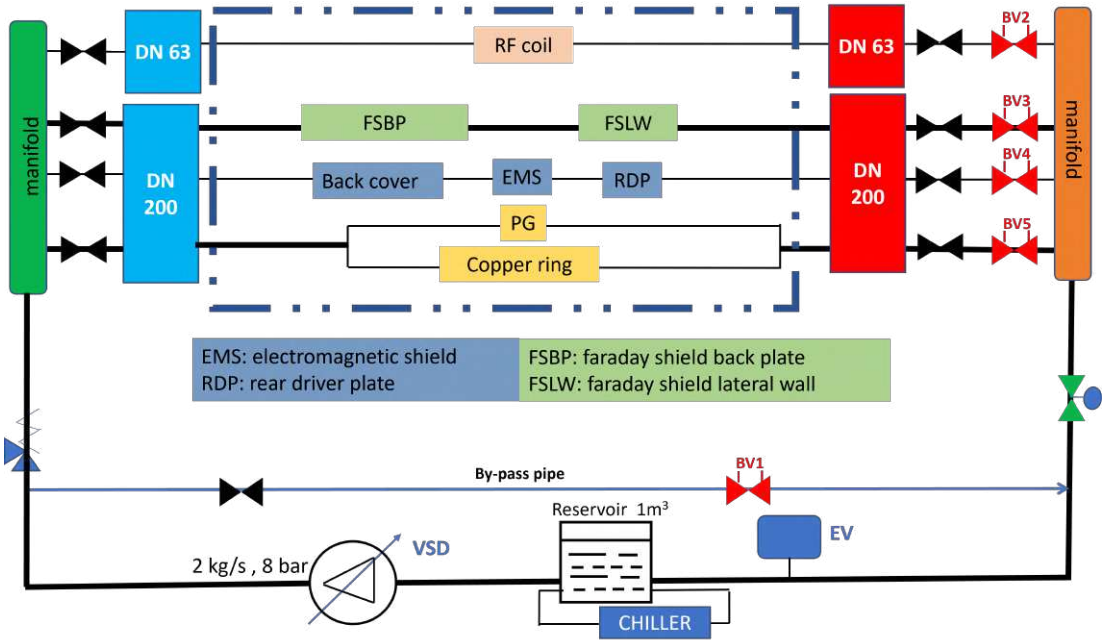

Figure 3.10: Cooling system of MINION, in detail the cooling lines are represented along with the various components of the system and their respective flow meters.

stainless steel panels inertially cooled were used as the side walls of the plasma box. The future implementation of the project involves using walls for the plasma box that are actively cooled to operate with longer pulses. All the other components of the driver, even in the initial experimentation phase, are equipped with direct cooling as they are either directly exposed to the plasma action or subjected to induced currents, leading to heating dynamics with much shorter time characteristics compared to those of the expansion chamber walls.

In order to have a control system for the cooling system, asameters have been applied to each branch of the cooling circuit, on the outlet branches. These instruments, remotely monitored, enable the measurement of water pressure on the inlet and outlet sides of the hydraulic circuits, allowing real-time detection of any malfunctions or leaks.

3.3.3 Ion Source Radio-Frequency Power Supply (ISRF)

The Ion Source Radio-Frequency Power Supply (ISRF) is the system that provides power to the coil windings around the RF driver used to supply the energy needed for plasma generation. As mentioned earlier, coupling the power supplied to the coil with the plasma is essential for optimal power transfer. To ensure this correct coupling, it is necessary to study the individual components that intervene between the power supply and the RF coil.

In general, the RF circuit consists of:

- A tetrode-based self-excited oscillator as an RF generator. MINION utilizes one of the power supplies from SPIDER capable of providing a power of 200 kW with a maximum efficiency of about 70% when coupled to a resistive load of 50 ohms.
- A coaxial transmission cable. It connects the RF generator to the matching network. In the case of MINION, this cable has a length of approximately 30 meters.
- A matching network. It consists of a group of capacitors connected in series or parallel and properly designed to ensure the best matching between the load required by the generator and the driver. In the case of MINION, the matching network is of the π-type.
- The driver RF represented by a load means of an ohmic-inductive impedance Z_D.

A sketch of the RF circuit is shown in Figure 3.11.

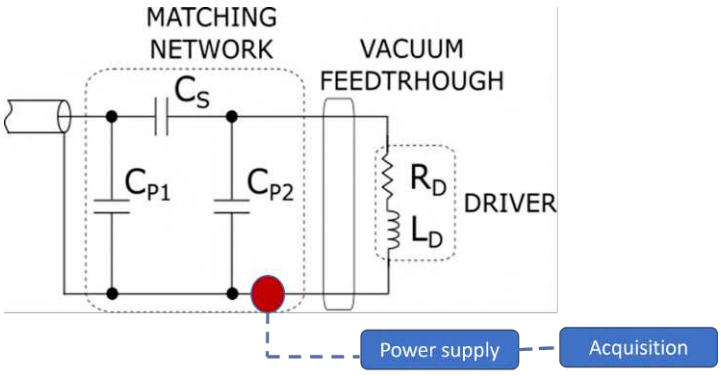

Figure 3.11: General design of the RF circuit with the spot indicated for measuring the voltage characteristics of the system.

The coaxial cable used to transmit the signal from the generator to the experimental site, the matching network, and the equivalent impedance of the RF driver constitute the load applied to the generator.

As mentioned, the generator exhibits maximum efficiency when connected to a resistive load of $50\,\Omega$. The coaxial cable used is designed to have a characteristic impedance of $50\,\Omega$. To achieve maximum power transmission, it is necessary to design the matching network to match the load of the RF driver, which is predominantly inductive, to the resistive load required by the generator in the presence of plasma discharge. The measured impedance of the RF driver required for the correct design of

the matching network is equal to $R_D = 720$ mΩ and $L_D = 8.8$ mH at $f = 1$ MHz. These characteristic parameters of the driver, however, change once the plasma is ignited in the driver. Indeed, the plasma results in an increase in resistive load as the resistance of the coil (and other components involved in the structure) is added to the resistance of the plasma. In contrast, the inductive contribution undergoes a decrease due to the shielding effects of the plasma. However, estimating the same parameters with the plasma ignited is very complex due to the fact that measurements are more affected by disturbances resulting from the high RF power involved.

The effects of the matching network are visible in Figure 3.12 and Figure 3.13, where magnitude and phase plots are shown between the RF oscillator and the matching network, and between the RF oscillator and the RF load.

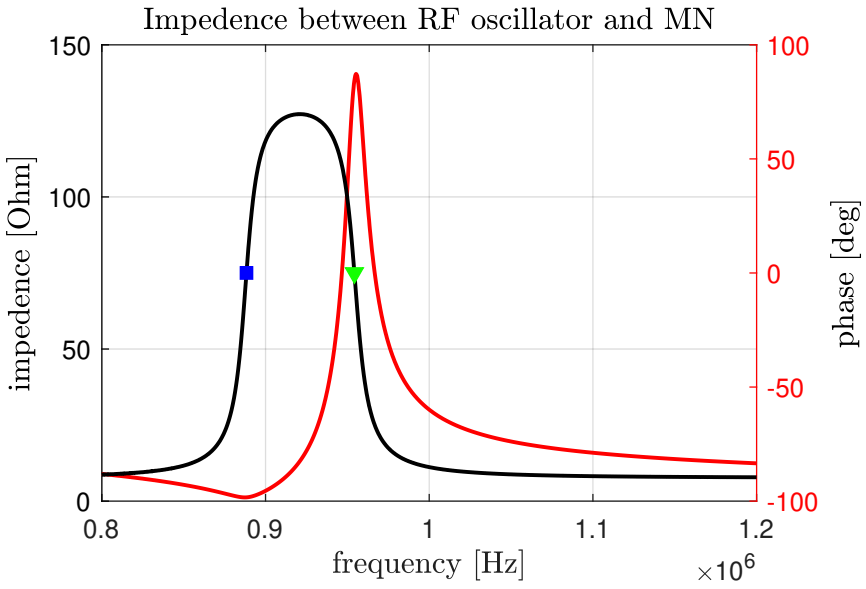

Figure 3.12: Measured impedance between RF oscillator and matching network.

Analyzing the trends of the impedance versus frequency, we observe how the RF load is resonant due to the capacitive nature of the matching network and the predominantly inductive nature of the RF driver.

The resonance and anti-resonance frequencies correspond to the passage through zero in the phase plot, as indicated by the markers in the graphs. By considering the load formed by only the coaxial cable and the matching network, a resonance is estimated at approximately 0.89 MHz, and the anti-resonance at 0.95 MHz. Considering instead the complete load formed also by the RF driver, a resonance is estimated at approximately 1.01 MHz and an anti-resonance at 1.06 MHz. Furthermore, considering the figure with the complete RF load, we see that resonance and anti-resonance do not correspond to the peaks, positive and negative, of the impedance. Indeed, resonance occurs shortly after the impedance peak, whereas anti-resonance occurs before

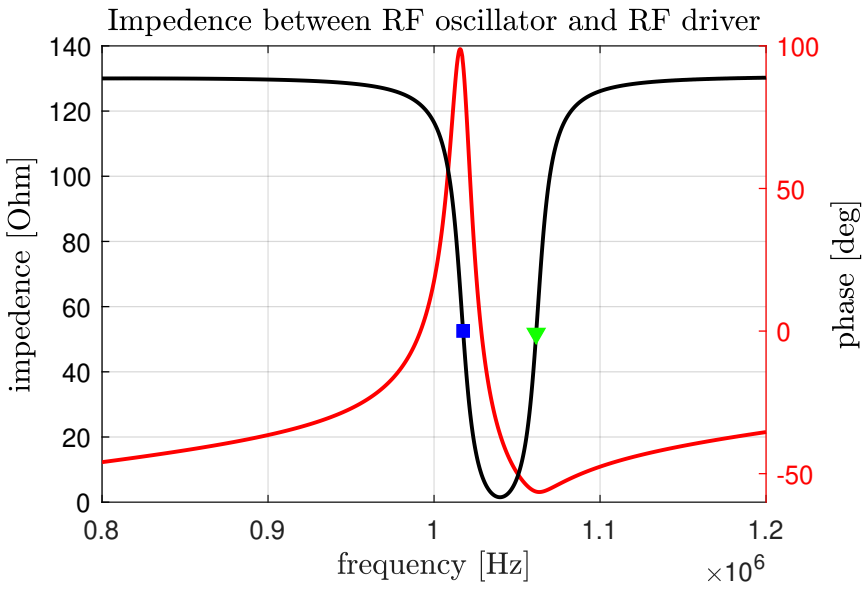

Figure 3.13: Measured impedance between RF oscillator and RF load.

the negative peak. Such behaviors are caused by damping phenomena of the resistive elements in the circuit.

To achieve maximum power transmission, it is necessary to have a perfect matching between the impedance of the RF driver and a purely resistive impedance of 50 Ohms. In this condition, the power reflection coefficient between the RF oscillator and the load is zero. Achieving this perfect matching is only possible within a limited range of frequencies compared to the operational frequency, and it can be attained by properly adjusting the capacitor network of the matching network. However, approaching the matching frequency can lead to instability phenomena due to the self-excitement of the RF oscillator, which can result in so-called *frequency flip* phenomena. These phenomena can cause undesired deviations from the desired operational frequency and can negatively impact the circuit performance. The Figure 3.14 shows the complete RF circuit used in MINION where the capacitors of the matching network have been properly adjusted to achieve the matching of the RF load.

3.3.4 Ion Source Filament Bias (ISFB)

The filament bias power supply (ISFB) is the system used to bias the starting filament relative to the source body. When discussing the operation of a negative ion RF source, we have seen that the only input of RF power through inductive coupling alone is not able to ignite the plasma due to the capacitive couplings established between the input power and the various driver components. To ignite the plasma, a starter filament is then used. MINION and SPIDER use tungsten filaments, which, when heated and

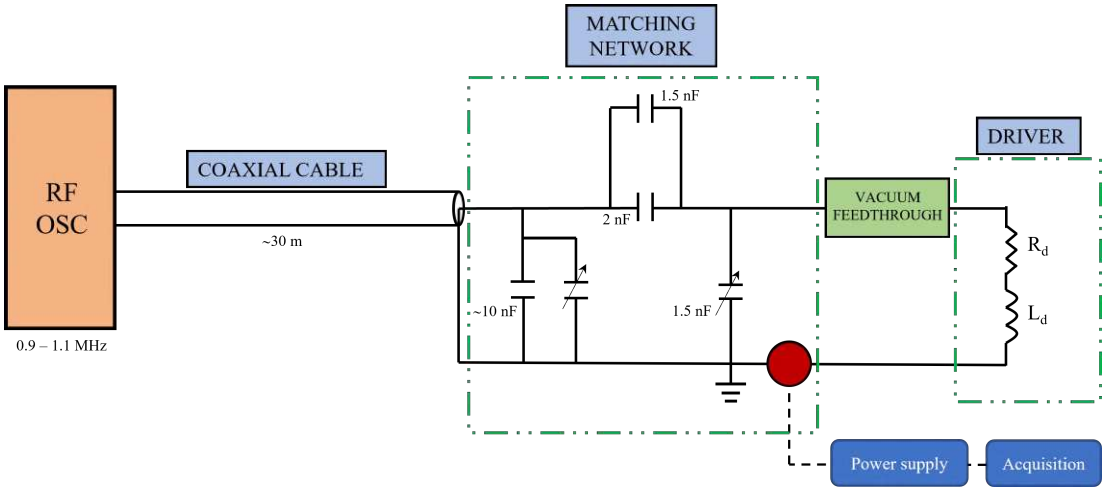

Figure 3.14: Complete RF circuit with MINION where the capacitors of the matching network have been adjusted to achieve the best matching.

biased relative to the source, provide the initial electrons needed to ignite the plasma. In Figure 3.15, a detail of the ignition filament used in MINION and its position relative to the driver is shown.

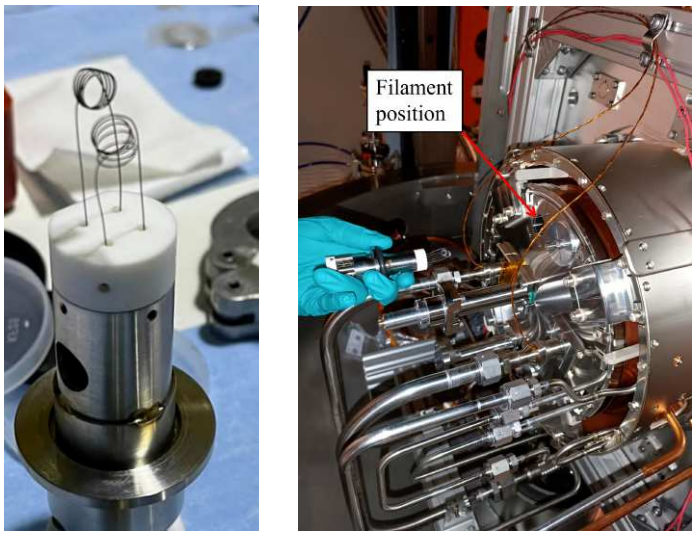

(a) (b)

Figure 3.15: (a) The ignition filament used in MINION, it is identical to one of the eight filaments used in SPIDER in each driver; (b) rear view of the driver indicating the position where the filament is inserted. The length of the support is such that it allows the filament to be fully exposed inside the driver.

In general, considering a conductor, it is possible to define the resistance of the conductor as:

$$R = \rho \frac{L}{\Sigma} \tag{3.20}$$

where L is the length of the conductor, Σ is the cross-sectional area, and ρ is the resistivity of the conductor. Therefore, the resistance is proportional to the length and inversely proportional to the area of the section. As for resistivity ρ, it represents the material's tendency to oppose the flow of current. It is a characteristic parameter for each material and, for metals, it increases linearly with the temperature of the conductor weighted by an empirical factor α for each material $\rho = \rho_0(1 + \alpha T)$.

The increase in temperature of the conductor results in an increase in kinetic energy of the lattice electrons. When a lattice electron collides with an ion, the particles are scattered with a direction of motion aligned with the electric field lines. The increase in kinetic energy of the particles translates into an increase in the conductor's temperature through the Joule effect and the heat exchange it entails. In a vacuum, this heat exchange is called radiation. The power of radiation follows Stefan-Boltzmann's law, according to which the total heat radiation emitted by a body is proportional to the fourth power of its absolute temperature. The complete relationship is given by:

$$P_R = \varepsilon S \sigma_B T^4 \tag{3.21}$$

where ε is the emissivity of the material, S is the exposed area and σ_B is the Stefan-Boltzmann constant.

When discussing filament-based plasma sources, we have seen how electrons can be extracted from the heated metal when an electric field is applied. This phenomenon, called *thermoionic emission*, is described by Richardson's law in Equation 2.1.

The maximum current that can flow through the hot filament is limited by the space charge produced by the emitted electrons at the cathode. This maximum current is quantified by the Child-Langmuir law, see Equation 2.16, and is reproduced by the effect where at a certain point, the increase in temperature of the filament causes no further increase in the current flowing through it.

Considering the condition in which the conductor is a cylindrical coaxial filament, and is polarized relative to a plane, the Child-Langmuir equation can be readapted to become:

$$j_{fil} = \frac{8\pi\varepsilon_0}{9}\sqrt{\frac{2e}{m}}\frac{V^{3/2}}{r\beta^2} \tag{3.22}$$

where j is the electron current per unit length along the axis, V is the voltage at the anode, r is the radius of the conductor at a certain point, and the characteristic factor β depends on the conductor and is determined by the ratio r/r_c, where r_c is the radius of the cathode.

Now let's consider the experimental characterization of the ignition filament used

in MINION. The table below shows the main geometric parameters of the filament and the main characteristic parameters of tungsten.

Parameter	**Value**
Diameter (m)	2.5×10^{-4}
Length (m)	0.178
Resistivity ρ (Ωm)	5.60×10^{-8}
Resistance-temperature coefficient β	0.94
Resistivity temperature coefficient α	3.309×10^{-3}
Tungsten emissivity ε	0.22

Table 3.5: Geometric and characteristic parameters of the tungsten filament.

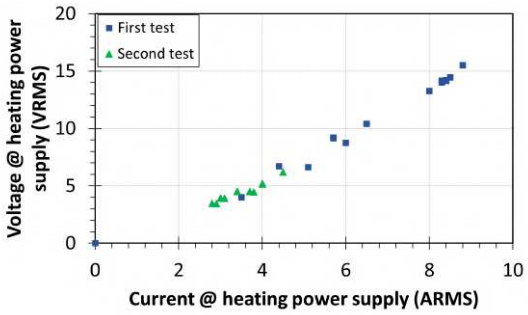

Figure 3.16: Filament current-voltage characteristic.

In Figure 3.16, the I-V curve is shown, which allows understanding the resistance of the filament starting from Ohm's law. The measured resistance actually corresponds to the sum of the resistance of the cable, used for voltage and current measurement, which can be considered constant, plus the effective resistance of the filament. We see that the behavior as the current increases is not perfectly linear. This is because, as seen, the resistance depends on the temperature of the filament in a nonlinear manner.

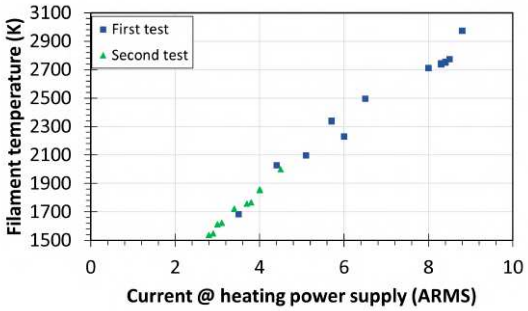

Figure 3.17: Filament current-temperature characteristic.

The graph in Figure 3.17, instead, represents the dependence of temperature on current. We observe that the temperature increase is nearly linear relative to the applied

current to the filament. However, we know that the temperature distribution along the filament is not uniform but follows a bell-shaped trend that increases in concavity with increasing applied current. In Figure 3.18, the trend of the current emitted by the filament is shown as a function of the bias voltage in accordance with the Child-Langmuir law.

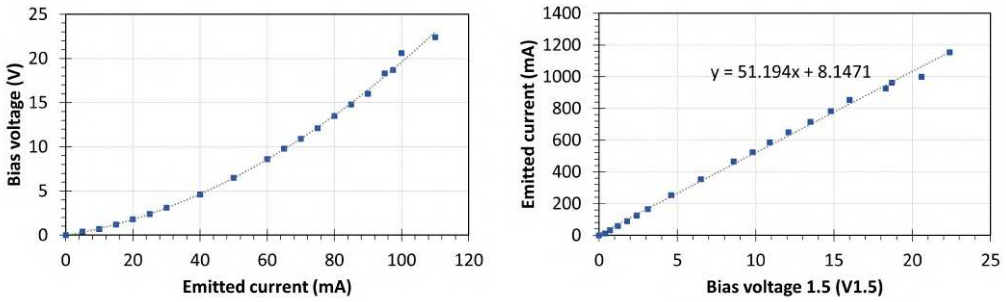

(a) (b)

Figure 3.18: (a) Filament emitted current - V_{bias} characteristic, (b) filament $V_{bias}^{\frac{3}{2}}$ - emitted current characteristic.

In detail, the graph on the right Figure 3.18b shows the proportional relationship between the current emitted by the filament and the power of $3/2$ of the bias voltage. As expected from the Child-Langmuir law, in Equation 3.22, this relationship is almost linear, as confirmed by the experimental data collected.

Chapter 4

Analysis of magnetic configurations

In this chapter, the configurations of the driver setup tested during the experimental phase will be presented. In the first part of the chapter, preliminary analyses conducted using the software *Ansys Maxwell* for magnetic simulations of the field intensity produced by cusp magnets installed around the driver will be reported. Subsequently, qualitative comparisons of plasma behavior in the expansion chamber will be presented by comparing the fields extracted from simulations with observations made by visible cameras. Finally, comparisons between different configurationsare done based on experimental data retrieved from the diagnostics installed in MINION. In Table 4.1 a summary of the analyzed configuration and the activities is shown.

Configurations			**Activities**			**Section**
Cusp magnets	**Fe shield**	**FF**	**Measurements**	**VC**	**LP**	
24	✓	✓	✓	✓	✓	4.1.1, 4.2.1, 4.3
12	✓	✓	✓	✓	x	4.1.2, 4.2.2
12	✓	1/2	x	✓	x	4.2.2
0	✓	✓	x	✓	✓	4.2.3, 4.3
0	x	✓	x	x	✓	4.3

Table 4.1: Summary of the configurations and the activities performed for them.

4.1 Cuspidal magnets configuration

As previously stated in section 3.1, the main issue encountered during the experimental campaign of SPIDER is that to achieve the current density required by the stringent parameters of ITER, with the original design of the ion source, a power of about 105 kW/driver would be necessary. Such a power requirement is too high to be

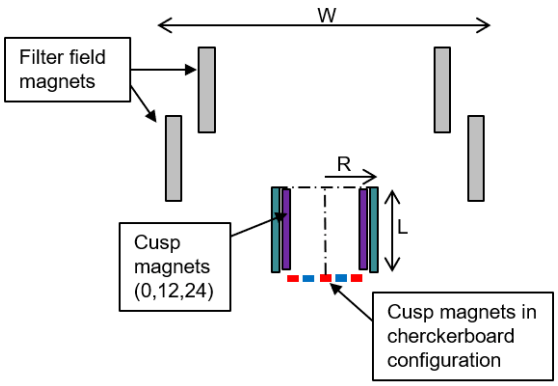

Figure 4.1: Magnetic configuration of the source as seen with a section along the y-z axis, L = 137.5 cm, L = 155 cm, W = 88 cm

sustained by a single driver. In order to increase the plasma density not by increasing power but through magnetic confinement various types of magnetic configurations have been studied and tested using permanent magnets installed around the driver in an iron shield. In this section, different configurations of cuspidal magnets will be analyzed by comparing the experimentally measured magnetic field with the magnetic field obtained through simulation.

4.1.1 24 cuspidal magnets

The first configuration tested, the one with 24 cuspidal magnets attached to the iron shield placed around the driver is here presented. In order to validate the *Ansys Maxwell* model used for studying the magnetic field magnitude and field lines, the calculated magnetic field profiles from the simulation were compared with those obtained experimentally. The experimental measurements of the magnetic field was conducted on a bench using a gaussmeter. The magnetic field measurements were taken during the commissioning phase of the experiment in order to obtain a preliminary measure of the generated field and a possible estimation of its effects in the source. The ferromagnetic shield with cuspidal permanent magnets was therefore assembled on a test bench and subjected to tests. In Figure 4.2, photos of the driver with the mounted shield and of the experimental setup used for the measurement are shown.

The magnets used are permanent magnets of size $70 \times 20 \times 10$ at SaCo with a relative magnetic permeability of about 1.1. They are positioned around the driver in pairs of two magnets, along the axial direction, and they are arranged on the circumference with alternating magnetic fields. Three radial profiles were measured and compared with the simulations: along the radius arranged at the lower curb, corresponding to the outermost region of the driver, at the midpoint of the axis, and at the upper curb,

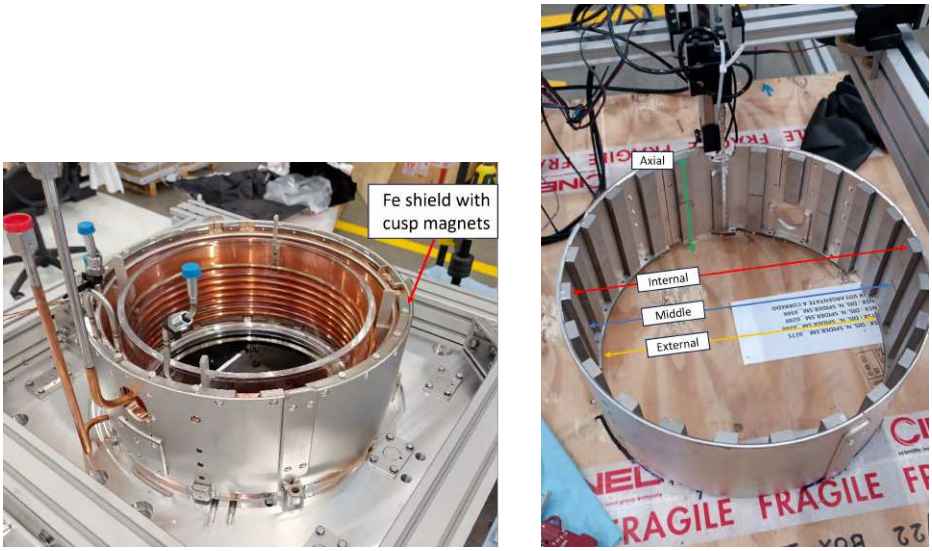

(a) (b)

Figure 4.2: (a) Minion driver connected to the plasma box, where the coil, cooling ducts, and the Fe shield to which the cuspidal magnets are attached can be distinguished; (b) the experimental setup for bench measurement of the driver's magnetic field is detailed, including the experimentally measured field profiles, which are then compared with the simulation profiles.

corresponding to the innermost region facing the plasma box. Additionally, the radial profile in front of a magnet pair and at 2 cm away from the magnets was measured to gain an understanding of the actual magnetic field value inside the driver. In Figure 4.3, the obtained profiles are presented.

From the comparisons of the profiles, we observe that the simulation fairly accurately reflects the experimentally derived profile. The discrepancies between the two trends are to be considered as a result of the measurement under non-ideal magnetic field conditions. Specifically, the measurements were conducted on a bench after assembling the iron shield, which was not perfectly calibrated as it was not constrained to the supporting structure. The gaussmeter probe itself was manually operated, therefore, there might be a measurement error in terms of alignment with the magnets and the orientation of the probe itself.

Figure 4.4 shows the simulation of the magnetic field produced by this configuration and the respective field lines. As we can see, the field thus generated forms a circular crown around the walls of the driver, where the field effect helps reduce the diffusion of charged particles to the wall, thereby confining the plasma inside.

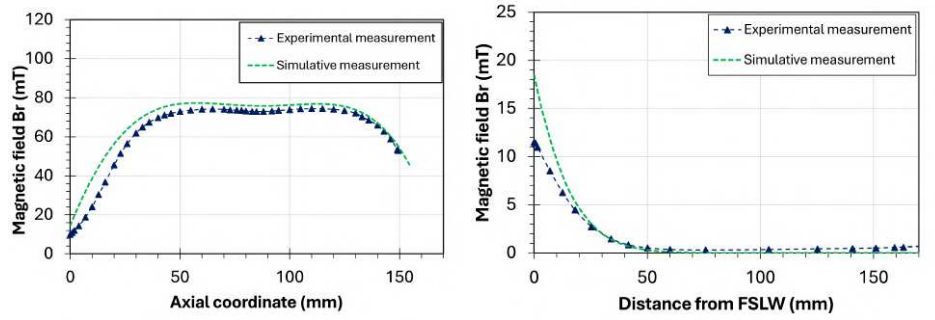

(a) (b)

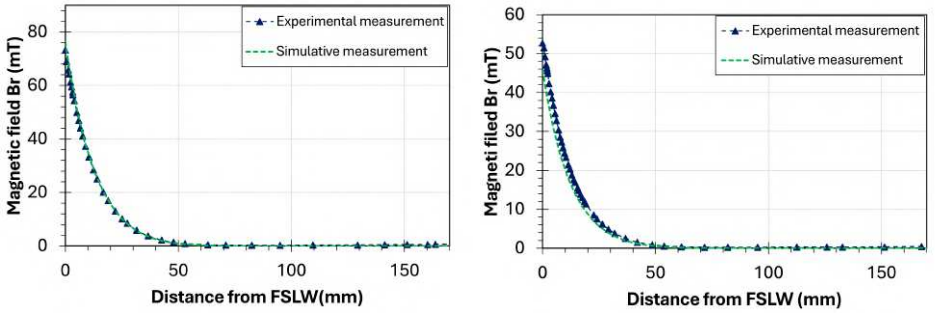

(c) (d)

Figure 4.3: Comparisons between the magnetic field profiles of the shield with 24 cuspidal magnets, measured experimentally, and derived from the simulation: (a) axial profile, (b) external radial profile, (c) middle radial profile, (d) internal radial profile.

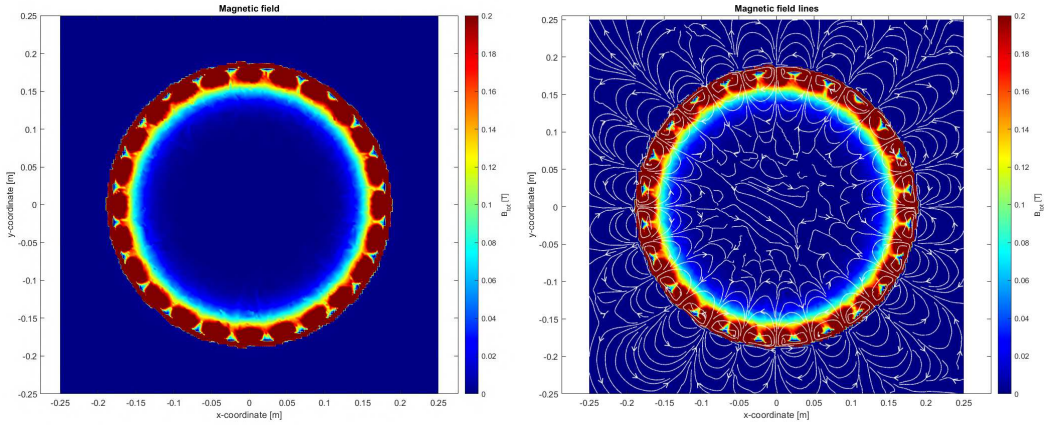

(a) (b)

Figure 4.4: Magnetic field produced by the 24 cuspidal magnets (a) with and (b) without field lines.

4.1.2 12 cuspidal magnets

Now let's consider the magnetic configuration with 12 cuspidal magnets positioned around the driver. The magnets are the same as those used and described previously in the configuration with 24 magnets. Once again, to validate the simulation, the magnetic

field profiles measured on the bench with the same experimental setup seen before were compared with the profiles derived from the simulation. The collected data is presented in Figure 4.5.

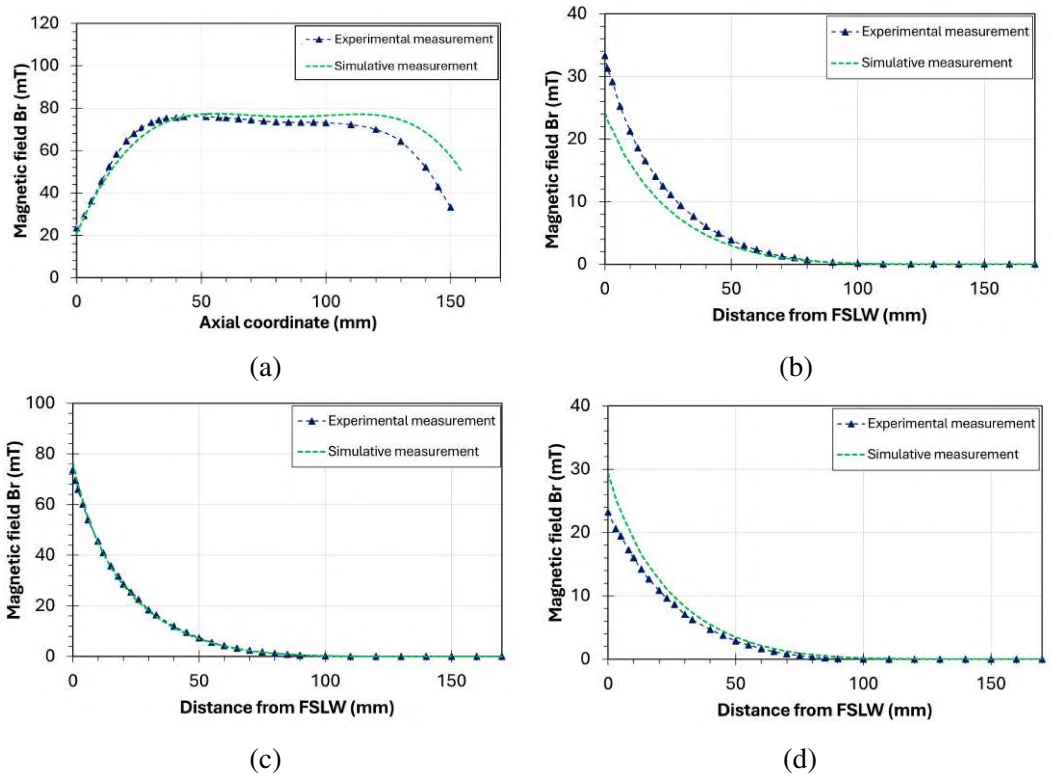

Figure 4.5: Comparisons between the magnetic field profiles of the shield with 12 cuspidal magnets, measured experimentally, and derived from the simulation: (a) axial profile, (b) external radial profile, (c) middle radial profile, (d) internal radial profile.

Comparing the experimentally measured magnetic field profiles with the profiles derived from the simulation, we observe that the trends are maintained with a certain margin of error. As previously mentioned, the discrepancy with what is obtained in the simulation is attributed to the manual mode in which the experimental measurements were collected on the test bench. In Figure 4.6, the magnetic field map derived from the simulation with the respective field lines is then presented.

From the magnetic field map, we can see that the field penetration profile with the 12 magnets configuration is more significant compared to that obtained with the 24 magnets configuration. In Figure 4.7, these two models are compared in detail.

This aspect becomes crucial and relevant in plasma creation. The configuration with 12 magnets positively allows for a significant increase in magnetic confinement, as the region where the effect of the field becomes less relevant shifts to a smaller circular section inside the driver. Theoretically, this configuration would allow for a higher plasma density and reduced losses to the walls of the Faraday shield. However,

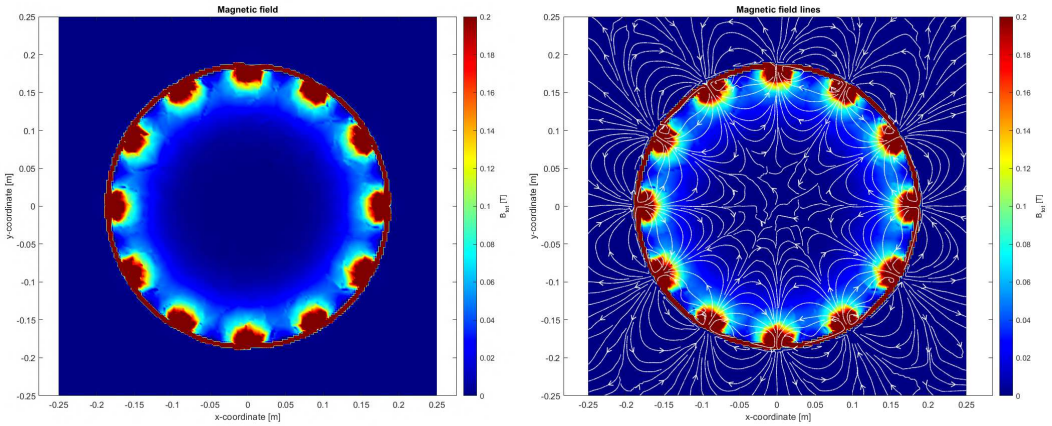

(a) (b)

Figure 4.6: Magnetic field produced by the 12 cuspidal magnets (a) with and (b) without field lines.

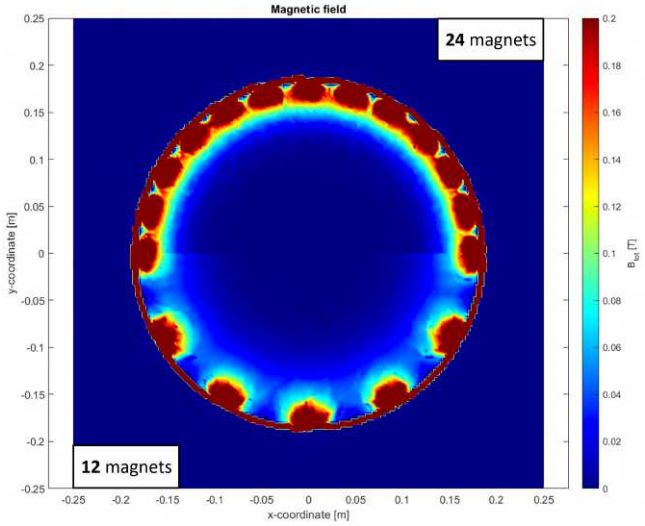

Figure 4.7: Comparison between the thickness of magnetic field penetration inside the driver with the configurations of 24 and 12 cuspidal magnets.

experimentally it has been found that such intense magnetic confinement requires a large RF power for plasma ignition and a much higher chamber pressure compared to the conventional $0.3-0.4$ Pa. Specifically, it has been observed that the power required for ignition and sustaining the plasma, with the configuration with 12 magnets, must be $P_{RF} > 55$ kW, and the necessary chamber pressure must be $p_{source} > 1$ Pa. At lower powers, only a poorly ionized, high-density plasma is obtained.

4.2 Comparison between visible cameras and simulations

Starting from the magnetic models of the driver developed with *Ansys Maxwell* and validated by comparison with experimental measurements taken with the gaussmeter a qualitative comparison between simulations and images from the visible is made. For this purpose, the model of the filter field was added to the *Ansys* simulations.

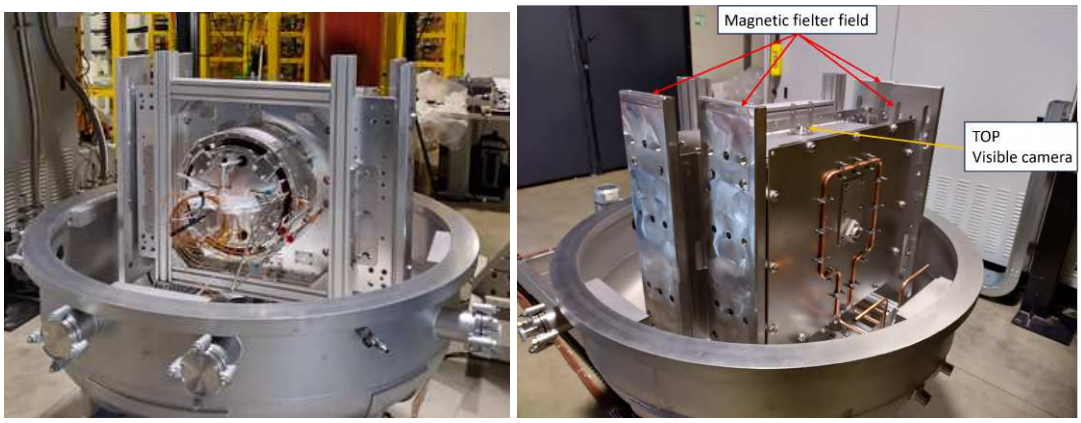

(a) (b)

Figure 4.8: Experimental setup of the MINION source: (a) rear view of the source; (b) frontal view of the source highlighting the filter field and the visible camera positioned on top of the plasma box.

In these series of analyses, the effect of the magnetic field generated by the magnets on the bottom of the driver will be neglected, as the generated effect becomes entirely negligible upon the driver's exit towards the expansion chamber. As reported in the general description of the MINION experiment in the previous chapter, during this first experimental campaign, the filter field was implemented using permanent magnet bars placed at the sides of the plasma box. An image of this implementation is shown in Figure 4.8. Below are analyzed the main magnetic configurations studied experimentally by comparing the images collected from visible cameras with magnetic simulations derived from *Ansys* models.

4.2.1 24 cuspidal magnets with filter field

The first configuration analyzed is the one implementing a setup with 24 cusp magnets around the driver, and the filter field implemented close to the expansion chamber. Charged particles subject to the magnetic filter field due to Lorentz force move through space along the field lines. Photons emitted by such particles and collected by cameras

will therefore exhibit a higher luminous intensity along paths that follow the direction of the magnetic field.

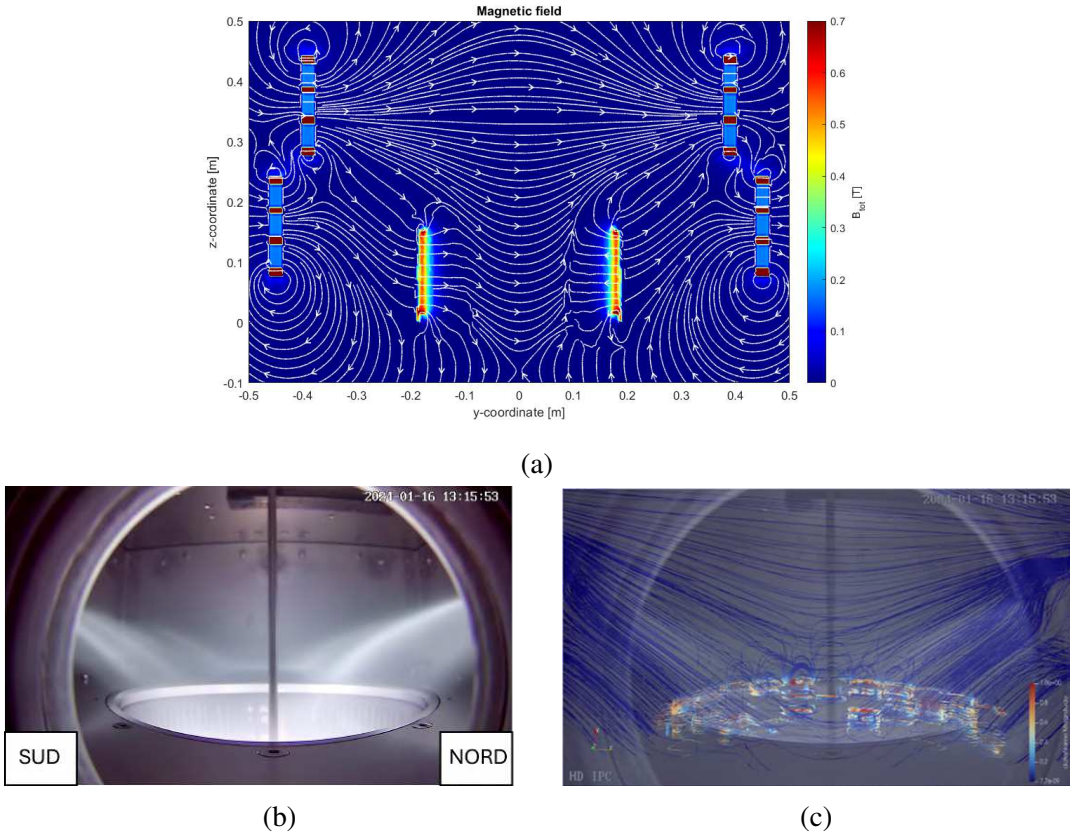

(a)

(b) (c)

Figure 4.9: (a) Simulation of the field lines in a 2D view of the cross-section in the y-z plane of the driver and the filter field with 24 cuspidal magnets; (b) image of the top camera obtained with a power of 30 kW at a pressure of 0.3 Pa; (c) field lines in a 3D view overlaid on the camera figure.

Figure 4.9 shows the simulation and comparison for the configuration with 24 cuspidal magnets. From the magnetic analyses conducted, consistent with what was observed by the visible camera, we see how the field lines produced by the filter magnets enter the driver at a certain angle. The charged particles and the photons emitted by them during state transitions follow the field lines generated by the filter magnets. The charged particles produced in the driver are thus assisted in moving towards the expansion chamber, allowing the electron temperature near the walls of the driver and the plasma box to be lowered. In detail, the luminous beam observed throught the chambers corresponds to the area of high-temperature charged particles. We see, in fact, how it is concentrated inside the driver, while in the expansion chamber the luminous intensity decreases due to the lowering of electronic temperature caused by the action of the filter field.

4.2.2 12 cuspidal magnets with filter field

Regarding the configuration with the 12 cuspidal magnets, the analysis conducted previously has demonstrated that the effect of the magnetic field produced by the cusps affects a larger area of the driver.

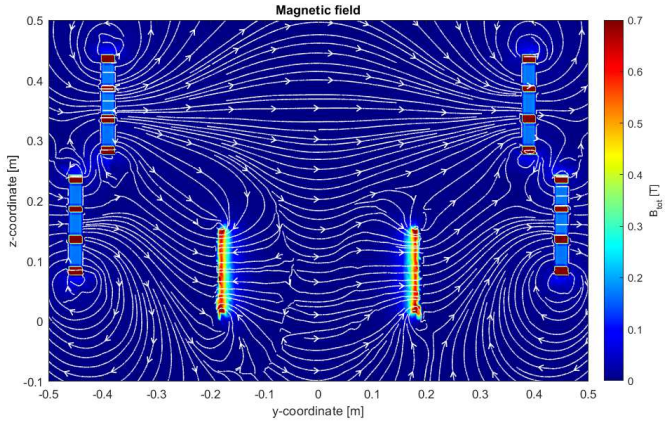

(a)

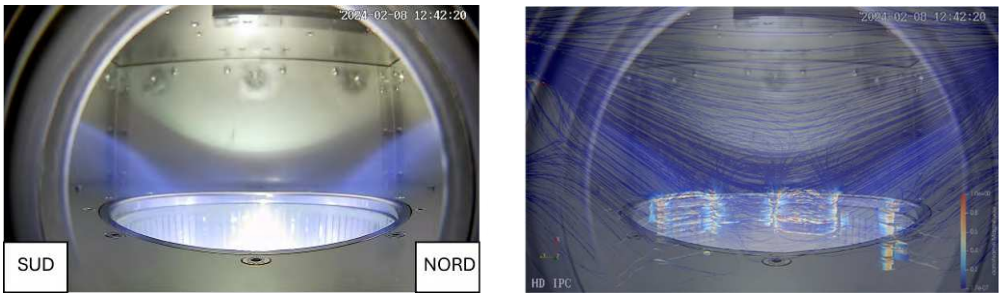

(b) (c)

Figure 4.10: (a) Simulation of the field lines in a 2D view of the cross-section in the y-z plane of the driver and the filter field with 12 cuspidal magnets; (b) image of the top camera obtained with a power of 40 kW at a pressure of 0.6 Pa; (c) field lines in a 3D view overlaid on the camera figure.

The magnetic field effect is to reduce plasma diffusivity and consequently its conductivity, allowing for magnetic confinement of the fluid within a more restricted region inside the driver. However, with this configuration, it was found experimentally that the effect of the field produced by the 12 cuspidal magnets combined with the field produced by the filter magnets was too high to allow for ignition and sustainment of plasma at low pressures or low powers. Considering a pressure of 0.6 Pa at a power of 40 kW, conditions under which dense plasma was produced with other configurations, with this configuration, at most, poorly ionized plasma at very low density was achieved. Figure 4.10 shows the results obtained through visible cameras and magnetic field line analysis.

In order to reduce the excessively high magnetic field and to achieve a dense plasma

at not excessively high powers, an attempt was made to remove the pair of magnet packs from region close to the driver.

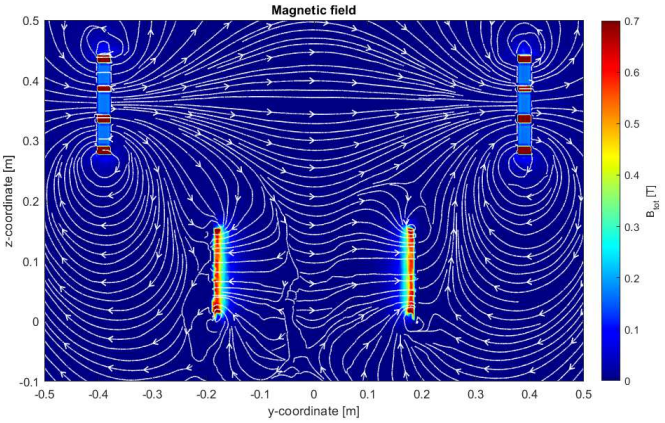

(a)

(b)

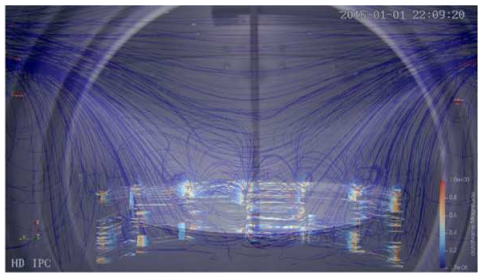

(c)

Figure 4.11: (a) Simulation of the field lines in a 2D view of the cross-section in the y-z plane of the driver and the filter field with 12 cuspidal magnets and without the filter field close to the driver; (b) image of the top camera obtained with a power of 55 kW at a pressure of 1.5 Pa; (c) field lines in a 3D view overlaid on the camera figure.

The effect of removing this pair of magnetic packs is, on one hand, to definitely reduce the field inside the driver, however, on the other hand, it increases the angle at which the field lines enter the driver, effectively unbalancing the filter field. The result obtained, as shown in Figure 4.11, was still achieving a denser plasma but necessitated further increasing the source pressure, brought to approximately 1.5 Pa, and increasing the power to 55 kW.

4.2.3 Without cuspidal magnets and with Fe shield

The last configuration for which it's possible to make a qualitative comparison of the field lines with the images collected by the visible cameras is the configuration where the cuspidal magnets were removed, and the iron shield around the driver was retained. This configuration aims to leverage the benefits induced by the use of the ferromagnetic shield while eliminating the confinement effects of the cuspidal magnets.

In Figure 4.12, the comparison between the field lines derived from the Ansys model and the images collected by the camera is shown.

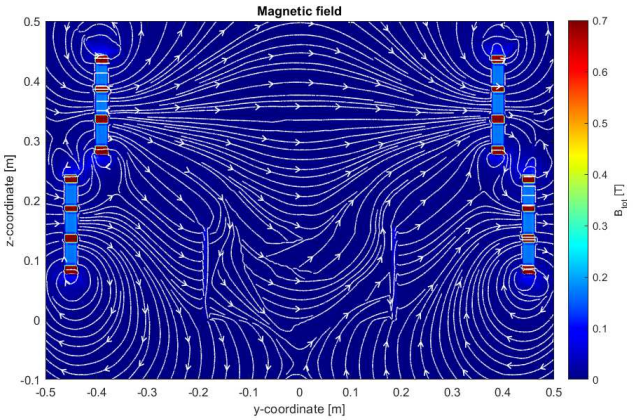

(a)

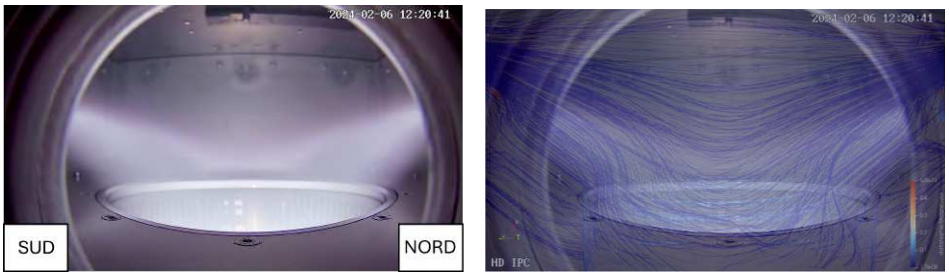

(b) (c)

Figure 4.12: (a) Simulation of the field lines in a 2D view of the cross-section in the y-z plane of the driver and the filter field without cuspidal magnet and only with the Fe shield; (b) image of the top camera obtained with a power of 60 kW at a pressure of 0.3 Pa; (c) field lines in a 3D view overlaid on the camera figure.

Unlike the other configurations, we observe that the field lines enter the driver without the hindrance of the field produced by the cuspidal magnets, allowing for easier extraction of the plasma towards the expansion chamber.

4.3 Configuration comparison

In this section, the main results obtained from comparisons with the different magnetic configurations tested during the experimental phase are summarized. The configuration with 12 magnets is disregarded from the comparison since the previous analysis has shown how excessive confinement is not applicable to the generation of low-pressure plasma, such as the parameters indicative of ITER. Instead, the configuration without both the cuspidal magnets and the ferromagnetic shield is considered. This configuration is similar to the one originally used on SPIDER and was tested during

the activity. However, no images were collected from the cameras in the visible spectrum. Figure 4.13 schematically summarizes the effects of the filter field on the source.

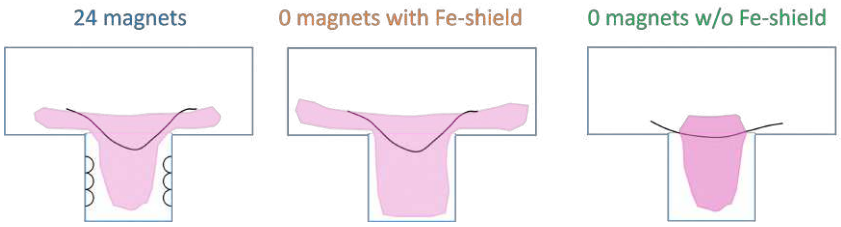

Figure 4.13: Schematic comparison of the effects of the filter field on the main configurations studied

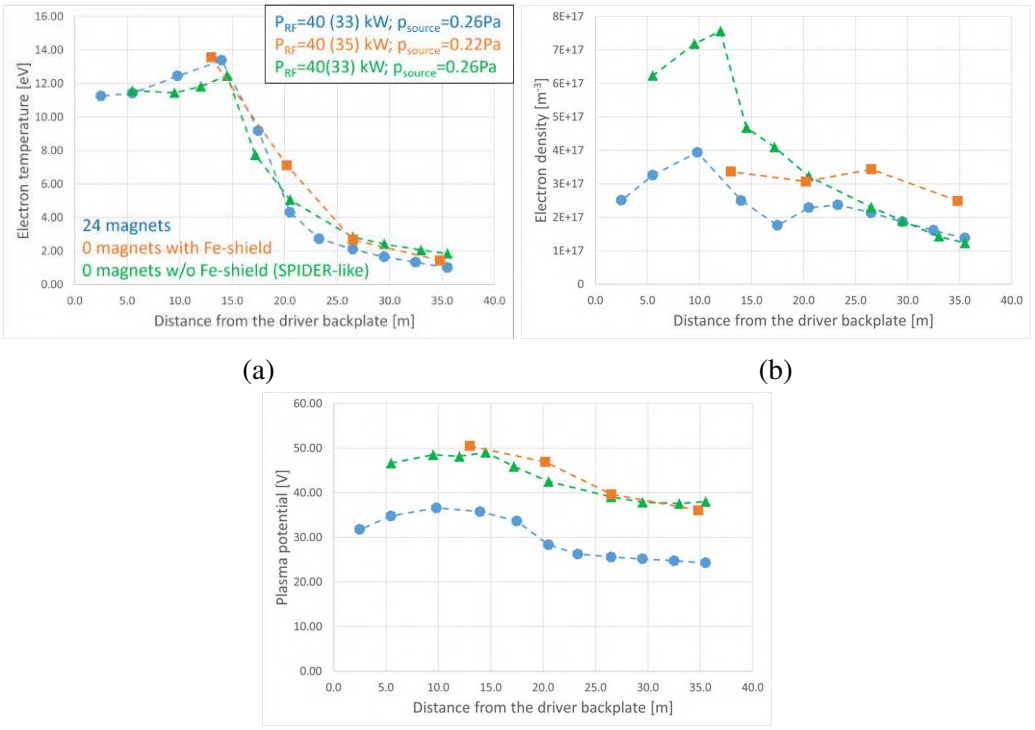

Figure 4.14: Comparison of axial profiles of (a) electron temperature, (b) electron density, (c) plasma voltage measured through the mobile Langmuir probe for the three magnetic configurations.

In summary, we obtain that: with 24 (and 12) cuspidal magnets, we have strong confinement inside the driver and highly concentrated field lines wrapped around the driver. Without cuspidal magnets but with the iron shield, we obtain more open field lines compared to the configuration with cuspidal magnets and a smoother flow towards the expansion chamber. Without cuspidal magnets and without iron, we obtain even more open field lines, but they tend to confine the plasma within the driver.

In Figure 4.14, measurements axial profile of electron temperature, electron density, and plasma voltage obtained through the mobile Langmuir probe are reported.

In detail, we observe the effect of the filter field on the different configurations. For all three configurations, the electron temperature at the exit of the driver, approximately 14 cm from the driver backplate, drops due to the filter field effect. Regarding the electron density in the configuration similar to that of SPIDER, it also drops at the exit of the driver. This indicates that the filter field tends to confine the plasma inside the driver. In the other two configurations, however, we see that the density at the exit of the driver remains high towards the plasma grid due to the filtering field effect that tends to help the plasma exit the driver. Among all, the configuration without cuspidal magnets but with the electromagnetic shield is the one that allows for the highest density at the plasma grid, thus appearing to be the most promising for future analyses in SPIDER and MINION. However, this aspect must be studied more thoroughly as it is a three-dimensional problem, and during this initial phase of experimentation, the diagnostics used have only provided 1D results. In the future, specialized diagnostics are expected to be available to sample the 3D space. The beneficial effect of the cuspidal magnets is observed in the plasma potential, where this configuration allows for a lower value. The lower plasma potential is related to reduced losses at the faraday shield surface in the driver region, due to the presence of cusp magnets.

Chapter 5

Modeling of inductive coupling in the RF driver of MINION

This chapter is dedicated to the study of inductive coupling. To this end, various tools are used, including data obtained from experimental measurements, magnetic models, and diagnostic results. Particular attention is paid to finite element method simulations performed using the FEMM software. In this regard, the first part of the chapter provides a brief introduction to FEMM. Subsequently, the measurements taken during the vacuum tests are reported and compared with the results obtained from the simulations. The focus then shifts to plasma modeling. It is well known that, when the transverse filter field is applied to limit the diffusion of hot electron towards the extraction region of the ion source, the driver region is affected as well, and the plasma distribution strongly departs from the cylindrical symmetry. For this reason, we focused the benchmark on the axissymmetric cases with no filter field applied. Experimental data obtained will be presented, and the main phenomena underlying the simulations will be discussed. Special attention will be given to studying the sensitivity of the implemented model.

5.1 Finite-Element-Method-Magnetics (FEMM) code

FEMM is a suite of programs used for solving frequency electromagnetic problems in two-dimensional planar and axisymmetric domains. Presently, the suite handles a range of problems including linear and nonlinear magnetostatic issues, linear and nonlinear time harmonic magnetic problems, linear electrostatic concerns, and steady-state heat flow problems.

For simple magnetostatic problems the field intensity H and the flux density B are given by:

$$\nabla \times H = J \tag{5.1}$$

$$\nabla \cdot B = 0 \tag{5.2}$$

For each material, the relationship between B and H is:

$$B = \mu H \tag{5.3}$$

where μ is the permeability of the material. FEMM solves the field using the magnetic vector potential approach by solving the Equation 5.1 and the Equation 5.3. Flux density is written in terms of the vector potential A as:

$$B = \nabla \times A \tag{5.4}$$

The definition of B now satisfied the Equation 5.2. So, the Equation 5.1 can be written as:

$$\nabla \times \left(\frac{1}{\mu(B)} \nabla \times A \right) = J \tag{5.5}$$

When the magnetic field is time varying, eddy current can be induced in materials with a non-zero conductivity. Denoting the electric field intensity as E and the current density as J the relationship can be written as:

$$J = \sigma E \tag{5.6}$$

where σ corresponds to the conductivity of the material. The induced field than obeys:

$$\nabla \times E = -\frac{\partial B}{\partial t} \tag{5.7}$$

Substituting the vector potential form of B, we can say that:

$$\nabla \times E = -\nabla \times \dot{A} \tag{5.8}$$

Substituting into Equation 5.5 we obtain the partial differential equation:

$$\nabla \times \left(\frac{1}{\mu(B)} \nabla \times A \right) = -\sigma \dot{A} + J_{scr} - \sigma \nabla V \tag{5.9}$$

where J_{scr} represents the applied currents sources and the term ∇V is an addition voltage gradient over the conducting body.

For the problems where field is oscillating at one fixed frequency, e.g. simulating

the source where the frequency is 1 MHz, FEMM implement the *phasor transformation* algorithm to solve the amplitude and the phase of A. Using this approach, the equation Equation 5.9 became:

$$\nabla \times \left(\frac{1}{\mu_{eff}(B)} \nabla \times a \right) = -j\omega\sigma a + \hat{J}_{scr} - \sigma \nabla V \tag{5.10}$$

where $\hat{J}_{scr}$ represent the phasor transform of the applied current source and μ_{eff} is the effective permeability selected to give the correct amplitude of the fundamental component of the waveform under sinusoidal excitation.

The macroscopic properties of the system are calculated in a discretized domain called *mesh*. The bidimensional problem is divided into a large number of regions of simple geometry (FEMM specifically uses triangular elements). In each element, the solution is approximated using linear interpolation of the values of potential at the three vertices of the triangle. Within each element, different properties can be defined in terms of electric conductivity and magentic permeability.

The model developed and used in this thesis is an axial symmetric simulation of the plasma source and driver used in MINION. In the axial symmetric model, the magnetic filter field induced by the magnets located outside the plasma box, is not included, and neither are the cusp magnets around the driver and the perm magnets in the driver back plate. These three fields are indeed not spatially axially symmetric, thus not reproducible correctly by the model. However, the effect of the magnetic field generated by the magnets can be considered in the calculation: being static contributions to the magnetic field, they do not influence the time-varying solution of the induced currents. However, when the plasma is ignited and becomes itself a conductor, the static magnetic field such as the one produced by permanent magnets influences the electric conductivity of the plasma. This effect must be taken into account in the induction model. The plasma conductivity model will be described in details in subsection 5.3.1. Regarding the effects induced by this field, a sensitivity study will be conducted in order to properly weigh the effects of this non-axially symmetric field.

A second interesting aspect in the implementation of the model concerns the modeling of the Faraday shield. As described earlier, it represents the surface directly facing the plasma and is formed by a copper cylinder internally lined and coated with molybdenum. The walls of the cylinder are machined with z-shaped slits oriented along the axis of the cylinder. that cannot be represented in an axially symmetric model. To realistically model the Faraday shield, 3-D simulation models used for the study of much more complex plasma sources were used. From the analysis of these models, a good approximation for the Faraday shield geometry is obtained by consid-

ering a fictitious material with a conductivity slightly higher than that of copper, equal to $\sigma_c = 58$ MS/m, identical to $\sigma_{FS} = 60$ MS/m.

The the creation of geometry and mesh and the execution of the simulation with FEMM are performed using a Python script. An image of the simulation model is shown in Figure 5.1.

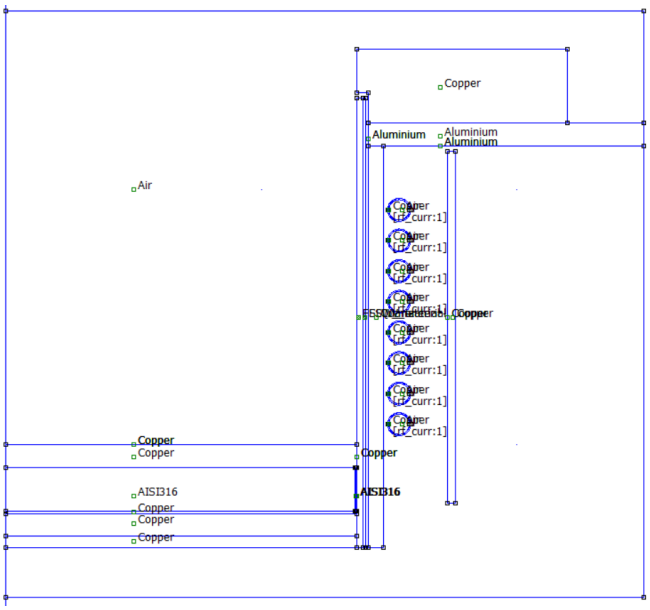

Figure 5.1: FEMM model implemented. The left axis corresponds to the driver axis. Therefore, the layers of the driver back plate and side walls, the coil, and the electromagnetic shield (EMS) on the right are highlighted. In this image, air is present inside the driver.

5.2 RF induction fields without plasma

In this section, the data collected during the low-voltage tests conducted during the commissioning phase of MINION are analyzed and compared with the results of the FEMM simulation in order with the aim of validating the code.

The voltage tests were conducted in air with the vessel open up to powers of 300 W. These tests were essential in characterizing the circuit to establish the overall load of the source in order to adjust the matching network to match the load with the oscillator. As explained in subsection 3.3.3, the oscillator exhibits maximum efficiency when connected to a predominantly resistive load of $50\,\Omega$. Therefore, it is necessary to know the load of the source in order to properly tune the capacitors of the matching network. The low-voltage open-circuit tests primarily serve this purpose. A preliminary measurement of the circuit characteristics of the system had been conducted using an impedance meter, obtaining the aforementioned data of resistance equal to $R = 720$

mΩ and inductance of $L = 8.8$ mH at a frequency of $f = 1$ Mhz. However, it is desired to derive the same parameters a significant power is delivered to the system; therefore, dedicated tests were performed as discussed in the following subsection 5.2.1. The results were the benchmark for the FEMM model, as described in subsection 5.2.2.

5.2.1 Measurement of the output power

To obtain the voltage and current measurements delivered from the RF oscillator to the load, the system shown in Figure 5.2 was used.

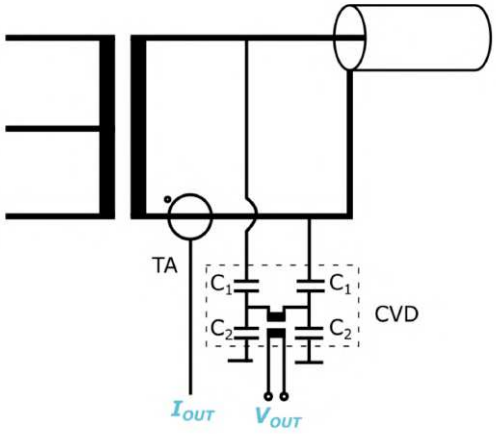

Figure 5.2: Measurement system used for voltage and current measurements on MINION: current transformer (TA) for current measurement and capacitive voltage divider (CVD) for voltage measurement. The two thicker rectangular elements represent the inductive coupling between the RF coil on the right and the metal structures and plasma on the left.

It consists of a capacitive voltage divider (CVD) used for voltage measurements and a current transformer (TA) for current measurement. The CVD and TA were placed downstream of the matching network. Specifically for current measurement, various independent devices were used: two Stangenes current transformers with ratings of 220 A_{RMS} and 60 A_{RMS} respectively, and a Tektronix TCP 303 current probe. The active output power P was measured using the volt-ampere method, integrating the instantaneous values of voltage, $v_M(t)$ and current, $i_M(t)$:

$$P = \frac{1}{t_2 - t_1} \int_{t_1}^{t_2} v_M(t) \cdot i_M(t) dt \tag{5.11}$$

During the low-voltage tests, the values of active power, current on the coil, and voltage at the high-voltage side of the coil were experimentally obtained.

As for the measurements of circuit parameters at high power operation with the plasma, a second independent measurement instrument, the dual directional coupler (DDC), was added to the CVD. This instrument is a four-port meter capable of measuring the forward and reverse voltages in the load and allows for evaluation of the forward and reflected power. Unfortunately, during the high-voltage tests, the measurement of the current on the coil was not collected.

5.2.2 Data collected and FEMM simulation

Let's begin now the analysis of the low-voltage tests conducted on MINION in vacuum. Table 5.1 lists the main data collected during the tests, specifically the obtained active power, the currents measured by the three current probes, and the voltage obtained from the CVD at the high voltage coil feedthrough.

P (W)	$\mathbf{I}_{Tek}$ **($\mathbf{A}_{RMS}$)**	$\mathbf{I}_{Stan220}$ **($\mathbf{A}_{RMS}$)**	$\mathbf{I}_{Stan60}$ **($\mathbf{A}_{RMS}$)**	$\mathbf{V}_{m,CVD}$ **(mV)**	$\mathbf{V}_{p,CVD}$ **(kV)**
40	7.85	9.82	7.53	26	0.64
83	11.45	14.3	11	37.7	0.92
124	13.93	17.4	13.37	45.8	1.12
165	16.05	20.04	15.38	52.4	1.29
206	17.8	22.23	17.06	58	1.42

Table 5.1: Active power, current measured by the three probes, and voltage measured by the CVD during low voltage tests at $f = 1$ MHz.

Regarding the current measurements, we see that the three probes have obtained slightly different results. Specifically, the Tektronix and Stangenes 60 probes collected comparable data, whereas the Stangenes 220 current probe collected values larger than the others. These discrepancies can be attributed to the non-ideal operation of the probes and the tolerances imposed by the instruments themselves in signal measurement. As for voltage measurement, the average voltage $V_{m,CVD}$ is obtained directly from the CVD, while the peak voltage $V_{p,CVD}$ can be derived by considering the voltage damping factor induced by the instrument, provided by the instrument itself as $k = -87.8$ dB.

To accurately estimate the circuit load, the measurements available were analyzed to retrieve resistance and inductance by comparing the measured active power and impedance with the calculated ones. By making this comparison using the three current measurements and minimizing the error between the powers and the total impedance of the circuit, the Tektronix probe yielded optimal results. The circuit parameters obtained from the measurements are $R = 0.657\,\Omega$ and $L = 9.08$ μH. As we can see,

the total impedance of the circuit is predominantly inductive. The resistive component contributes minimally compared to the total load.

Starting from the geometric dimensions of the source and the materials used in its construction, the FEMM model of the driver was then implemented. To fairly compare the FEMM model with the measurements, it was interrogated using the same RMS current measured by the Tektronix current probe. Table 5.2 reports the power and voltage parameters of the circuit obtained.

P (W)	**I (A_{RMS})**	**V_p (kV)**
39.09	7.85	0.526
83.27	11.45	0.768
123.14	13.93	0.934
163.5	16.05	1.076
201	17.8	1.194

Table 5.2: Active power, coil current and voltage at $f = 1$ MHz estimated by the FEMM simulation.

From the model, we obtain the following circuit parameters of resistance $R = 0.634\,\Omega$ and inductance $L = 7.55\ \mu$H. Table 5.3 summarizes the collected circuit parameters. While in the graphs of Figure 5.3, the comparisons between the experimentally measured data and those obtained from the FEMM model are presented.

Experimental data		**FEMM data**	
R (Ω)	**L (μH)**	**R (Ω)**	**L (μH)**
0.657	9.08	0.634	7.55

Table 5.3: Circuit parameters experimentally measured during low voltage tests and parameters estimated by the FEMM model.

From the comparison of the collected data, we can see that regarding the circuit resistance, the FEMM model estimates about 4% less resistance, while the error increases to about 18% for the inductance. These values are entirely reasonable considering the non-idealities of the real system compared to the simulated one. In terms of resistance, the error between the model estimation and the measurement is negligible whereas for the inductance, the discrepancy may depend on non-idealities of the model. The coil is represented as an ideal solenoid without simulating the connection part between the actual coil around the driver and the feedthrough vacuum and the connection point of the measurement system. For instance, we can discuss the influence of one part of the RF conductors inside the vacuum vessel, i.e. the 0.08 m-long segment in which the two conductors run parallel one to the other. Considering the two

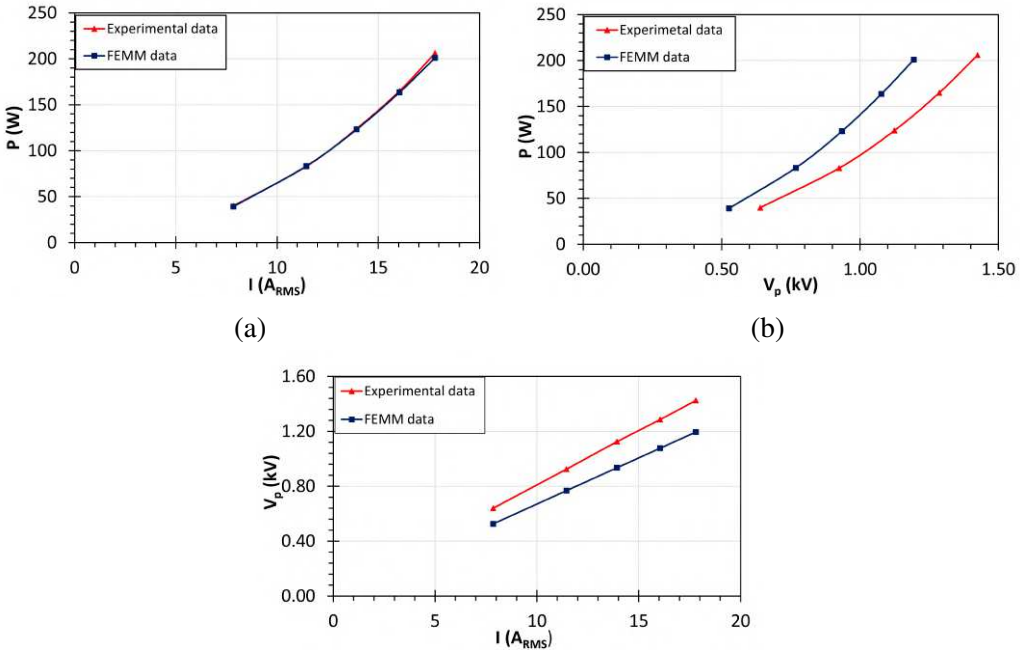

Figure 5.3: Comparison between experimentally derived measurements and data obtained from FEMM simulation: a) active power characteristic versus current on the coil, b) active power characteristic versus voltage at the high-voltage pass-through, c) comparison between voltage at the high-voltage pass-through and current on the coil.

parallel connections, one at high voltage and the other at low voltage, with a radius of $r = 0.005$ m, a distance of $d = 0.1$ m and a length of 0.8 m, it is possible to estimate the self-inductance coefficient of the two wires carrying current at high frequency as:

$$L_{ab} = \frac{\mu_0 l}{\pi} log\left(\frac{d}{2r} + \sqrt{\frac{d^2}{4r^2} - 1}\right) = 0.419\mu\text{H} \tag{5.12}$$

The total circuit inductance then becomes $L = 8.01$ μH. The additional difference between the circuit inductance and that estimated from the load can be attributed to other three-dimensional features not present in the simulation, such as the fact that the coil, when entering the driver, passes close to the ferromagnet, which alters its value by creating mutual couplings.

For all these reasons, mainly related to the non-ideal elements of the real circuit compared to the simulated model, it is possible to consider the geometric model of the driver sufficiently accurate and therefore proceed with the analysis of the system under operating conditions.

5.3 RF induction fields and power coupling with plasma

The main issues to address in order to correctly model the plasma on FEMM are the spatial distribution of the plasma parameters inside the driver, and the choice of the correct theoretical model needed to describe the electric conductivity of the plasma. its distribution in the driver. To describe the plasma as realistically as possible, it would be necessary either to perform a fully threedimensional experimental characterization of the plasma properties, or to perform a fully threedimensional plasma simulation, for instance by particle-in-cell or fluid models. Neither of these are available, and hypotheses have to be formulated to describe the radial shape of the plasma parameters. To simulate such distribution on the r,θ plane in FEMM, the approach chosen is to divide the interior of the driver into a grid consisting of 40 elements radially and 45 elements axially, and then define a different conductivity material for each element. Although this approximation is not extremely precise, it allows for a good distribution of plasma into the domain.

The problem now lies in how to calculate the conductivity of these elements and specifically which profile to use radially and axially. The only available measurements to base on are the axial profile measurements obtained through the mobile Langmuir probe, which define the axial profile of electron density n_e and electron temperature T_e. These axial profiles have been measured under operating conditions at 40 kW with a particular configuration without the filter field and without the ferromagnetic shield (and cusp magnets). Magnets positioned at the bottom of the driver were still present. Regarding radial profiles, in the absence of measurements, used approximations that will then be analyzed in detail. In Figure 5.4, the axial profiles of density and temperature measured by the Langmuir probe are shown.

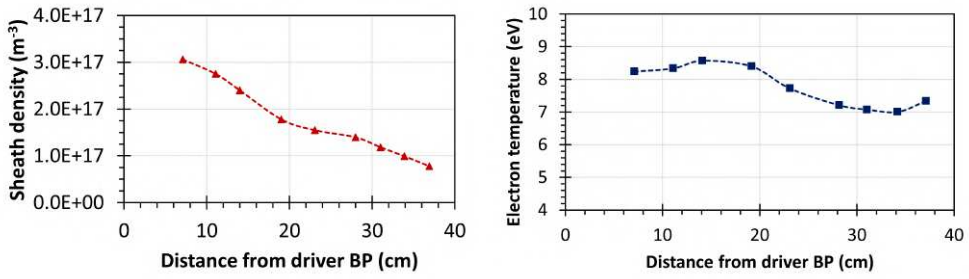

(a) (b)

Figure 5.4: Axial profiles obtained from the mobile Langmuir probe at power of 40 kW: (a) electron density, (b) electron temperature.

5.3.1 Plasma conductivity

Considering an inductive plasma source within a cylindrical geometry, the conductivity of the plasma can be defined as:

$$\sigma = \mu n_e = \frac{e^2 n_e}{m_e \nu_{eff}} \tag{5.13}$$

where $\nu_{eff} = \nu_{e,n} + \nu_{e,c} + \nu_{stoc}$ is the collision frequency and is defined as the sum of effects of the electron-neutral collisions $\nu_{e,n}$, Coulombic collisions $\nu_{e,c}$ and stochastic collisions ν_{stoc}. The contribution of stochastic effects is expected to be smaller than of to that of Coulomb collisions and it will not be considered in this treatment. As for the Coulomb collision frequency, it is mainly determined by the collisions between electrons and neutrals, electrons and ions, and electron-electron collisions.

As for the electron-neutral collision frequency, it can be measured starting from the gas density, obtainable from the source pressure and from the values of the momentum transfer cross-section Q_m derived from the literature. Specifically, the derived gas density is equal to:

$$n_{fill} = \frac{p_{source}}{k_B T} \tag{5.14}$$

where n_{fill} corresponds to the fill density of the source and n_{gas} can be approximated to about half of the fill density. As for the momentum transfer cross-section, the one obtained from the Ramanan and Freeman models for the hydrogen molecule is considered. The characteristic curve is shown in the Figure 5.5.

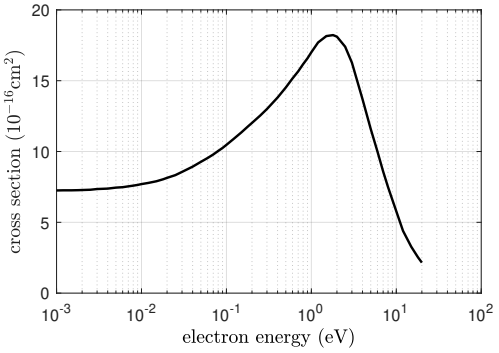

Figure 5.5: Momentum transfer cross section for molecular hydrogen. The values derived from mobility measurement by Ramanan and Freeman [48], [49].

As regard the electron-neutral collision can be said that:

$$\nu_{e,n} = n_{H2} \cdot \angle \sigma_{m,H2} v_e \rangle + n_H \cdot \langle \sigma_{m,H} v_e \rangle \tag{5.15}$$

The brackets indicate averaging over the maxwellian distribution of the quantity

$\sigma_m v_e$. The averaged term, called rate coefficient, is multiplied by the density of the background neutrals n_{H2} and n_H. The latter quantities are difficult to estimate: the dissociation degree n_H/n_{H2} can be derived only from optical emission spectroscopy, and not directly; the density of molecules n_{H2} differs from the filling density due to the heating by the plasma and by the ionization itself, in addition to the dissociation, which all deplete the gas density within the plasma discharge. In the following we will consider only an effective density of molecules n_{gas}, nu_e, $n \approx n_{gas} \cdot \langle \sigma_m v_e \rangle$ We can expect a strong reduction, say by a factor fo two with respect to the filling condition. Futher considerations about this term can be found in section 5.4.2

From the interpolated cross-section values and the gas density, a collision frequency for electron-neutral particles in the order of $\nu_{en} \simeq 10^6$ s^{-1} is derived.

Regarding the collision frequency of electron-electron and electron-ion, concerning the momentum loss, they depend on the electron density n_e (and ions assumed to be equal to that of electrons $n_e \simeq n_i$) and the electronic temperature T_e. The electron-ion collision frequency can be calculated as:

$$\nu_{ei} = \frac{\sqrt{2}}{3\sqrt{\pi}} n_e \left(\frac{e^2}{4\pi\varepsilon_0} \right)^2 \frac{4\pi}{m_e^{\frac{1}{2}} T_e^{\frac{3}{2}}} log\Lambda_e \tag{5.16}$$

where Λ_e corresponds to the Coulomb logarithm defined as:

$$\Lambda_e = \sqrt{\frac{\varepsilon_0 T_e}{n_e e}} \frac{4\pi\varepsilon_0 m_e v_{th,e}^2}{e^2} \tag{5.17}$$

where $v_{th,e}$ is the thermal temperature given by:

$$v_{th,e} = \sqrt{\frac{8k_B T_e}{\pi m_e}} \tag{5.18}$$

The collision frequency of electron-electron can be approximated under quasi-neutrality conditions as:

$$\nu_{ee} \simeq \frac{1}{\sqrt{2}} \nu_{ei} \tag{5.19}$$

With the density and temperature values of our application, the two collision frequencies assume values on the order of $\nu_{ei}, \nu_{ee} \simeq 10^4 - 10^5$ s^{-1}.

By summing the frequencies of electron-neutral collisions, which remain constant throughout the domain, and the frequencies of electron-ion and electron-electron collisions, which vary depending on the values of electron density and temperature, the total frequency of collisions ν_{eff} used in Equation 5.13 to calculate the plasma conductivity map is obtained.

As said, we will model in axissymmetric approximation the inductive coupling, and for this reason we will use as a benchmark the results of MINION without filter field. Nevertheless, magnets are embedded in the backplate of the driver. Magnets have the role of reducing the plasma losses at that surface; however, their magnetic field strongly affects the transport of electrons in the plasma volume as well. As discussed in the following subsection 5.4.2, we will symmetrize the magnetic field on the r, z plane, to derive on the same plane the map of electron conductivity along the azimuthal direction θ : to that purpose, only the magnetic field components perpendicular on the r,z plane will be considered, to estimate the reduction of the mobility as:

$$\mu_{\perp} = \frac{\mu}{1 + \left(\omega_c / \nu_{eff}\right)^2} \tag{5.20}$$

where the term $\omega_c = qB/m$ is the electron cyclotron frequency.

When an electron undergoes a collision while gyrating around a line of force, it alters its direction, thereby causing its center of gyration to shift, on average, by a gyration radius. This process is random but can be quantified by considering the perpendicular diffusion as the only mechanism of mobility perpendicularily to the magnetic field lines.

5.4 Analysis of inductive coupling with plasma

In this section, the data collected during high-power steady-state tests with plasma and those produced by the FEMM simulation are reported and analyzed. Firstly, experimentally derived data are discussed to observe how circuit parameters change in the presence of plasma. Subsequently, the study of inductive coupling is proposed using the axisymmetric model of FEMM. A sensitivity analysis is conducted to verify the robustness of the model, focusing on the following aspects:

- role of the magnetic field;
- validity of the axissymmetric approximation;
- radial profile of plasma density;
- role of neutrals

5.4.1 Experimentally collected data

As previously reported in the data measurement methods, the voltage in these tests was obtained using a DDC as a second independent measurement system, parallel

to the CVD. Regarding the current, however, we do not have a measurement due to malfunctions in the measurement systems caused by high RF noise. Therefore, the only circuit data collected are the power and the voltage at the high-voltage passerby. Without the current measurement, there is an additional constraint on the estimation of circuit parameters. To mitigate this problem, it is reasonable to consider that the circuit inductance does not vary significantly during the plasma discharge, considering the shielding effect of the plasma to be negligible at not too high densities. Since inductance, as demonstrated in the low-voltage tests, is the main contribution to the system impedance, assuming the circuit inductance to remain constant, the only circuit term that changes becomes the resistance. We reasonably expect that the circuit resistance increases because, with the presence of plasma inside the driver. The plasma itself becomes a sort of resistive component. Taking these considerations into account, the power and the voltage measurements, and the estimated current are reported in Table 5.4.

$\mathbf{P}_{tot}$ (kW)	$\mathbf{P}_{d}$ (kW)	$\mathbf{V}_{p,CVD}$ (kV)	$\mathbf{V}_{p,DDC}$ (kV)	I ($\mathbf{A}_{RMS}$)
40	35	13.40	13.48	166.16
50	43	15.22	14.94	188.74
60	52	16.63	16.43	206.30

Table 5.4: Total and direct power measurements, voltage measured by the CVD and by the DDC at the high-voltage passerby, and estimation of the current on the coil.

We can see how the voltage values measured by the two instruments are almost identical. In the next analyses, we consider the measurements obtained with the DDC as reference measurements.

Considering, therefore, the inductance constant compared to that obtained during the low-voltage tests equal to $L = 9.08\ \mu$H, we obtain an estimate of the circuit resistance equal to $R \simeq 1.22\,\Omega$. This value is approximately doubled compared to that obtained without plasma.

5.4.2 FEMM simulation of plasma and sensitivity analysis

As previously mentioned, in order to simulate the plasma with the FEMM model, the interior of the driver was divided using a grid consisting of 40 elements radially and 45 elements axially, for which a different material was defined.

The main issue encountered during the simulation is the presence of the magnetic field produced by the magnets placed at the bottom of the driver. This magnetic field, indeed, is not axisymmetric. In order to interpret the spatial behavior of this field, a magnetic simulation was conducted using *Ansys Maxwell* software of the magnets on

the back plate (BP) of the driver, from which a spatial map of the field was obtained. Then is was used to correctly calculate the plasma conductivity. Figure 5.6 shows the Ansys model used for the modeling of the magnets placed in the back plate of the driver and the map of the rz components of the magnetic field seen on an $r-\theta$ plane taken at a distance of 10 cm from the driver back plate.

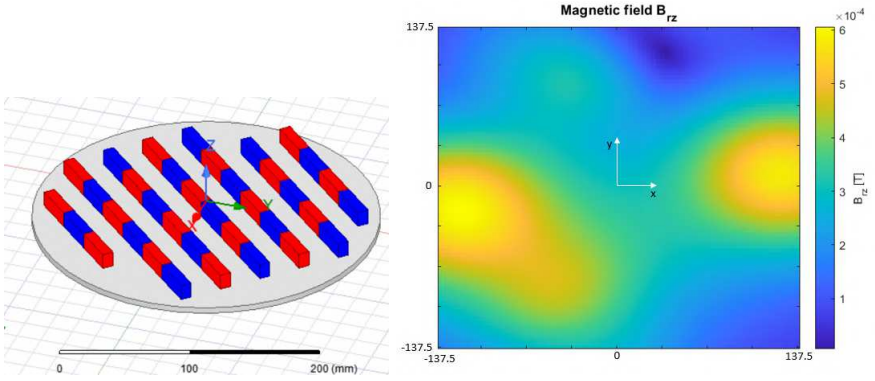

(a) (b)

Figure 5.6: (a) Ansys model used for simulating the magnetic field produced by the magnets of the BP driver; (b) component of the magnetic field B_{rz} produced by the magnets on the bottom of the driver seen on an $r-\theta$ plane placed at 10 cm from the BP.

Analyzing the spatial arrangement of the magnets and the subsequent map of the magnetic field, we can see that the positioning is not symmetric, and consequently, neither is the produced field. Therefore is it difficult to reproduce in in an axisymmetrical simulation. To overcome this issue, several sensitivity tests were conducted to better understand the effect of this field. The main parameters studied in the sensitivity analysis were: the intensity of the B_{rz} field and its variability depending on the chosen angle to extract the 2-D map, dependence on the shape of the radial density profile, dependence on the density of electrons and gas.

Dependence on the field intensity

First, in Figure 5.7, the trend of the estimated active power from the simulation is shown as the magnetic field varies, starting from a condition where there is no magnetic field present, up to a condition where we have the actual field. For this series of tests, the rz components of the magnetic field taken at a plane rotated at 45 degrees were considered and a radial profile of n_e proportional to a Bessel function of order zero was used.

As we can see from the trend represented in the graph, in conditions of work without a magnetic field, the simulated active power turns out to be an order of magnitude

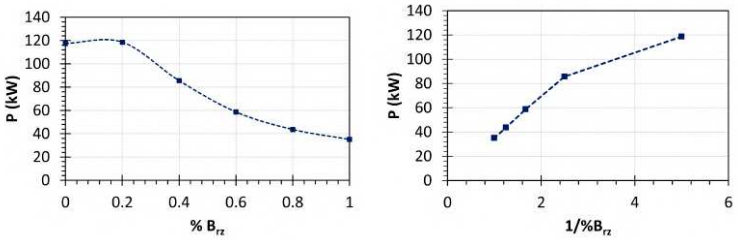

(a) (b)

Figure 5.7: Active power simulation as a function of the percentage of magnetic field B_{rz} produced by the magnets on the bottom of the driver. Plasma radially with a profile proportional to a first-order Bessel function and planar in $r-z$ at 45 degrees, (a) percentage of B, (b) ratio of percentage of B.

higher compared to that obtained considering the magnetic field in the BP. In Figure 5.8 and Figure 5.9, maps of the current density on the plasma and maps of the plasma conductivity are shown in two boundary conditions: without magnetic field from the magnets and with total field. In the graph of Figure 5.10, the normalized radial profile of the induced current in the plasma is instead reported, considering a line approximately 10 cm from the driver BP.

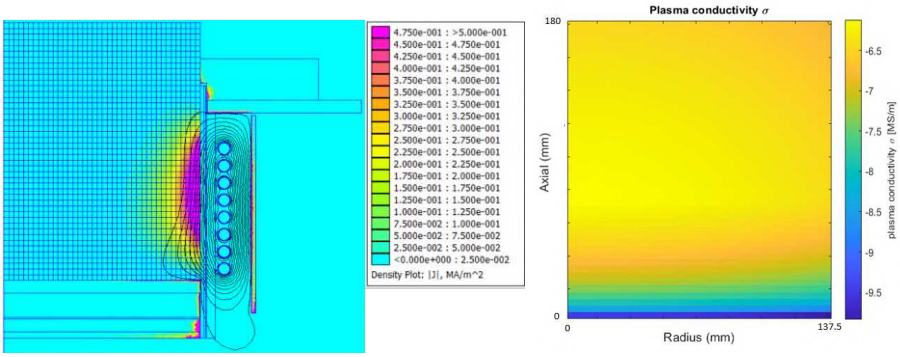

(a) (b)

Figure 5.8: Operating condition without magnetic field from the magnets on the bottom: (a) map of the current density on the plasma, (b) map of plasma conductivity.

As we can see, the magnetic field significantly limits the power coupled with the plasma and consequently the current density in it. However, this consideration does not take into account the fact that the magnets allow the plasma to be confined, reducing the loss area. This area is inversely proportional to the magnetic field at the wall, so eliminating the magnets it will increase. In detail, we can write the following relationships:

$$P = q_e n_s u_B A_{loss} \varepsilon_{ext} \tag{5.21}$$

where P represent the power absorbed by the plasma, u_B is the Bohm velocity, ε_{ext} is

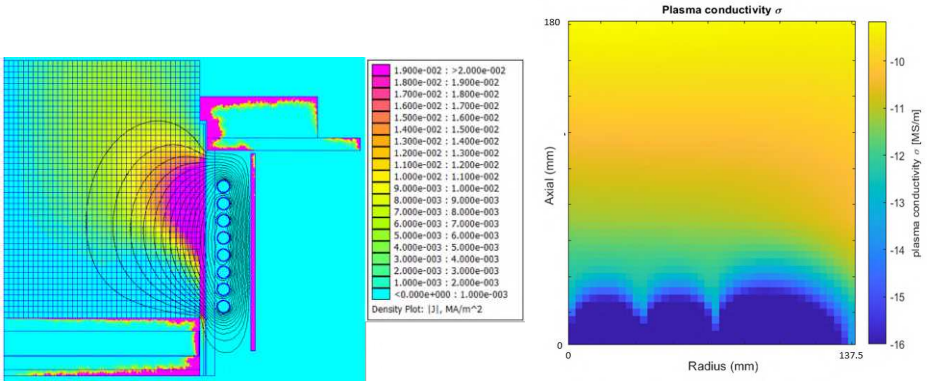

(a) (b)

Figure 5.9: Operating condition with magnetic field from the magnets on the bottom: (a) map of the current density on the plasma, (b) map of plasma conductivity.

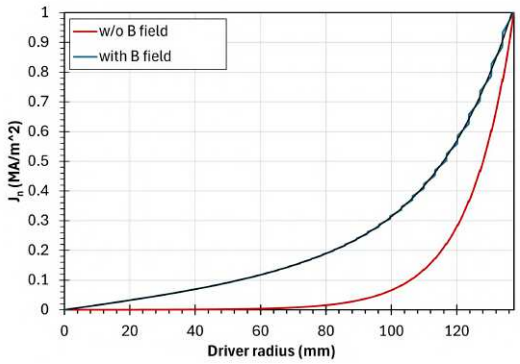

Figure 5.10: Normalized radial profile of the current density on the plasma considering a line at 7 cm from the bottom of the driver.

the excitation energy and A_{loss} is the total loss area. The loss area is given by:

$$A_{loss} = fA_{geom} = \frac{w}{p}A_{geom} \tag{5.22}$$

where f f is a factor defined as the ratio between the leak width w and the distance between the magnets "pitch" p. A_{geom} is the area dependent on the considered geometry. The leak width depends on the relationship:

$$w \propto \sqrt{r_{ce}r_{ci}} \propto \frac{1}{B} \tag{5.23}$$

where r_{ce} and r_ci are the mean electron and ion gyroradii, respectively.

Thus, the density relationship can be defined as:

$$n_s \propto \frac{P \propto 1/B_{vol}}{w \propto 1/B_{wall}} \tag{5.24}$$

Without proper considerations regarding the percentage of the loss area of the back wall of the driver, it is difficult to define whether the absence of magnets can actually contribute significantly to the increase in plasma density.

Dependence of the angle for the rz field plane

As previously stated, the limitation of the axisymmetric model requires choosing a specific angle θ for creating the 2-D map of the B_{rz} component necessary for calculating the plasma conductivity. In order to study the dependence on the chosen angle in estimating circuit parameters, a sensitivity analysis was conducted by repeatedly simulating the FEMM code, changing the angle used for creating the 2D map each time. In Figure 5.11, the active power profile generated by the model is shown as a function of the angle chosen for creating the map.

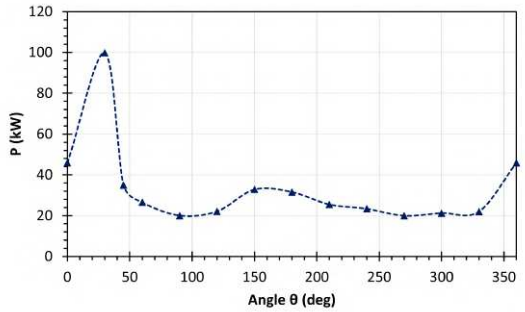

Figure 5.11: Active power simulation as a function of the angle used for creating the B_{rz} map in the definition of the plasma conductivity.

As evidenced by the profile graph, the non-symmetry of the field significantly affects the generated active power. In order to provide an average estimate of the power, it is possible to calculate an integrated average of the profile. In this case, the radial density profile has been defined as a descending line with a ratio between the density at the axis and the density at the wall equal to 0.7. The average power generated with this configuration is $P = 34.6$ kW.

Dependence on the shape of the radial profile

In the absence of radial density measurements, it is necessary to conduct a dedicated study of the density profile. Considering a cylindrical geometry under steady-state conditions with a specific source term, it is possible to define the following relationship between the density at the axis of the cylinder n_0 and the density at its wall $n_{s,R}$:

$$n_{s,R} = n_0 J_0(\beta r) \tag{5.25}$$

where J_0 is the zero-order Bessel function and β is a coefficient given by:

$$\beta = \left(\frac{\nu_{iz}}{D}\right)^{1/2} = \frac{\chi_{01}}{R} \tag{5.26}$$

where ν_{iz} is the ionization frequency and $\chi_{01} \simeq 2.405$.

Considering a ratio between the density at the axis and the density at the wall ranging from 1 to 0.7, ratios necessary to obtain a power at the coil current level similar to that measured during operations on MINION, it can be approximated to a straight line without losing generality. In this regard, by simulating the FEMM model using a Bessel function as the radial profile and a descending straight line, we obtain the results in Table 5.5.

Radial profile	$n_{s,R}/n_0$	$\mathbf{I}_p$ **(A)**	$\mathbf{V}_p$ **(kV)**	**R** (Ω)	**L** (μ**H**)	$\mathbf{P}_d$ **(kW)**
line	0.7	235	11.125	1.25557	7.5351	34.667
bessel	0.7	235	11.124	1.27183	7.53376	35.118

Table 5.5: Circuit parameters derived considering a radial density profile in the form of a descending straight line and a Bessel function. Angle at 45 degrees of the B_{rz} map with a filling pressure of 0.4 Pa.

As we can see from the circuit parameters derived from the simulation, the circuit inductance remains substantially unchanged compared to the test in vacuum, while the resistance approximately doubles. The power is in line with what was experimentally measured. The difference in radial profile results in minimal differences considering density ratios as high as these. Therefore, approximating the radial profile with a straight line is a good approximation when operating with these parameters.

Dependence on the density electrons and gas

Now, the dependence of inductive coupling on electron and neutral density is being analyzed. First, let's consider the dependence on electron density. As previously mentioned, the only measurement of electron density was obtained using the mobile Langmuir probe at the axis of the driver.

However, the density derived from the fitting function of the probe and obtained from the saturation current of ions corresponds to the plasma density at the sheath edge, assuming an effective velocity at the sheath edge. In detail:

$$n_{e,s} = \frac{j_{sat,i}}{u_B} \tag{5.27}$$

where $n_{e,s}$ is the density at the plasma sheath and $j_{sat,i}$ is the ion saturation current. The

density in the plasma bulk is found assuming quasi-neutrality and a Boltzmann factor can describe the electron density variation though the presheath. If Bohm velocity is used:

$$\frac{n_{e,b}}{n_{e,s}} = exp\left(\frac{-V_b - V_s}{T_e}\right) \simeq exp\left(-\frac{T_e/2}{T_e}\right) = 0.6 \tag{5.28}$$

Assuming therefore the density at the axis defined as either the plasma sheath density or bulk density, it is possible to derive the following power trend as defined in the graph in Figure 5.12. In this case, the map used to model the magnetic field considered an angle of 45 degrees and a radial density profile formed by a descending line.

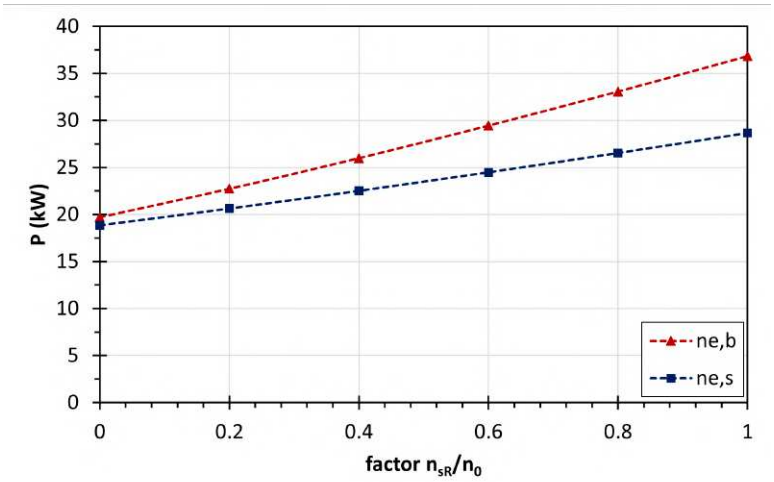

Figure 5.12: Profiles of active power measured by the FEMM model considering a radial density trend formed by a descending straight line as the ratio between the density at the axis and the density at the wall varies, For the two cases of interest of electron density. Filling pressure of 0.3 Pa.

From the analysis performed, we see that even considering the sheath density as the density at the axis, even with a uniform distribution, we never achieve an active power comparable to that measured experimentally. Considering instead the bulk density as the axial density, a power of approximately 35 kW is obtained with a pressure ratio of about 0.9.

Now let's consider how the dependence of gas density influences the inductive coupling model. In Figure 5.13, a sketch of the gas measurement system is shown. Considering two chambers filled with gas with a temperature gradient at equilibrium, the gas flow through the connecting duct must be zero, because at the end the duct has installed a pressure gauge, so that $\Gamma_{out} = \Gamma_{in}$.

For this equilibrium of fluxes, it is therefore, possible to write the following relationship:

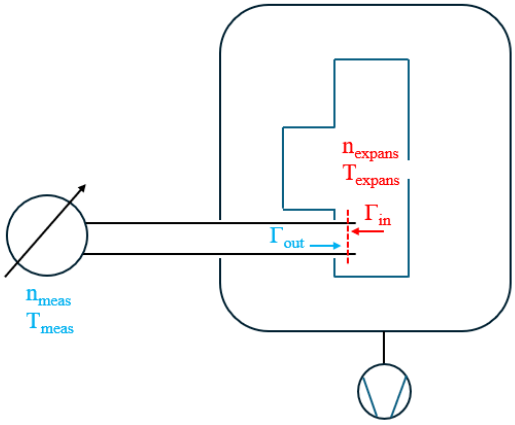

Figure 5.13: Sketch of the gas injection system of MINION.

$$\frac{p_{meas}}{\sqrt{2\pi k_B T_{meas} m_{gas}}} = \frac{p_{expans}}{\sqrt{2\pi k_B T_{expans} m_{gas}}} \tag{5.29}$$

from which, considering the fact that in the RF driver and in the expansion chamber the gas is heated by the presence of the plasma, we can derive a correction factor that relates the density in the expansion region to the density measured at the gauge. This ratio, also called thermal transpiration effect, reads::

$$\frac{p_{expans}}{p_{meas}} = \sqrt{\frac{T_{expans}}{T_{meas}}} = \frac{n_{meas}}{n_{expans}} \tag{5.30}$$

In our case of interest, during the plasma discharge the pressure measurement shows a clear reduction in correspondence to the duration of the plasma discharge, as shown in Figure 5.14. p_{meas} corresponds to approximately $p_{meas} = 0.5 p_{fill}$. So, a good estimation for the gas density inside the ion source is:

$$n_{expans} = \sqrt{\frac{T_{expans}}{T_{meas}}} \cdot \frac{p_{meas}}{p_{fill}} \cdot n_{fill} \tag{5.31}$$

with the filling density obtained using the ideal gas law from the imposed filling pressure at room temperature, as $n_{fill} = \frac{p_{fill}}{k_B T}$.

According to preliminary evaluations, a gas temperature of the order of 550-600 K can be taken for the hydrogen molecules during the plasma, with minor corrections to take into account the atomic fraction. The measurement is taken at about room temperature (or slightly higher). For the shots considered in this section, the reduction of the istantaneous pressure from the filling pressure is about $p_{meas}/p_{fill} \approx 0.72$. Therefore, $n_{gas} = n_{expans} \approx 0.75 \cdot 0.72 \cdot n_{fill}$, i.e. about 5×10^{19} m^{-3}.

Considering this ratio between filling density and neutral density, a sensitivity study

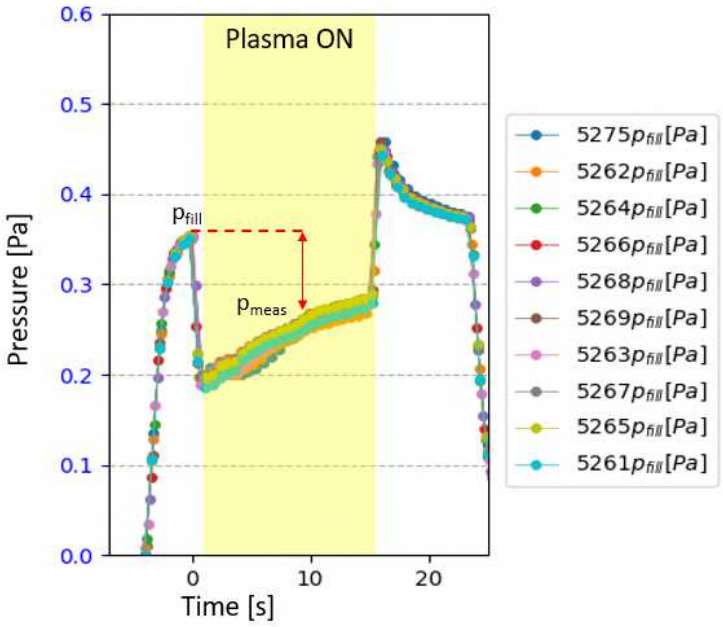

Figure 5.14: Behavior of the filling pressure in the expansion chamber during the experimental operations for various shots performed.

was conducted by varying the filling pressure. In detail, three cases of interest were considered, with p_{fill} equal to 0.3, 0.4, and 0.5 Pa.

In the graph of Figure 5.15, the trend of the active power obtained from the FEMM model is shown, varying the ratio between the electron density at the axis and the electron density at the driver's wall, considering a radial linear trend and a magnetic field derived from the 2-D map with a 45-degree angle.

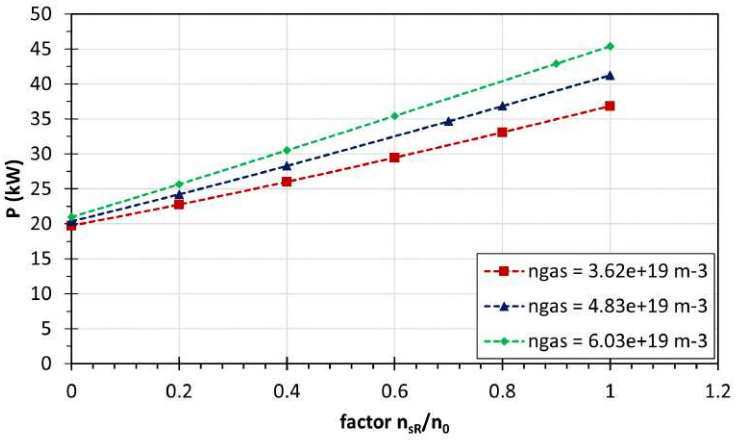

Figure 5.15: Active power obtained for filling pressures of 0.3, 0.4, and 0.5 Pa, varying the ratio between electron density at the axis and at the wall.

From the trends obtained with the model, we can see that as the filling pressure increases, and consequently the neutral density increases, it's possible to obtain higher

powers at the same ratio between electron densities.

5.5 Estimation of the coupling efficiency and suggested optimizations

In this final section, we present an estimation of the efficiency of the RF source in terms of power dissipated on the metal structures and power coupled with the plasma. Then several analyses are proposed aimed at studying some geometric implementations useful for improving the performance of the source. Finally, a brief analysis of the most promising magnetic configuration of the driver is proposed, which will be tested in SPIDER and in the future MINION.

5.5.1 Power coupled to the metallic structures in the presence of the plasma and coupling efficiency

Considering the sensitivity study conducted in the previous section and verifying the robustness of the implemented model, the aim is to estimate the efficiency of the source. To achieve this, the model was simulated by applying the same current to the coil, first in a vacuum condition and then implementing the plasma model. Regarding the latter, the conductivity map was generated considering a radial profile as a Bessel function and a ratio between axial pressure and wall pressure of 0.7. The magnetic field was generated considering a 45-degree map and a fill pressure $p_{fill} = 0.4$ Pa. The Table 5.6 summarizes the main parameters derived in terms of supplied power P_d, power absorbed by the metal structures P_{diss}, and power coupled to the plasma P_{abs}.

Condition	**I (A)**	**P$_d$ (kW)**	**P$_{diss}$ (kW)**	**P$_{abs}$ (kW)**
Vaccum	235	17.522	17.522	-
Plasma	235	35.118	17.418	17.700

Table 5.6: Simulative results of the power supplied, dissipated by the metal structures, and coupled to the plasma.

From these experimental results, we can then proceed to estimate the efficiency of the RF source in terms of power coupled with the plasma compared to the total supplied power:

$$\eta = \frac{P_{abs}}{P_d} = 0.504 \tag{5.32}$$

Approximately half of the power supplied to the source is dissipated on the passive metal structures. Among them, the Faraday shield absorbs approximately 11.7 kW,

which is about 67% of the total dissipated power. Extensive studies and research into engineering solutions aimed at reducing these losses are underway.

5.5.2 Suggested modifications for the optimization of the coupling efficiency

In this section, we evaluate possible design modifications that could be improve the coupling efficiency of the RF driver.

First of all, we note the poor coupling occurring at the bottom of the driver: as shown in Figure 5.9a, there can be no induced currents in the plasma in correspondence of the bottom half of the RF antenna (four of the eight coils), due to the presence of the magnetic field from the magnets embedded in the rear of the driver.

As shown in Figure 5.7a, for a given plasma the coupled power would increases linearly with 1/B. The confining effect of cusp magnets is also proportional to 1/B [5]. From this first order dependences, we shall expect that removing the magnets would not give a net gain in terms of plasma density. The straighforward solution would be to increase the driver length. However, a quantitative analysis of the improvement cannot be obtained from the presented numerical models, because they require the knowledge of the plasma density, which clearly not available for such a modified configuration. This modification is a major one, and would require years to manufacture the modified drivers and install them in SPIDER prototype.

As a second point, we note that the poor coupling occurring on the rear part of the driver may imply that the coil design is not an optimized one. Ideally, a coil with a reduced length could in principle provide the same net power coupled to the plasma. This design modification could require a reduction of the number of turns, meaning a full redesign of the matching network and - probably - an increase of the voltage drop along the single turn. The voltage between the turns directly influences the discharge probability in the region of the RF coil, and may not be possible. Alternatively, a reduction of the conductor cross-section may allow a maintaining the same number of coils but reduce the coil length; also in this case the matching network would have to be modified.

Finally, there are two design optimization with good feasibility and minor drawbacks, namely: - distance of the electromagnetic screen (EMS) to increase the induced fields; - use of the Ferromagnetic screen to reduce the magnetic field strength in the region where the RF coupling shall occur.

Using the benchmarked model, in the following sections we evaluated these two possible design improvements, as they are feasible options for design improvements and actually the second option was selected for the immediate test in SPIDER during

2024.

Dependency on the driver's geometry

A brief is presented regarding the effects of the EMS position relative to its proximity to the coil on the induced field inside the driver. As reported previously during the general description of the MINION driver, unlike the original design of SPIDER, the electromagnetic shield has been brought closer to the coil by 10 mm. This modification was made due to geometric constraints, as there are two adjacent drivers in SPIDER. The radial profiles of the induced field are shown in the graphs in Figure 5.16, varying the distance δ between the EMS and the Faraday shield lateral wall.

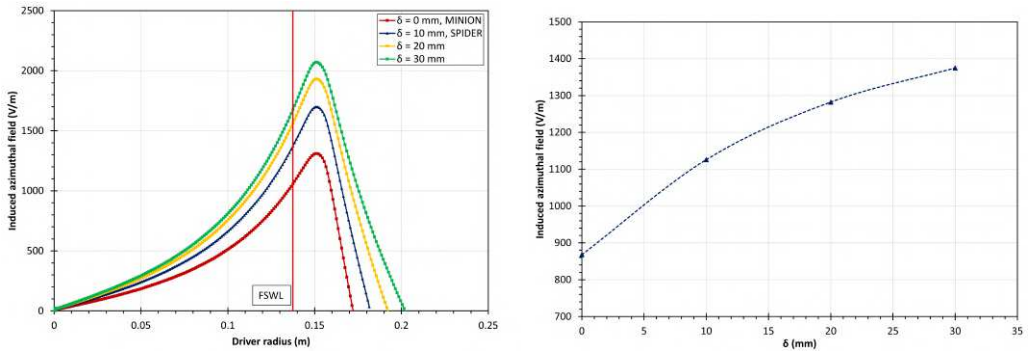

(a) (b)

Figure 5.16: FEMM simulation with 200 A applied to the coil: (a) induced field considering a radial profile at 7 cm from the driver back plate, approximately halfway up the driver, as the distance δ varies between the FSLW and the EMS; b) induced field at 1 mm inside the FSLW as the distance δ between FSLW and EMS. varies.

As we can see from the simulations performed, the variation in distance between the Faraday shield lateral wall and the EMS plays a significant role in the induced field, and therefore in the induced current in the plasma. Specifically, bringing the electromagnetic shield closer, results in greater confinement of the RF field, limiting the induced field required to ignite the plasma inside the driver. With the configuration used in MINION, compared to the original one in SPIDER, more power is therefore needed to ignite and sustain the plasma.

Regarding the arrangement of magnets on the bottom of the driver, during sensitivity studies conducted by varying the field intensity, it has already been demonstrated how it is inherently challenging to determine whether removing these magnets could lead to an improvement in coupling. Eliminating the confinement field would indeed result in an increase in the loss area at the bottom of the driver where the gas density is very high. However, one possible implementation could be to elongate the driver. This modification would lead to an increase in coupling since the coil would be further

axially away from the magnets at the bottom without losing magnetic confinement at the back plate.

5.5.3 Analysis of coupling with the configuration with Fe shield

Finally, an interpretation is proposed regarding the potential improvement resulting from the use of the driver configuration without cusp magnets but with the ferromagnetic shield. This configuration has been identified as the best as it allows for a higher electron density at the plasma grid and will be implemented in the upcoming experimental campaign of SPIDER.

Utilizing the FEMM model, despite the various limitations outlined due to the use of an axisymmetric model, a qualitative interpretation of the improvement in terms of coupled power is intended to be provided. To achieve this, the iron shield was implemented in the magnetic model of Ansys, in addition to the magnets positioned at the bottom of the driver. This allowed us to derive a map of the magnetic field used for defining the plasma conductivity map. Figure 5.17 shows the result of the FEMM simulation in terms of current absorption and the derived conductivity map. To ensure consistency with previous analyses, the simulation was conducted with the same coil current, a radial trend with a Bessel function, and an electron density ratio of 0.7, considering the 45-degree field map.

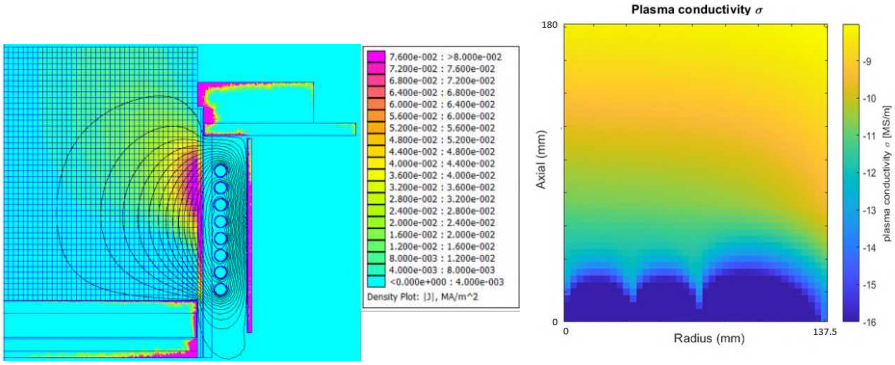

(a) (b)

Figure 5.17: Operating condition with Fe shield and magnetic field of the magnets at the BP: (a) map of the current density on the plasma, (b) map of plasma conductivity.

From the FEMM simulation we obtain an active power equal to $P_d = 50.433$ kW compared to that obtained without considering the ferromagnet, which was equal to $P_d = 35.118$ kW, see Table 5.5. An increase in power equivalent to the density used to define the plasma conductivity translates practically into a potential increase in plasma density at the same power level. Of course, this is a purely approximate estimate since the model, with its limitations, is difficult to calibrate without experimental measure-

ments. However, it provides an idea of the possible improvements of this configuration. After the subsequent experimental testing phase and better analyses, more accurate assessments can be made.

Chapter 6

Conclusions

The work carried out in this thesis focuses on the MINION experiment, with the commissioning phase of various plants, initial measurements, and on a specific studies and simulations of the inductive coupling with plasma.

The commissioning of the individual plants allowed successful operation during the experimental phase. In order to achieve a proper calibration of the gas injection system, necessary to ensure stable and reproducible conditions during operations, simplified models have been developed to obtain a good estimation of the vacuum system parameters, e.g. conductance between the source and the vessel and the pumping speed, see Figure 3.8. To characterize the source feeding system, electrical measurements of the transmission line between the oscillator and the load were performed, necessary for the correct calibration of the matching network used to achieve optimal coupling between the power supply and the load. Furthermore, the commissioning phase involved the installation of various diagnostics used for plasma characterization, to which I dedicated myself by working alongside the team of specialized technicians.

To aid in the understanding of the collected data of the various magnetic confinement configurations, magnetic measurements and simulations were conducted and compared with the results gathered from Langmuir probe. In detail, an Ansys model was implemented for the magnetic simulation of the two main cusp magnet configurations and for the analysis of the effects of the filter field on the plasma expansion in the ion source. A great attention was devoted to the experimental validation of the model, accurately measuring with a gaussmeter the components of the magnetic field along various directions, obtaining a very good agreement between measurements and simulations (see for instance Figure 4.3 and Figure 4.5). On this basis, the magnetic field lines calculated for the various configurations was used to describe and explain the expansion of the plasma from the driver. As shown for instance in Figure 4.9, the hot electrons from the driver are found to be largely magnetized and to follow the field

lines in their motion. To this purpose, my role in the preparation of the visible camera diagnostic and acquisition was also key to allow this interpretation.

From the analysis of the experimental data collected through diagnostics it was found that the magnetic configuration involving the use of 12 cusp magnets inside the driver allows for greater plasma confinement but requires too much power to initiate and sustain the plasma. The magnetic configurations with 24 cusp magnets and the one without cusp magnets but with the ferromagnetic shield positioned around the driver, prove to be the most promising in terms of lower plasma potential and higher electron density at the plasma grid, see Figure 4.14. Future experiments implementing diagnostics available to sample the 3D space will be necessary to gain a better understanding of these configurations.

The main focus of the thesis work was aimed at better understanding the operation of inductive coupling. For this purpose, an axisymmetric model of the RF driver was developed using finite element analysis software (FEMM). This model was first validated by comparing simulated circuit parameters with those obtained through low-voltage tests in vacuum, yielding optimal agreement with the electrical measurements of transmitted direct power and inductance. Subsequently, a model for simulating plasma inside the driver was implemented, considering a sensitivity study of the main phenomena influencing the spatial distribution of the plasma.

In detail, the variation of inductive coupling was studied considering the role of the asymmetric magnetic field produced by the magnets on the bottom of the driver, taking into account the radial profile of the plasma and considering the role of neutrals. It has been demonstrated that the magnetic field from the bottom magnets plays a crucial role in the distribution of plasma conductivity reducing the diffusion of charged particles, as shown in Figure 5.8 and Figure 5.9, but that this field is still necessary to reduce losses on the bottom of the driver. Regarding the radial profile, it has been shown that the coupled power significantly depends on the radial distribution, see Figure 5.12, indicating that future models will require spatial measurements of density and temperature for increased accuracy. Moreover, it has been observed that the density of neutrals plays a key and dominant role in estimating plasma conductivity, and thus in the effectiveness of inductive coupling, see Figure 5.15.

Finally, the efficiency of the coupling was estimated by simulating the axisymmetric model, demonstrating that only about half of the power supplied to the system is actually coupled with the plasma. The values obtained for the axisymmetric case do not deviate significantly from those of currently used sources.

Therefore, future studies and implementations are necessary to improve the efficiency of these radiofrequency sources. The next experimental campaign of SPIDER will involve the use of drivers with the ferromagnetic shield around the coil, as this

configuration has shown the best results on MINION. The axisymmetric model implemented in this thesis work serves as a foundation for future more comprehensive three-dimensional simulations of the source, aimed at achieving a better understanding of the coupling with the plasma.

Ringraziamenti

Un ringraziamento particolare al mio relatore prof. Emanuele Sartori per lunghe chiacchierate, le serate passate davanti alle simulazioni e ai fogli volanti, la pazienza e il supporto datomi nella stesura di questo elaborato.

Un caro ringraziamento ad Isabella per aver letto più volte questa tesi e per avermi fatto sentire come a casa durante le giornate passate ad RFX. A Gianluigi e Antonio per i consigli preziosi e a tutto il gruppo di lavoro che ha ruotato attorno a MINION.

A Daniele con cui ho condiviso questi cinque anni universitari tra treni, pranzi al sacco e nottate di studio. Grazie di aver condiviso difficoltà , momenti di sconforto e di incertezza, ma soprattutto risate, soddisfazioni e spensieratezza. Senza il tuo aiuto e le tue idee sarebbe stato tutto diverso.

Ringraziamento speciale a Mattia per essermi amico e compagno di peripezie da una vita, per essersi sorbito i miei sfoghi ma anche per aver condiviso con me i momenti felici in tutti questi anni. Grazie di esserci sempre.

Alla mia famiglia per avermi supportato e accompagnato nelle mie scelte senza mai avermi fatto mancare nulla.

Ai miei amici storici e a tutti coloro che ho conosciuto in questi anni universitari che hanno reso questo percorso più un'esperienza di vita che di studio.

Ai miei affetti più cari che in questi anni mi hanno accompagnato e hanno creduto in me, questi tesi è dedicata anche a voi.

Bibliography

[1] Hannah Ritchie, Pablo Rosado, and Max Roser. Energy production and consumption. *Our World in Data*, 2020. https://ourworldindata.org/energy-production-consumption.

[2] William Moebs Samuel J. Ling, Jeff Sanny. *University Physics Volume 3*. OpenStax, 2016. https://openstax.org/books/university-physics-volume-3/pages/1-introduction.

[3] Q. M. Tran M. Kikuchi, K. Lackner. *Fusion physics*. International Atomic Energy Agency Vienna, 2012.

[4] A.M. Bradshaw, T. Hamacher, and U. Fischer. Is nuclear fusion a sustainable energy form? *Fusion Engineering and Design*, 86(9):2770–2773, 2011. ISSN 0920-3796. doi: https://doi.org/10.1016/j.fusengdes.2010.11.040. URL `https://www.sciencedirect.com/science/article/pii/S0920379610005119`. Proceedings of the 26th Symposium of Fusion Technology (SOFT-26).

[5] M.A. Lieberman and A.J. Lichtenberg. *Principles of Plasma Discharges and Materials Processing*. Wiley, 2005. ISBN 9780471724247. URL `https://books.google.it/books?id=m0iOga2XE5wC`.

[6] Arnab Rai Choudhuri. *The Physics of Fluids and Plasmas: An Introduction for Astrophysicists*. Cambridge University Press, 1998.

[7] URL `https://euro-fusion.org/devices/jet/`.

[8] URL `https://www.ipp.mpg.de/w7x`.

[9] URL `https://www.iter.org/`.

[10] H.P.L. de Esch, D. Stork, C. Challis, and B. Tubbing. The optimization of neutral beams for ignition and burn control on next-step reactors. *Fusion Engineering and Design*, 26(1):589–604, 1995. ISSN 0920-3796. doi: https://doi.org/

10.1016/0920-3796(94)00226-W. URL https://www.sciencedirect.com/science/article/pii/092037969400226W. Proceedings of the Fifth International Toki Conference on Plasma Physics and Controlled Nuclear Fusion.

[11] Marthe Bacal and Motoi Wada. Negative hydrogen ion production mechanisms. *Applied Physics Reviews*, 2:021305, 06 2015. doi: 10.1063/1.4921298.

[12] Hemsworth Ronald et al. Status of the iter heating neutral beam system. *Nuclear Fusion*, 49:045006, 03 2009. doi: 10.1088/0029-5515/49/4/045006.

[13] *ITER Technical Basis*. Number 24 in ITER EDA Documentation Series. INTERNATIONAL ATOMIC ENERGY AGENCY, Vienna, 2002. URL https://www.iaea.org/publications/6492/iter-technical-basis.

[14] O. W. Richardson. The emission of electricity from hot bodies. *Nature*, 98, 1916. doi: 10.1038/098146a0.

[15] S. Peruzzo et al. Thermal analyses for the design of the iter-nbi arc driven ion source. *Fusion Engineering and Design*, 2007. URL https://www.academia.edu/20640019/Thermal_analyses_for_the_design_of_the_ITER_NBI_arc_driven_ion_source.

[16] R. S. Hemsworth, A. Tanga, and V. Antoni. Status of the ITER neutral beam injection system (invited)a). *Review of Scientific Instruments*, 79(2):02C109, 02 2008. ISSN 0034-6748. doi: 10.1063/1.2814248. URL https://doi.org/10.1063/1.2814248.

[17] Marcuzzi D. et al. Design of the rf ion source for the iter nbi. *Fusion Engineering and Design*, 82(5-14):798–805, 2007. doi: 10.1016/j.fusengdes.2007.07.033.

[18] Jain P. et al. Estimation of plasma electron density inside the radio frequency inductively coupled driver of spider. In *2020 IEEE International Conference on Plasma Science (ICOPS)*, pages 25–25, 2020. doi: 10.1109/ICOPS37625.2020.9717701.

[19] D Zielke, S Briefi, and U Fantz. Rf power transfer efficiency and plasma parameters of low pressure high power icps. *Journal of Physics D: Applied Physics*, 54(15):155202, feb 2021. doi: 10.1088/1361-6463/abd8ee. URL https://dx.doi.org/10.1088/1361-6463/abd8ee.

[20] Na Wang et al. Design optimization of slit aperture faraday shield for rf ion source in craft nnbi system. *Fusion Engineering and Design*, 183:113272, 2022. ISSN

0920-3796. doi: https://doi.org/10.1016/j.fusengdes.2022.113272. URL https://www.sciencedirect.com/science/article/pii/S0920379622002642.

[21] M. Bacal. Physics aspects of negative ion sources. *Nuclear Fusion*, 46(6):S250, may 2006. doi: 10.1088/0029-5515/46/6/S05. URL https://dx.doi.org/10.1088/0029-5515/46/6/S05.

[22] Yu.I. Belchenko, G.I. Dimov, and V.G. Dudnikov. A powerful injector of neutrals with a surface-plasma source of negative ions. *Nuclear Fusion*, 14(1):113, jan 1974. doi: 10.1088/0029-5515/14/1/017. URL https://dx.doi.org/10.1088/0029-5515/14/1/017.

[23] Fantz U. et al. Diagnostics of the cesium amount in an rf negative ion source and the correlation with the extracted current density. *Fusion Engineering and Design*, 74:299–303, 11 2005. doi: 10.1016/j.fusengdes.2005.06.184.

[24] P. Franzen et al. Progress of the development of the ipp rf negative ion source for the iter neutral beam system. *Nuclear Fusion*, 47(4):264, mar 2007. doi: 10.1088/0029-5515/47/4/004. URL https://dx.doi.org/10.1088/0029-5515/47/4/004.

[25] James D. Callen. *Fundamentals of Plasma Physics*. University of Wisconsin, 2006.

[26] Agostinetti P. et al. Design of a low voltage, high current extraction system for the ITER Ion Source. In Elizabeth Surrey and Alain Simonin, editors, *Negative Ions, Beams and Sources*, volume 1097 of *American Institute of Physics Conference Series*, pages 325–334, March 2009. doi: 10.1063/1.3112529.

[27] Franzen P. et al. Performance of multi-aperture grid extraction systems for an ITER-relevant RF-driven negative hydrogen ion source. *Nuclear Fusion*, 51(7):073035, July 2011. doi: 10.1088/0029-5515/51/7/073035.

[28] S. Mochalskyy, A.F. Lifschitz, and T. Minea. 3d modelling of negative ion extraction from a negative ion source. *Nuclear Fusion*, 50(10):105011, sep 2010. doi: 10.1088/0029-5515/50/10/105011. URL https://dx.doi.org/10.1088/0029-5515/50/10/105011.

[29] Fubiani G. et al. Modeling of negative ion extraction from a magnetized plasma source: Derivation of scaling laws and description of the origins of aberrations in the ion beam. *Physics of Plasmas*, 25(2):023510, February 2018. doi: 10.1063/1.4999707.

[30] Ralph Hollinger. *Ion Extraction*, chapter 5, pages 61–86. John Wiley and Sons, Ltd, 2004. ISBN 9783527603954. doi: https://doi.org/10.1002/3527603956.ch5. URL https://onlinelibrary.wiley.com/doi/abs/10.1002/3527603956.ch5.

[31] G. Serianni et al. First operation in spider and the path to complete mitica. *Review of Scientific Instruments*, 91(2):023510, feb 2020. doi: 10.1063/1.5133076.

[32] Pasqualotto R. et al. Diagnostics of the iter neutral beam test facility. *Rev Sci Instrum*, 83(2):02B103, 2012. doi: 10.1063/1.3662017.

[33] Marcuzzi D. et al. Detail design of the beam source for the spider experiment. *Fusion Engineering and Design*, 85(10):1792–1797, 2010. ISSN 0920-3796. doi: https://doi.org/10.1016/j.fusengdes.2010.05.039. URL https://www.sciencedirect.com/science/article/pii/S0920379610002516. Proceedings of the Ninth International Symposium on Fusion Nuclear Technology.

[34] Pimazzoni A. et al. Co-extracted electrons and beam inhomogeneity in the large negative ion source spider. *Fusion Engineering and Design*, 168:112440, 2021. ISSN 0920-3796. doi: https://doi.org/10.1016/j.fusengdes.2021.112440. URL https://www.sciencedirect.com/science/article/pii/S0920379621002167.

[35] Sonato P. et al. The iter full size plasma source device design. *Fusion Engineering and Design*, 84:269–274, 06 2009. doi: 10.1016/j.fusengdes.2008.11.095.

[36] D. Marcuzzi et al. Lessons learned after three years of spider operation and the first mitica integrated tests. *Fusion Engineering and Design*, 191:113590, 2023. ISSN 0920-3796. doi: https://doi.org/10.1016/j.fusengdes.2023.113590. URL https://www.sciencedirect.com/science/article/pii/S0920379623001746.

[37] Sartori E. et al. Design of a large nonevaporable getter pump for the full size iter beam source prototype. *Journal of Vacuum Science & Technology B*, 41(3):034202–1–034202–12, 2023.

[38] Siragusa M. et al. Numerical simulation of experimental tests performed on zao® non-evaporable-getter pump designed for neutral beam injector applications. *Rev Sci Instrum*, 91(2):023501, 2020. doi: 10.1063/1.5128662.

[39] Agostinetti P. et al. Detailed design optimization of the mitica negative ion accelerator in view of the iter nbi. *Nuclear Fusion*, 56:016015, 01 2016. doi: 10.1088/0029-5515/56/1/016015.

[40] I. mario et al. Optimizing the iter nbi ion source by dedicated rf driver test stand. In *Journal of Physics*, 2023. Submitted for Presentation.

[41] Marconato N. et al. Integration of new sets of magnets for improved plasma confinement in the spider experiment. *Fusion Engineering and Design*, 193: 113805, 2023. ISSN 0920-3796. doi: https://doi.org/10.1016/j.fusengdes.2023.113805. URL https://www.sciencedirect.com/science/article/pii/S0920379623003873.

[42] Robert L. Merlino. Understanding Langmuir probe current-voltage characteristics. *American Journal of Physics*, 75(12):1078–1085, 12 2007. ISSN 0002-9505. doi: 10.1119/1.2772282. URL https://doi.org/10.1119/1.2772282.

[43] Poggi C. et al. Langmuir probes as a tool to investigate plasma uniformity in a large negative ion source. 50(11):3890–3896, 2022. doi: 10.1109/TPS.2022.3181805.

[44] Maher I. Boulos, Pierre L. Fauchais, and Emil Pfender. *Plasma Diagnostics, Optical Emission and Absorption Spectroscopy*, pages 963–1023. Springer International Publishing, Cham, 2023. doi: 10.1007/978-3-030-84936-8_18. URL https://doi.org/10.1007/978-3-030-84936-8_18.

[45] B. H. Bransden and C. J. Joachain. *Physics of Atoms and Molecules*. Pearson Education, Harlow, England, 2003.

[46] Zaniol B. et al. NIO1 diagnostics. 1655:060010, April 2015. doi: 10.1063/1.4916479.

[47] B. Ferrario and A. Calcatelli. *Introduzione alla tecnologia del vuoto*. Pàtron, 1999. ISBN 9788855525107. URL https://books.google.it/books?id=iErIPAAACAAJ.

[48] G. Ramanan and G. R. Freeman. Electron mobilities in low density hydrogen and carbon monoxide gases: Momentum transfer cross sections at very low energies. *The Journal of Chemical Physics*, 95(6):4195–4200, 09 1991. ISSN 0021-9606. doi: 10.1063/1.460775. URL https://doi.org/10.1063/1.460775.

[49] Yoon Jung-Sik et al. Cross Sections for Electron Collisions with Hydrogen Molecules. *Journal of Physical and Chemical Reference Data*, 37(2):913–931, 03 2008. ISSN 0047-2689. doi: 10.1063/1.2838023. URL https://doi.org/10.1063/1.2838023.